Abstract

NEALIS, JAMES MATTHEW. Model-Based Robust Control Designs for High Performance Magnetostrictive Transducers. (Under the direction of Ralph C. Smith.)

The increasing employment of smart structures in industrial, automotive, aerospace, and aeronautic processes necessitates the study of materials exhibiting constitutive nonlinearities and hysteresis. The high performance and high speed demands of such processes can often be met by transducers utilizing piezoceramic, shape memory alloy, or magnetostrictive elements.

Here, the focus is placed on magnetostrictive materials. These materials provide several benefits such as the ability to generate large forces and strains and provide precision placement. However, to achieve the full potential of magnetostrictive materials, models and control laws which accommodate the inherent nonlinearities and hysteresis must be employed. Furthermore, it is advantageous to consider material characterization, model development, and control design simultaneously to fully exploit unique sensor and actuator capabilities of these magnetostrictive materials in coupled systems. An emphasis has been placed on the design of models for magnetostrictive transducers and control strategies that are implementable in real time and incorporate realistic operating conditions.

To this end, models of the nonlinearities and hysteresis exhibited by magnetostrictive materials are developed considering not only accuracy, but the computational

efficiency and the existence of an inverse or partial inverse as well. To attenuate the nonlinear and hysteretic behaviors, we employ the inverses of the material models as filters of the input to the transducer. The models describing the nonlinearities and hysteresis for the smart materials, contain several material dependent parameters which must be identified in order to effectively utilize resulting inverse compensators.

A nonlinear adaptive parameter estimation algorithm is developed to identify nonlinearly occurring parameters which may not be identified by physical measurements or may be slowly varying. This method can be utilized during the control process and requires no additional data collection.

Once an inverse filter has been developed and the material parameters identified, feedback control laws are designed to meet the performance specifications. A successful controller must provide accurate tracking of a reference signal while accommodating the hysteretic behavior and other external disturbances such as sensor noise. Several initial feedback control methods are considered including a linear adaptive control method, PID control, and optimal LQR control, to motivate the investigation of robust control designs. Robust techniques including H_2 and H_∞ optimal control as well as multiple objective control designs are employed to control a magnetostrictive transducer and the performance is illustrated through simulations. We demonstrate the techniques on a magnetostrictive transducers but they are sufficiently general to be extended to several commonly used smart materials.

June 5, 2003

MODEL-BASED ROBUST CONTROL DESIGNS FOR HIGH PERFORMANCE MAGNETOSTRICTIVE TRANSDUCERS

BY

James M. Nealis

A DISSERTATION SUBMITTED TO THE GRADUATE FACULTY OF

NORTH CAROLINA STATE UNIVERSITY

IN PARTIAL FULFILLMENT OF THE

REQUIREMENTS FOR THE DEGREE OF

DOCTOR OF PHILOSOPHY

APPLIED MATHEMATICS

RALEIGH, NORTH CAROLINA

June 2003

APPROVED BY:

Ralph C. Smith CHAIR OF ADVISORY COMMITTEE	K. Ito
H. Tran	F. Wu

Biography

The author was born in Livonia, Michigan and moved to Cary, North Carolina at the age of one. He graduated from Apex High School and then attended North Carolina State University. He graduated magna cum laude with bachelor of science degrees in mathematics and mathematics education in 1997. He stayed on at North Carolina State University and received a master of science degree in applied mathematics with a concentration in computation mathematics in 2001 and a doctorate degree in applied mathematics in 2003.

Acknowledgments

There are several groups and individuals I must acknowledge for their support and contributions during my graduate work. Without the generosity and assistance of the following, the completion of this dissertation would not have been possible.

Foremost, I must extend my deepest gratitude to my advisor Ralph Smith. Dr. Smith's enthusiasm, vast knowledge and creativity generated my attraction to the field of applied mathematics and he has proven to be an invaluable resource and mentor. His enduring dedication to the field of mathematics has provided motivation in my graduate career. I owe him many thanks for his guidance as well as several smoothies.

My committee members Dr. Hien Tran, Dr. Kazufumi Ito and Dr. Fen Wu also deserve recognition. I greatly appreciate the time and effort they have extended. Both in and out of the classroom, they have taught me much and their assistance was irreplaceable.

My research was made possible through funding from the Air Force Office of Scientific Research under the grant AFOSR-F49620-01-1-0107.

I would like to acknowledge Brenda Currin and Rory Schnell for all of the assistance and support they have given during my graduate career. They supplied much more than administrative assistance and were crucial to reducing my stress level and maintaining my state of mind.

A large portion of the credit for the completion of this dissertation must go to my fiance Monica. Her patience and support allowed me to fulfill my academic goals and made my years in graduate school not only bearable but enjoyable. Her understanding and friendship has given me respite from the stress and strains of school and the rest of the world.

My family has kept me focussed and given me an escape from mathematics when needed, which is often. Their friendship and support are greatly appreciated and have made occasional difficult times less difficult. I would especially like to acknowledge my parents since I can not thank them enough for everything they have given throughout my life.

Finally, I must recognize Maxine for her company during long nights of work. It is nice to have someone to talk to, especially if they can't talk back.

Table of Contents

List of Tables **vii**

List of Figures **viii**

1 Introduction **1**

2 Hysteresis Models **6**
2.1 Domain Wall Model 6
2.1.1 Domain Wall Model Inverse 10
2.2 Preisach Model 12
2.2.1 Preisach Inverse 16
2.3 Free Energy Model 19
2.3.1 Free Energy Model Implementation Algorithm 27
2.3.2 Inverse Energy Hysteresis Model 29
2.4 Concluding Remarks 30

3 Full Transducer Model **32**
3.1 Rod Dynamics 32
3.1.1 Finite Element Method 35
3.1.2 Linearized Model 37
3.2 ODE Model for Transducer Dynamics 39
3.3 Concluding Remarks 43

4 Nonlinear Parameter Estimation **44**
4.1 Scalar Equation Case 46
4.2 Vector System 53
4.3 Numerical Examples 56
4.3.1 Scalar Case 56
4.3.2 Vector System 57

4.4 Concluding Remarks 59

5 Preliminary Control Methods **62**
5.1 Linear Adaptive Control 63
5.1.1 Update Law 64
5.1.2 Numerical Example 70
5.2 PID Control 73
5.3 LQR Control 81
5.4 Concluding Remarks 85

6 Robust Control Methods **87**
6.1 H_2 and H_∞ Designs 88
6.1.1 System Representation 89
6.1.2 Minimal realization 92
6.1.3 Weighting Functions 94
6.1.4 H_2 Optimal Control Design 98
6.1.5 H_∞ Sub-optimal Control Design 105
6.2 Multiobjective Control 110
6.2.1 System Representation 116
6.2.2 Mixed l_1 and H_2 Control 120
6.2.3 Mixed l_1 and H_∞ Control 123
6.2.4 Mixed l_1, H_2 and H_∞ Control 125
6.3 Concluding Remarks 127

7 Conclusion **129**

A Proof of Theorem 4.1 **133**

List of References **139**

List of Tables

2.1 Parameters for the domain wall model. 10
2.2 Parameters for the Preisach model. 15
2.3 Parameters for the free energy model. 26

3.1 Zeros and poles of (3.16) utilizing 2 basis functions. 40
3.2 Zeros and poles of (3.16) utilizing 8 basis functions. 41
3.3 ODE model parameters for Terfenol-D transducer. 42
3.4 Maximum error between finite element model and ODE model. 43

5.1 Adaptive control method parameters. 72

List of Figures

1.1 Effects of hysteresis 2
1.2 Control system incorporating inverse compensator method. 2
1.3 Prototypical magnetostrictive transducer. 4

2.1 Ising spin model of anhysteretic magnetization. 8
2.2 Domain wall model of magnetization. 10
2.3 Inverse of domain wall model 11
2.4 Partial inverse of domain wall model 12
2.5 Preisach straight line hysteresis model. 13
2.6 Comparison of Preisach model and domain wall model. 16
2.7 Approximate hysteresis inverse model. 18
2.8 Progression of magnetization due to an applied field. 20
2.9 Gibbs energy and local magnetization for increasing applied field . . . 21
2.10 Varying field levels for the limiting case local average magnetization $\overline{M}$. 24
2.11 Free energy profiles for nonhomogeneous domain structure 25
2.12 Validation of the free energy hysteresis model 27
2.13 Error in linearization caused by free energy model inverse 30

3.1 Rod model for Terfenol-D transducer. 34
3.2 Basis elements. 35
3.3 Response of finite element method 38
3.4 Finite element verses spring model response. 42

4.1 Domain wall hysteresis models for two values of a. 45
4.2 Saturation function $\mathrm{sat}(x)$. 47
4.3 Concave and convex covers. 50
4.4 Verification of persistent excitation condition 57
4.5 Scalar adaptive nonlinear parameter estimation example 58
4.6 Parameter estimate value for matrix case. 59
4.7 Tracking error for matrix parameter estimation case 60

5.1 Linear adaptive inverse control scheme. 63
5.2 Tracking error obtained with linear adaptive control method. 71
5.3 Evolution of parameter estimates for linear adaptive control 73
5.4 PID control formulation. 74
5.5 Open loop with partial inverse compensation 76
5.6 PID control with no inverse compensation 77
5.7 PID control with partial inverse compensation 77
5.8 PID control for a high frequency signal with partial inverse compensation 78
5.9 PID control with partial inverse compensation and sensor noise . . . 79
5.10 PID control with full inverse compensation 80
5.11 LQR control with exact inverse compensation 84
5.12 LQR control with full inverse compensation 85
5.13 LQR control with full inverse compensation and sensor noise 86

6.1 Two filter implementations for robust control design 88
6.2 Effects of the two filter implementations 89
6.3 Robust control design system incorporating error created by the inherent hysteresis and sensor noise in the transducer. 90
6.4 Linear fractional transformation (LFT) representation of the transducer model. 91
6.5 Frequency response of W_s and W_n. 95
6.6 Frequency response of W_r. 96
6.7 Power spectrum of d and frequency response of W_d for linear scaling factor. 97
6.8 Power spectrum of d and frequency response of W_d for inverse compensation based on free energy hysteresis model. 98
6.9 H_2 optimal control performance or a system with no hysteresis present 101
6.10 H_2 optimal control performance for a system with an error to the input of the plant which is not considered in the control design 102
6.11 H_2 optimal control results for a system employing a scaling factor . . 103
6.12 H_2 optimal control results for a system employing an inverse compensator 104
6.13 Sensitivity and disturbance sensitivity functions of H_2 control formulation 106
6.14 H_∞ optimal control results for a system employing an inverse compensator with no sensor noise 108
6.15 H_∞ optimal control results for a system employing an inverse compensator 109
6.16 Sensitivity and disturbance sensitivity functions of H_∞ control formulation 110
6.17 LFT for a general closed loop system. 112

6.18 System diagram for multiple objective system. 117
6.19 Equivalent system diagram for multiple objective system. 118
6.20 LFT for Terfenol-D system. 119
6.21 Optimal Q for multiobjective control with an H_2 objective function and an l_1 constraint 121
6.22 Performance of multiobjective control with an H_2 objective function and an l_1 constraint 122
6.23 Optimal Q for multiobjective control with an H_∞ objective function and an l_1 constraint 124
6.24 Performance of multiobjective control with an H_∞ objective function and an l_1 constraint 125
6.25 Optimal Q for multiobjective control with an H_2 objective function and an H_∞ and an l_1 constraint 126
6.26 Performance of multiobjective control with an H_2 objective function, and an H_∞ and an l_1 constraint 127

Chapter 1

Introduction

Smart materials are increasingly utilized for a variety of applications, including tunable lenses, modular antennas, atomic force microscopes, and high speed milling. Materials such as piezoceramics (PZT), magnetostrictives, and shape memory alloys (SMA) are appropriate for such applications because of their set point accuracy and high stress outputs. However, these materials exhibit hysteresis and constitutive nonlinearities which must be accommodated to achieve the performance specifications for high performance applications. At low frequencies and moderate drive levels, these effects can often be mitigated through feedback loops. At high drive levels or high frequencies, however, the hysteresis and nonlinear dynamics must be incorporated into models and subsequent control designs.

Figure 1.1a depicts the hysteretic relationship between applied magnetic fields and resulting magnetization exhibited by the magnetostrictive material Terfenol-D. To employ transducers exhibiting the nonlinear and hysteretic behavior illustrated in Figure 1.1a, the inherent hysteresis must be accommodated in the control design. If hysteresis in a smart material transducer is not accommodated, it can induce a phase delay in the response of the actuator. This phenomena is illustrated in Figure 1.1b for an open-loop simulation of a Terfenol-D transducer.

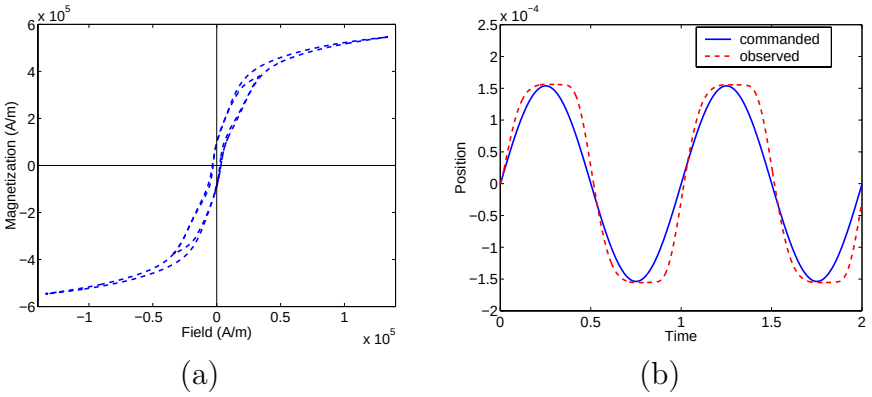

Figure 1.1: (a) Inherent hysteretic behavior, and (b) phase delay caused by the inherent hysteresis in a magnetostrictive material.

One method of attenuating the nonlinear and hysteretic behavior of these materials is to develop an inverse model. Once an inverse is derived from the hysteresis model, it may be employed as a filter to the input of the actuator in the control system, as depicted in Figure 1.2. This method requires a hysteresis model which allows an inverse that can be calculated in real-time. In Figure 1.2, the hysteretic actuator is represented by $H(s)$ and a linear plant is denoted by $P(s)$. The inverse compensator is denoted by $\widehat{H}^{-1}(s)$ and r is the desired position of the tip of the rod. In all of the control designs presented, some form of inverse compensation will be utilized.

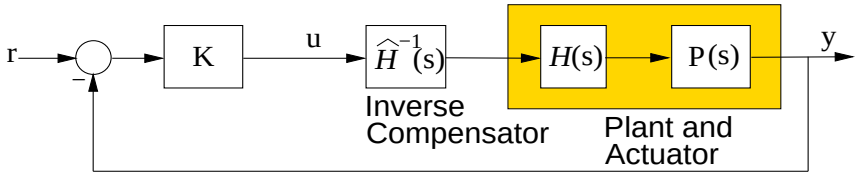

Figure 1.2: Control system incorporating inverse compensator method.

The models, which describe the nonlinearities and hysteresis for the smart materials, contain several material dependent parameters which must be identified in order to effectively utilize resulting inverse compensators. Additionally, material parameters in the models may slowly vary as a result of changes in the operating conditions such as temperature or creep. It is desirable to identify the material parameters during the operation of the transducer as opposed to applying off-line parameter estimation algorithms such as least square fits to data. A method capable of continuous or periodic estimation of nonlinearly occurring parameters in the hysteresis models ensures that the inverse compensators based on the hysteresis models continue to provide adequate attenuation of the hysteretic behavior in the smart system.

Once an inverse compensator has been designed and a method for identifying the material parameters in the transducer model has been developed, a control law must be designed to meet the given performance criteria. While forcing the smart transducer to track a reference signal is often the primary objective, it is beneficial to design the controller to be robust with respect to inherent disturbances in our system. For example, the models developed to describe the nonlinear and hysteretic behavior are not exact descriptions of the physical phenomena. Therefore, even with an inverse filter, we will not accommodate the nonlinear and hysteretic behavior entirely. The resulting error represents a disturbance to the input of the transducer. Furthermore, sensor noise is always present in the measurement of the transducer outputs. This must be attenuated so that the controller does not feedback on noise.

To focus the investigation, we consider a prototypical magnetostrictive actuator as illustrated in Figure 1.3. Terfenol-D is a magnetostrictive material which contains magnetic moment that rotate in response to an applied magnetic field. The rotation of moments induces a strain in the Terfenol-D, thereby causing a displacement in the tip of the rod. The magnetic field is applied by means of a current running through a

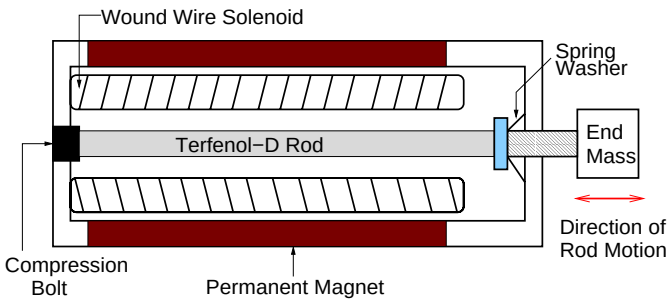

Figure 1.3: Prototypical magnetostrictive transducer.

wire solenoid. The magnetic field can be biased by the inclusion of a permanent magnet surrounding the Terfenol-D rod. This permanent magnet may also be designed to minimize the end effects of the magnetic field for reasons detailed in Chapter 3. The rod is fixed on one end and a spring washer is attached to the free end to provide a prestress. While the techniques in this dissertation are described in the context of a magnetostrictive transducer, they are sufficiently general to be applied to ferroelectrics as well as ferroelastics under certain conditions. This provides a unified approach to the control of many smart structures.

Three models quantifying the inherent hysteresis in magnetostrictive materials and their corresponding inverse compensators are summarized in Chapter 2. In Chapter 3, the hysteretic behavior of the magnetostrictive material is incorporated in the full model for the Terfenol-D transducer depicted in Figure 1.3. Under certain assumptions, it will be shown that the transducer can be modeled as a linear plant with a nonlinear hysteretic input. Chapter 4 describes a nonlinear adaptive parameter estimation algorithm capable of identifying nonlinearly occurring material parameters in the hysteresis models. The advantages and disadvantages of some preliminary control techniques utilizing inverse compensators are summarized in Chapter 5. The

deficiencies of the methods discussed in Chapter 5 motivates the investigation of robust control methods employing inverse compensations summarized in Chapter 6. A summary of the dissertation and directions for future work are stated in Chapter 7.

Chapter 2

Hysteresis Models

This chapter summarizes three constitutive models for hysteretic behavior in smart materials, namely a domain wall model, a Preisach model and a free energy model. Each model possesses benefits and drawbacks which will be noted during the discussion. While analogous models exist for ferroelectric and ferroelastic materials, the models here will be summarized in the context of magnetostrictive materials.

2.1 Domain Wall Model

In this section, we describe the domain wall model quantifying the hysteretic relationship between an applied magnetic field H and the magnetization M in a Terfenol-D rod. The premise of this model is that one source of hysteresis in ferromagnetic materials can be attributed to the impediment of motion of domain walls that are pinned at defects or inclusions in the material. A domain denotes a region where the magnetic moments have the same orientation and the domain walls are the transition areas between domains. Domain wall theory was developed for ferromagnetic materials by Jiles and Atherton [8] and extended to Terfenol-D transducers in [5]. Analogous theory was developed for ferroelectric materials in [20, 22] and ferroelastic compounds

in [21]. As illustrated in [21], this then provides a unified framework for quantifying constitutive nonlinearities and hysteresis in a broad class of ferroic compounds.

The development which follows is only an overview and much of the underlying physics will be omitted. For more detailed description of the domain wall theory, we refer the reader to [5].

The domain wall model for the magnetization produced by an imposed magnetic field will be developed in three steps; (i) quantification of the anhysteretic magnetization M_{an}, (ii) quantification of the irreversible magnetization M_{irr} and (iii) quantification of the total magnetization M.

Physically, M_{an} can be interpreted as the magnetization obtained when no inclusions or imperfections are present. As detailed in [8], the anhysteretic magnetization in the absence of applied stress is dependent on the effective field given by

$$H_e = H + \alpha M. \tag{2.1}$$

Here α quantifies the effects of the interdomain coupling.

Thermal and magnetostrictive energy are subsequently balanced using Boltzmann principles to specify the probability that a dipole will occupy a certain energy state. Under two different assumptions on the orientation of the dipoles, two models for the anhysteretic magnetization can be derived. Under the assumption that the dipole can only orient in the direction of or opposite to an applied field, the Ising spin relation

$$M_{an} = M_s \tanh\left(\frac{H_e}{a}\right) \tag{2.2}$$

is obtained. Here M_s is the saturation magnetostriction and a is a temperature dependent coefficient. If the dipoles have equal probability of orienting in any direction,

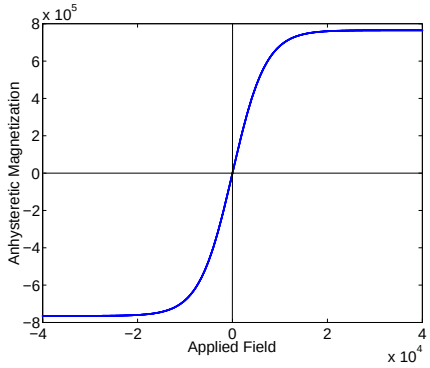

Figure 2.1: Ising spin model of anhysteretic magnetization.

we arrive at the Langevin model which is given as

$$M_{an} = M_s \left(\coth\left(\frac{H_e}{a}\right) - \frac{a}{H_e} \right). \tag{2.3}$$

Taylor expansion of these two expressions shows that they are equivalent through third order terms. The Ising model of the anhysteretic magnetization (2.2) is illustrated in Figure 2.1.

The anhysteretic relations can be utilized to model magnetization at low drive levels but do not include the energy loss due to the movement of domain walls and thus can not model high drive levels. To quantify the total magnetization, it is necessary to incorporate the reversible magnetization M_{rev} and the irreversible magnetization M_{irr}. Reversible magnetization occurs when applied field levels are sufficiently small that domain walls remain pinned while the irreversible component represents the movement of pinning sites which occurs at higher drive levels. Now, M_{irr} can be quantified as the anhysteretic component minus the loss required to break pinning sites:

$$M_{irr} = M_{an} - k\frac{\partial M_{irr}}{\partial H_e} \tag{2.4}$$

where k is a measure of the average energy required to translate a pinning site. This relation can be reformulated in terms of the applied field as

$$\frac{\partial M_{irr}}{\partial H} = \widehat{\delta}\frac{M_{an} - M_{irr}}{k\delta - \alpha(M_{an} - M_{irr})} \tag{2.5}$$

where $\delta = sign(dH)$ ensures that pinning opposes change in magnetization. The switch $\widehat{\delta}$ is 0 if $dH > 0$ and $M > M_{an}$ or $dH < 0$ and $M < M_{an}$ and 1 otherwise. This is necessary to model the physical observation that, after a field reversal, the changes in magnetization are purely reversible until the anhysteretic value is reached.

The reversible magnetization is given by the algebraic relationship

$$M_{rev} = c(M_{an} - M_{irr}) \tag{2.6}$$

where c is a material parameter which quantifies the reversibility of the material. The total magnetism is the sum of the reversible and irreversible magnetizations which yields

$$M = (1 - c)M_{irr} + cM_{an}. \tag{2.7}$$

The relation (2.7) can be reformulated as a differential equation

$$\frac{\partial M}{\partial H} = F(H, M) \tag{2.8}$$

$$M(H_0) = M_0$$

where

$$F(H, M) = \frac{1}{1 + c\alpha\frac{\partial}{\partial H}M_{an}}\left[\widehat{\delta}\frac{M_{an} - M}{k\delta - \widehat{\alpha}(M_{an} - M)} + c\frac{\partial}{\partial H}M_{an}\right] \tag{2.9}$$

with $\widehat{\alpha} = \dfrac{\alpha}{1 - c}$. The anhysteretic magnetization M_{an} can be taken as either the Ising model (2.2) or the Langevin model (2.3). The material parameters in the domain wall

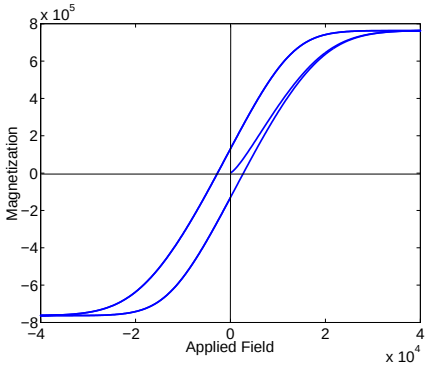

Figure 2.2: Domain wall model of magnetization.

model, which we will employ for the Terfenol-D sample, were estimated by a least squares fit to data as detailed in [5] and are given in Table 2.1. The domain wall model is illustrated in Figure 2.2.

2.1.1 Domain Wall Model Inverse

Since the domain wall hysteresis model can be formulated as a differential equation, the inverse can be formulated as a complementary differential equation as seen in [4, 16, 19]. The inverse of the domain wall hysteresis model is given as

$$\frac{\partial M^{-1}}{\partial H} = \frac{1}{F(M^{-1}, H)} \tag{2.10}$$

$$M^{-1}(H_0) = M_0^{-1} \ .$$

M_s	α	c	a	k
$7.65 \times 10^5 A/m$	-0.01	0.18	$7012 A/m$	$4000 A/m$

Table 2.1: Parameters for the domain wall model.

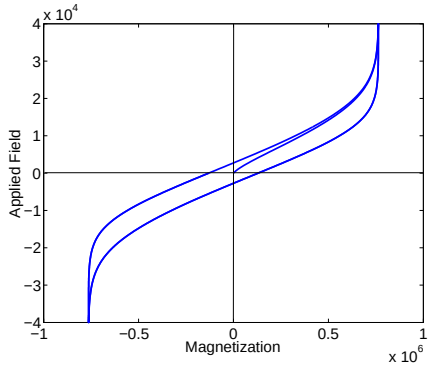

Figure 2.3: Inverse of the domain wall model given by (2.10).

The full inverse of the domain wall model is illustrated in Figure 2.3. Computing the full inverse of the domain wall model requires highly accurate initial conditions and is difficult to employ in a real-time control setting. These impediments motivate the introduction of a partial inverse which can be employed as a filter to attenuate the nonlinear effects of the Terfenol-D transducer in real-time. A partial inverse is formulated by inverting the anhysteretic component (2.2) or (2.3) of the magnetization. Because of the ease of inversion, we utilize the Ising model (2.2); which yields the partial inverse

$$[H(M)](t) = a \cdot \tanh^{-1}(M/M_s) - \alpha M. \tag{2.11}$$

The partial inverse is appropriate for control design because it can be implemented algebraically and therefore requires very little computation effort. Figure 2.4a depicts the partial inverse compensator. The partial inverse is able to attenuate much of the nonlinear behavior of the material but does not compensate for the inherent hysteresis. The effects of employing the partial inverse filter are illustrated in Figure 2.4b. If this partial inverse is employed in a control strategy, the control law must attenuate the phase delay due to uncompensated hysteresis to adequately track a reference signal.

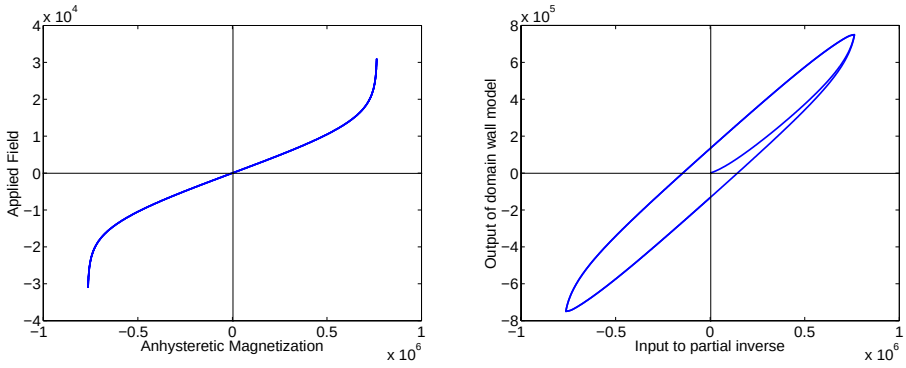

(a) (b)

Figure 2.4: (a) Partial inverse compensator, and (b) the effects of partial inverse compensation in reducing saturation nonlinearities.

2.2 Preisach Model

The second technique for qualifying hysteresis is based on a piecewise linear, generalized Preisach model. Preisach models suffer from the disadvantage that, because they are not based on energy formulations, they can have a large number of nonphysical parameters which are difficult to correlate with properties of the data. Furthermore, extensions to the theory must be employed to accommodate reversible effects, frequency dependencies and temperature dependencies. However, due to their rigorous mathematical foundations [1, 25], Preisach models lend transducers to the development of a linear adaptive control technique as will be discussed in Section 5.1. The model and a corresponding inverse model described in this section were developed by Tao and Kokotović (see [10, 11]).

The hysteresis model is parameterized by the constants m_t, c_t, m_b, c_b, m_r, c_r, m_l, c_l and the major loop can be described as two half lines

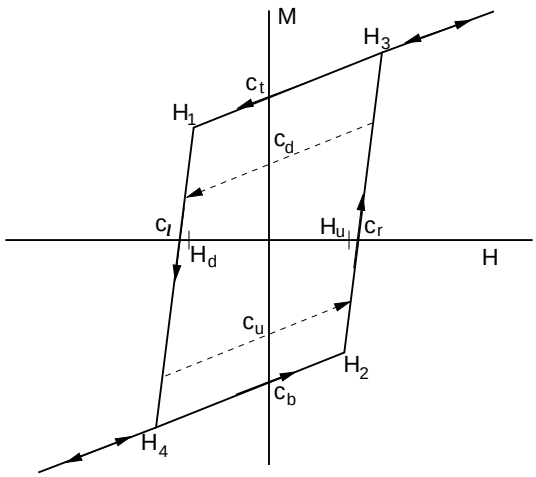

Figure 2.5: Preisach straight line hysteresis model.

$$\begin{aligned} M(t) &= m_t H(t) + c_t \quad \text{for } H(t) > H_1 = \frac{c_t + m_l c_l}{m_l - m_t} \\ M(t) &= m_b H(t) + c_b \quad \text{for } H(t) > H_2 = \frac{c_b + m_r c_r}{m_r - m_b} \end{aligned} \tag{2.12}$$

and two line segments

$$\begin{aligned} M(t) &= m_r(H(t) - c_r) \quad \text{for } H_2 \leq H(t) < H_3 = \frac{c_t + m_r c_r}{m_r - m_t} \\ M(t) &= m_l(H(t) - c_l) \quad \text{for } \frac{c_b + m_l c_l}{m_l - m_b} = H_4 < H(t) \leq H_1 \end{aligned} \tag{2.13}$$

where $H(t)$ is the applied magnetic field and $M(t)$ is the resulting magnetization. While the model is sufficiently general to accommodate asymmetric hysteresis, the hysteretic behavior of the Terfenol-D transducer is symmetric, therefore $m_t = m_b,\ c_t = -c_b,\ m_r = m_l$ and $c_r = -c_l$. Periodically throughout the model description, simplifications in the model due to symmetry will be noted. The Preisach straight line model is depicted in Figure 2.5.

The value of the time derivatives of $M(t)$ and $H(t)$ are constant along the two line segments. For example, $\dot{H} > 0$ and $\dot{M} > 0$ for the segment $M(t) = m_r(H(t) - c_r)$ and $\dot{H} < 0$ and $\dot{M} < 0$ for the segment $M(t) = m_l(H(t) - c_l)$. Similarly, on the half line $M(t) = m_t H(t) + c_t$, $\dot{H} < 0$ and $\dot{M} < 0$ if $H(t) < H_3$ but $\dot{H}$ and $\dot{M}$ need only be the same sign if $H(t) > H_3$. For the half line $M(t) = m_b H(t) + c_b, \dot{H} > 0$ and $\dot{M} > 0$ if $H(t) > H_1$ but $\dot{H}$ and $\dot{M}$ need only be the same sign if $H(t) < H_1$.

A situation which arises that has yet to be modeled is if $\dot{H}$ changes sign before a 'corner'. This forces an inner loop in the hysteresis as depicted by the dashed lines in Figure 2.5. The inner loop can be described as

$$\begin{aligned} M(t) &= m_t H(t) + c_d(t) \quad \text{for} \quad \dot{H} < 0 \\ M(t) &= m_b H(t) + c_u(t) \quad \text{for} \quad \dot{H} > 0 \end{aligned} \tag{2.14}$$

where $c_d(t)$ and $c_u(t)$ are the turning points for the downward and upward inner loop segments, respectively.

While the model can be stated as a continuous time model, to facilitate the description of the hysteresis output we shall consider the discretization of the continuous system. This is reasonable as the model must be implemented discretely. The turning points can be quantified as

$$\begin{aligned} c_d(t_k) &= M(t_{k-1}) - m_t H(t_k) \\ c_u(t_k) &= M(t_{k-1}) - m_b H(t_k). \end{aligned} \tag{2.15}$$

For a symmetric hysteresis, $c_d = c_u$.

Next, we define the 'H' coordinates of the start of an inner loop as

$$H_d = \frac{m_l c_l + c_d}{m_l - m_t}, \qquad H_u = \frac{m_r c_r + c_u}{m_r - m_b} \tag{2.16}$$

where $H_4 \leq H_d \leq H_u \leq H_3$. The Presiach hysteresis model can now be defined as

$$M(t_k) = \begin{cases} M(t_{k-1}), & \text{if } H(t_k) = H(t_{k-1}) \\ m_t H(t_k) + c_t, & \text{if } H(t_k) \geq H_3, \text{ or if } m_t < m_b, \\ & M(t_{k-1}) = m_t H(t_{k-1}) + c_t \\ & \text{and } H(t_{k-1}) < H(t_k) < H_3 \\ m_b H(t_k) + c_b, & \text{if } H(t_k) \leq H_4 \text{ or if } m_t > m_b, \\ & M(t_{k-1}) = m_b H(t_{k-1}) + c_b \\ & \text{and } H_4 < H(t_k) < H(t_{k-1}) \\ m_t H(t_k) + c_d, & \text{if } H_d < H(t_k) < H(t_{k-1}) \\ m_b H(t_k) + c_u, & \text{if } H(t_{k-1}) < H(t_k) < H_u \\ m_l (H(t_k) - c_l), & \text{if } H_d \geq H(t_k) \geq H_4 \\ m_r (H(t_k) - c_r), & \text{if } H_u \leq H(t_k) \leq H_3 \ . \end{cases} \tag{2.17}$$

One concern in the above model is the definition of the inner loops. The values of c_d, c_u, H_d and H_u must be calculated if $\dot{H}$ changes sign before a 'corner' and the input signal must be examined relative to H_d and H_u to determine the output of the hysteresis model. The material parameters for the Terfenol-D sample in the Preisach straight line hysteresis model are given in Table 2.2. The parameters employed in the Preisach model were identified by fitting the Preisach model to the domain wall model (2.8) employing the parameters given in Table 2.1. A comparison of the Preisach model and the domain wall model can be seen in Figure 2.6.

$m_t = m_b$	$c_t = -c_b$	$m_r = m_l$	$c_r = -c_l$
1.48	7.1 $\times 10^5$	41.82	3.14 $\times 10^3$

Table 2.2: Parameters for the Preisach model.

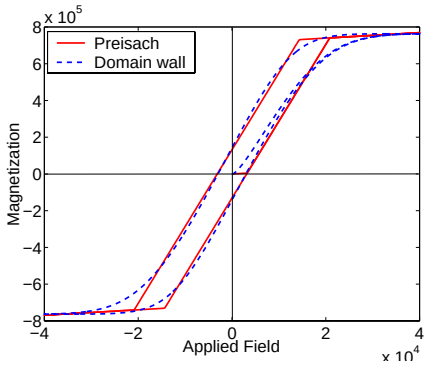

Figure 2.6: Comparison of Preisach model and domain wall model.

2.2.1 Preisach Inverse

An inverse of the Preisach straight line can be constructed in order to cancel the effects of the hysteresis (see [10, 11]). To construct an exact inverse, the model would again be parameterized by $m_t, c_t, m_b, c_b, m_r, c_r, m_l$, and c_l, but as we are developing this inverse to be utilized as a compensator in a linear adaptive control algorithm, it is advantageous to develop a tunable approximate inverse parameterized by $\widehat{m}_t(t)$, $\widehat{c}_t(t)$, $\widehat{m}_b(t)$, $\widehat{c}_b(t)$, $\widehat{m}_r(t)$, $\widehat{c}_r(t)$, $\widehat{m}_l(t)$, and $\widehat{c}_l(t)$. This approximate inverse converges to the exact inverse as the parameter estimates converge to the exact parameters of the hysteresis model. For the remainder of the model development, we will denote $\widehat{m}_*(t)$ as $\widehat{m}_*$.

We denote the input to the approximate hysteresis inverse model as $M_d(t)$ and the output as $H(t)$. Proceeding in the manner used when constructing the hysteresis model, the approximate inverse can be defined by two half lines

$$\begin{aligned} H(t) &= \frac{1}{\widehat{m}_t}(M_d(t) - \widehat{c}_t), \text{ for } M_d(t) > M_1 = \frac{\widehat{m}_l(\widehat{m}_t\widehat{c}_t + \widehat{c}_t)}{\widehat{m}_l - \widehat{m}_t} \\ H(t) &= \frac{1}{\widehat{m}_b}(M_d(t) - \widehat{c}_b), \text{ for } M_d(t) < M_2 = \frac{\widehat{m}_r(\widehat{m}_b\widehat{c}_r + \widehat{c}_b)}{\widehat{m}_r - \widehat{m}_b} \end{aligned} \tag{2.18}$$

and two line segments

$$\begin{aligned} H(t) &= \frac{1}{\widehat{m}_r} M_d(t) + \widehat{c}_r, \text{ for } M_2 \leq M_d(t) \leq M_3 = \frac{\widehat{m}_r(\widehat{m}_t\widehat{c}_r + \widehat{c}_t)}{\widehat{m}_r - \widehat{m}_t} \\ H(t) &= \frac{1}{\widehat{m}_l} M_d(t) + \widehat{c}_l, \text{ for } \frac{\widehat{m}_l(\widehat{m}_b\widehat{c}_l + \widehat{c}_b)}{\widehat{m}_l - \widehat{m}_b} = M_4 < M_d(t) \leq M_1. \end{aligned} \tag{2.19}$$

The approximate hysteresis inverse has conditions on the derivatives of M_d and H similar to the hysteresis model. For example, $\dot{M}_d > 0$ and $\dot{H} > 0$ for $H(t) = \frac{1}{\widehat{m}_r} M_d(t) + \widehat{c}_r$ and $\dot{M}_d < 0$ and $\dot{H} < 0$ for $H(t) = \frac{1}{\widehat{m}_l} M_d(t) + \widehat{c}_l$. For $H(t) = \frac{1}{\widehat{m}_t}(M_d(t) - \widehat{c}_t)$, $\dot{M}_d < 0$ and $\dot{H} < 0$ if $M_d(t) < M_1$. If $M_d(t) > M_1$ the derivatives need only have the same sign. A similar result is true of the other half line as depicted in Figure 2.7.

Again we define the discrete form of the model for implementation purposes. To keep track of an inner loop, we define

$$\begin{aligned} \widehat{c}_d(t_k) &= M_d(t) - \widehat{m}_t H(t_{k-1}) \\ \widehat{c}_u(t_k) &= M_d(t_{k-1}) - \widehat{m}_b H(t_{k-1}) \end{aligned} \tag{2.20}$$

which are the 'M_d' intercepts for the inner loops. For the symmetric case, $\widehat{m}_t = \widehat{m}_b$ thus $\widehat{c}_u$ is redundant. Now define

$$M_{dr}(t_k) = \begin{cases} \dfrac{\widehat{m}_r(\widehat{m}_t\widehat{c}_r + \widehat{c}_d)}{\widehat{m}_r - \widehat{m}_t}, & \text{if } M_d(t_{k-1}) > M_d(t_k) \\ \dfrac{\widehat{m}_r(\widehat{m}_b\widehat{c}_r + \widehat{c}_u)}{\widehat{m}_r - \widehat{m}_b}, & \text{if } M_d(t_{k-1}) < M_d(t_k) \end{cases} \tag{2.21}$$

$$M_{dl}(t_k) = \begin{cases} \dfrac{\widehat{m}_l(\widehat{m}_t\widehat{c}_l + \widehat{c}_d)}{\widehat{m}_l - \widehat{m}_t} & \text{if } M_d(t_{k-1}) > M_d(t_k) \\ \dfrac{\widehat{m}_l(\widehat{m}_b\widehat{c}_l + \widehat{c}_M)}{\widehat{m}_l - \widehat{m}_b} & \text{if } M_d(t_{k-1}) < M_d(t_k) \end{cases} \tag{2.22}$$

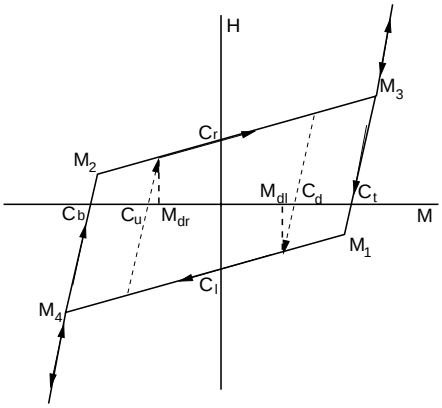

Figure 2.7: Approximate hysteresis inverse model.

which are the points where the inner loop begins. Again, we could simplify the expression by invoking symmetry properties.

The discrete inverse Preisach hysteresis model for a given input $M_d(t_k)$ and resulting output $H(t_k)$ is then given by

$$H(t_k) = \begin{cases} H(t_{k-1}), & \text{if } M_d(t_k) = M_d(t_{k-1}) \\ \dfrac{1}{\widehat{m}_t}(M_d(t_k) - \widehat{c}_t), & \text{if } M_d(t_k) \geq M_3 \\ \dfrac{1}{\widehat{m}_b}(M_d(t_k) - \widehat{c}_b), & \text{if } M_d(t_k) \leq M_4 \\ \dfrac{1}{\widehat{m}_r}M_d(t_k) + \widehat{c}_r, & \text{if } M_3 \geq M_d(t_k) \geq M_{dr} \\ \dfrac{1}{\widehat{m}_l}M_d(t_k) + \widehat{c}_l, & \text{if } M_4 \leq M_d(t_k) \leq M_{dl} \\ \dfrac{1}{\widehat{m}_t}(M_d(t_k) - \widehat{c}_d), & \text{if } M_{dl} < M_d(t_k) < M_{dr} \\ & \quad \text{and } M_d(t_{k-1}) > M_d(t_k) \\ \dfrac{1}{\widehat{m}_t}(M_d(t_k) - \widehat{c}_u), & \text{if } M_{dl} < M_d(t_k) < M_{dr} \\ & \quad \text{and } M_d(t_{k-1}) < M_d(t_k). \end{cases} \tag{2.23}$$

2.3 Free Energy Model

In this section a free energy model for the hysteretic relationship between an applied magnetic field and the resulting magnetization inherent in the Terfenol-D transducer is summarized. For a more detailed development of this model see [18, 21]. A major benefit of this model over the domain wall and straight line Preisach models is its ability to predict biased minor loops efficiently and accurately. Since we will be applying feedback control methods to the Terfenol-D transducer, we often have no *a priori* knowledge of the signal to be input into the transducer. Therefore, it is advantageous to be able to model biased inner loops accurately. While the domain wall model can predict symmetric inner loops it does not model biased inner loops as accurately as the free energy model. The straight line Preisach model also does a poor job of modeling biased inner loops. While classical Preisach models provide the capability for accurately quantifying minor loop behavior, this accuracy typically comes at the price of increased computational complexity.

The free energy model is based on the quantification of energy required to reorient dipoles in combination with stochastic homogenization techniques to accommodate variations in coercive and effective fields. The model summarized here assumes that there is very little change in the operating temperature and, therefore, we treat the temperature as fixed. The model also ignores losses due to eddy currents and, therefore, should be employed for low frequency drive levels.

A further assumption is that the spring washer in the transducer illustrated in Figure 1.3 provides sufficient prestress to dominate the crystal anisotropies in the Terfenol-D. Much like the domain wall model, the free energy formulation asserts that the rotation of magnetic moments in the magnetostrictive material is impeded by polycrystallinity and imperfections in the material. As a consequence, the magnetic moments do not rotate uniformly causing the nonlinear hysteretic behavior.

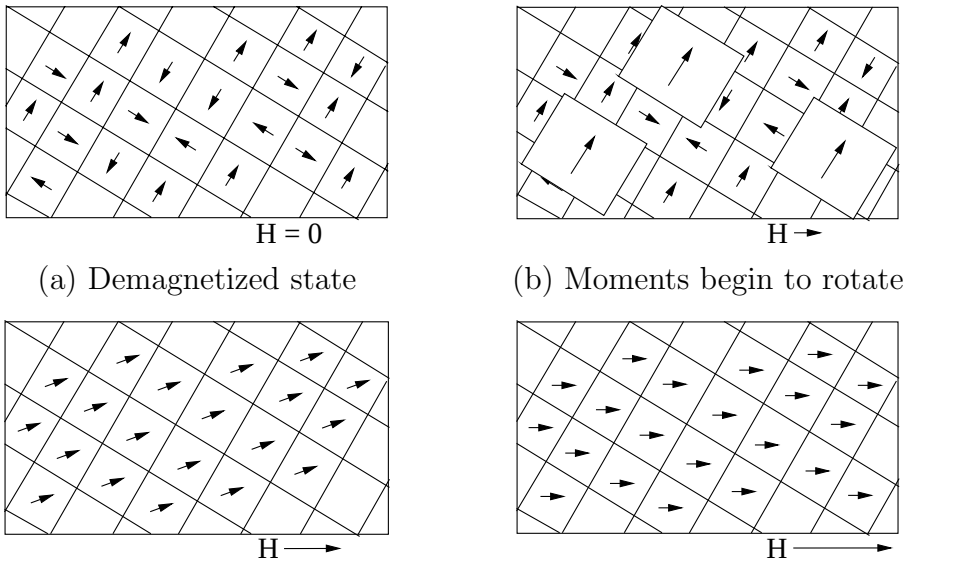

(a) Demagnetized state (b) Moments begin to rotate

(c) Moments rotate to easy axis (d) Moments rotate to align with field

Figure 2.8: For no applied field the magnetostrictive material is in a (a) demagnetized state, as the field increases (b) domains grow as moments being to rotate. For a certain field level (c) all of the moments align with the easy axis and then, for further increase in the applied field, (d) the moments rotate to align with the field.

Figure 2.8 illustrates the progression of magnetization due to an applied magnetic field.

We first consider the Helmholtz energy which incorporates the internal energy due to the interaction of moments. The model assumes that the moments have two preferred orientation, namely in the direction of the stress-induced easy axis of the Terfenol-D crystal and against it. Therefore, a double well potential can be employed to approximate the Helmholtz free energy. Again, we are assuming isothermal conditions, that crystalline anisotropies are negligible and that we are operating in the ferromagnetic regime. Under these assumptions, statistical mechanics analysis [21] indicates that a first order approximation to the potential behaves quadratically in the neighborhood of the three equilibria. Therefore, we can formulate the Helmholtz

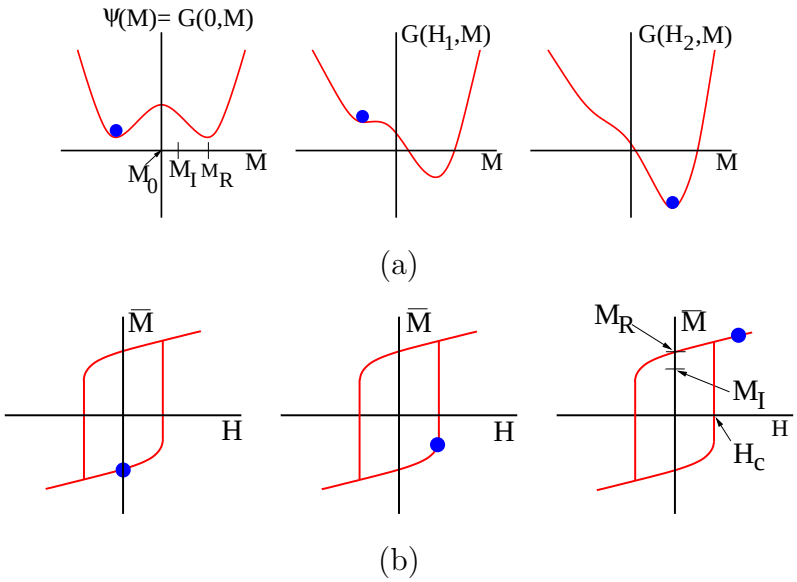

Figure 2.9: (a) Gibbs energy G, and the corresponding (b) local magnetization $\overline{M}$ for increasing field H.

free energy as

$$\psi(M) = \begin{cases} \frac{1}{2}\eta(M + M_R)^2, & M \leq -M_I \\ \frac{1}{2}\eta(M - M_R)^2, & M \geq M_I \\ \frac{1}{2}\eta(M_I - M_R)\left(\frac{M^2}{M_I} - M_R\right), & |M| < M_I. \end{cases} \tag{2.24}$$

As depicted in Figure 2.9, M_R and M_I respectively denote the point at which the minimum of ψ occurs and the inflection point.

For an applied magnetic field H the Gibbs energy is given as

$$G = \psi - HM. \tag{2.25}$$

Note that the magnetostatic energy is given as $\varepsilon = \mu_0 HM$ where μ_0 denotes the magnetic permeability. The Gibbs free energy given in (2.25) can be interpreted as incorporating μ_0 into ψ for simplicity.

For a homogeneous material with the effective field taken as the applied field, the local average magnetization is given by

$$\overline{M} = x_+\langle M_+\rangle + x_-\langle M_-\rangle \tag{2.26}$$

where x_+ and x_- denote the fraction of moments having positive and negative orientations, respectively. We denote the expected values of the magnetization for moments having positive and negative orientations as $\langle M_+\rangle$ and $\langle M_-\rangle$, respectively. We can quantify $\langle M_+\rangle$ and $\langle M_-\rangle$ by

$$\langle M_+\rangle = \frac{\int_{M_0}^{\infty} M e^{-G(H,M)V/kT}\, dM}{\int_{M_0}^{\infty} e^{-G(H,M)V/kT}\, dM}, \quad \langle M_-\rangle = \frac{\int_{-\infty}^{M_0} M e^{-G(H,M)V/kT}\, dM}{\int_{-\infty}^{M_0} e^{-G(H,M)V/kT}\, dM}. \tag{2.27}$$

Here $e^{-G(H,M)V/kT}$ represents the probability of obtaining an energy level G and the denominator of (2.27) assures that the probability of integrating over all possible magnetization values is 1. Here, M_0 denotes the unstable equilibrium (see Figure 2.9), V is the lattice volume, k is Boltzman's constant and T is the temperature. For implementation, M_I can replace M_0. This simplifies the approximation of the integrals and is reasonable since the maximum restoring force occurs at M_I and $-M_I$. Also if the thermal activation is reduced to zero the infection points and the unstable equilibria coincide (see [18]).

The moment fractions satisfy the evolution equations

$$\begin{aligned} \dot{x}_+ &= -p_{+-}x_+ + p_{-+}x_- \\ \dot{x}_- &= -p_{-+}x_- + p_{+-}x_+ \end{aligned} \tag{2.28}$$

where p_{+-} and p_{-+} are the likelihoods of switching from positive to negative orientation and switching from negative to positive orientation, respectively. They are given as

$$p_{+-} = \sqrt{\frac{kT}{2\pi m}} \frac{e^{-G(H,M_0)V/kT}}{\int_{M_0}^{\infty} e^{-G(H,M)V/kT} dM} \tag{2.29}$$

$$p_{-+} = \sqrt{\frac{kT}{2\pi m}} \frac{e^{-G(H,-M_0)V/kT}}{\int_{-\infty}^{-M_0} e^{-G(H,M)V/kT} dM} \tag{2.30}$$

where m is the mass of lattice volume V. The relation between the applied field H and the magnetization M exhibits both hysteresis and nonlinear transition because the local magnetization (2.26) is probabilistic. The steepness of the transition depends on the ratio of GV to kT.

For operating regimes in which thermally activated relaxation processes are negligible, we can employ the asymptotic analysis from [18] to obtain an algebraic formulation for the local average magnetization. From the equilibrium condition $\dfrac{\partial G}{\partial M} = 0$, we note immediately that $H = \dfrac{\partial \psi}{\partial M}$. Therefore, the local model predicts a linear relationship between H and $\overline{M}$ with a slope of $\frac{1}{\eta}$. The local magnetization in this limiting case is give as

$$[\overline{M}(H; H_c, \xi)](t) = \begin{cases} [\overline{M}(H; H_c, \xi)](0), & \tau(t) = \emptyset \\ \frac{H}{\eta} - M_R, & \tau(t) \neq \emptyset \text{ and } H(\max \tau(t)) = -H_c \\ \frac{H}{\eta} + M_R, & \tau(t) \neq \emptyset \text{ and } H(\max \tau(t)) = H_c \end{cases} \tag{2.31}$$

where the transition points are specified as

$$\tau(t) = \{t \in (0, T_f] \mid H(t) = -H_c \text{ or } H(t) = H_c\} \tag{2.32}$$

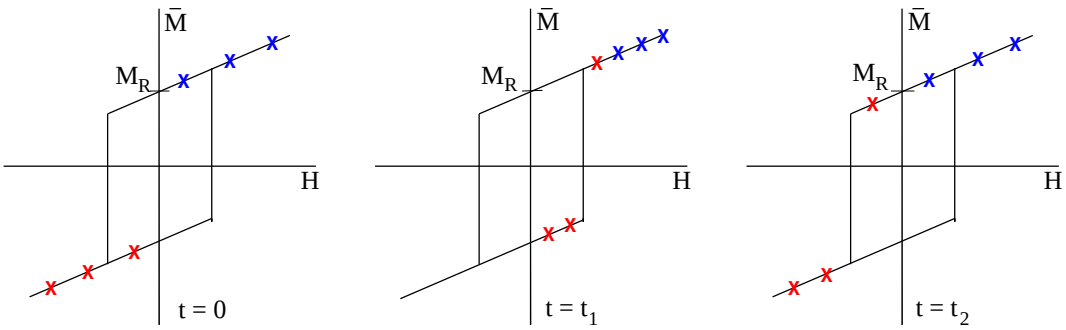

Figure 2.10: Varying field levels for the limiting case local average magnetization $\overline{M}$.

and the initial moment orientation is given as

$$[\overline{M}(H;H_c,\xi)](0) = \begin{cases} \frac{H}{\eta} - M_R, & H(0) \le -H_c \\ \xi, & -H_c < H(0) < H_c \\ \frac{H}{\eta} + M_R, & H(0) \ge H_c \ . \end{cases} \tag{2.33}$$

Here ξ denotes the initial magnetization of the points with field levels between $-H_c$ and H_c. The progression of several points in the limiting case definition is illustrated in Figure 2.10.

In the previous discussion, we have assumed that the lattice structure is homogeneous and hence the domain structure is homogeneous. This implies that the free energy profiles for the different regions of the Terfenol-D are identical. This assumption is overly simple since it ignores material defects, polycrystallinity and nonuniformities in the crystals. Also, the model assumed that the effective field at the domain level is the same as the applied field. To remedy these over-simplifications, the model incorporates stochastic distributions to develop a bulk magnetization model for a nonhomogeneous Terfenol-D sample with nonconstant effective fields.

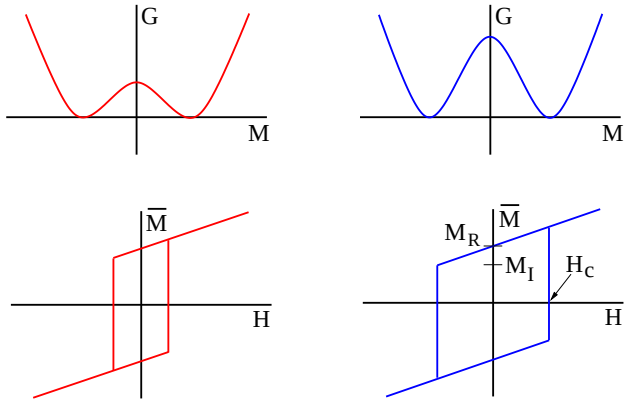

Figure 2.11: Free energy variations for a nonhomogeneous domain structure and the resulting variations in the local coercive field H_c.

We shall begin by summarizing the inclusion of a distribution of free energy profiles to accommodate material nonhomogeneities as developed in [18] and depicted in Figure 2.11. The nonhomogeneities are included by assuming the parameters M_R and M_I, or equivalently $H_c = \eta(M_R - M_I)$, satisfy a normal distribution with mean $\overline{H}_c$. The total magnetization can then be given as

$$M(H) = \int_0^\infty \overline{M}(H; H_c, \xi) f(H_c)\, dH_c \tag{2.34}$$

with density

$$f(H_c) = C_1 e^{-(H_c - \overline{H}_c)^2/b}. \tag{2.35}$$

The parameters C_1 and b are positive and $\overline{M}$ is given by (2.26) or (2.31).

The second extension entails the incorporation of variations in the effective field. In the domain wall model, the effective field H_e given by (2.1) was assumed to have a constant interaction coefficient. However, in the free energy model the effective field is assumed to be normally distributed with mean $\mathcal{H}$. Therefore, for a fixed coercive

$\mathcal{H}$	$300A/m$	η	14
$\overline{H}_c$	$7 \times 10^4 A/m$	M_R	$3.7 \times 10^4 A/m$
b	$1 \times 10^8 A^2/m^2$	C_1	6×10^{-4}
$\overline{b}$	$8 \times 10^8 A^2/m^2$	C_2	4.2×10^{-5}

Table 2.3: Parameters for the free energy model.

field, the magnetization can be given as

$$M(H) = \int_{-\infty}^{\infty} \overline{M}(H; H_c, \xi) C_2 e^{-(H-\mathcal{H})^2/\overline{b}} d\mathcal{H} dH_c. \tag{2.36}$$

Combining coercive field and effective field distributions for the full magnetization of a nonhomogeneous polycrystalline sample of Terfenol-D with variable effective fields yields the magnetization model

$$M(H) = C \int_0^{\infty} \int_{-\infty}^{\infty} [\overline{M}(\mathcal{H} + H; H_c, \xi)](t) e^{\mathcal{H}^2} e^{-(H_c - \overline{H}_c)^2/b} d\mathcal{H} dH_c. \tag{2.37}$$

The model is sufficiently simple to allow the possibility of real time implementation and has a relatively low number of material dependent parameters. The material parameters for the Terfenol-D sample are given in Table 2.3. These parameters were estimated through a least squares fit to high drive level data in [18] and the free energy model is shown against physical data collected from a Terfenol-D sample in Figure 2.12. It is evident from this figure that the free energy hysteresis model provides an accurate description of the inherent hysteresis in a magnetostrictive material including biased minor loop behavior and saturation nonlinearities.

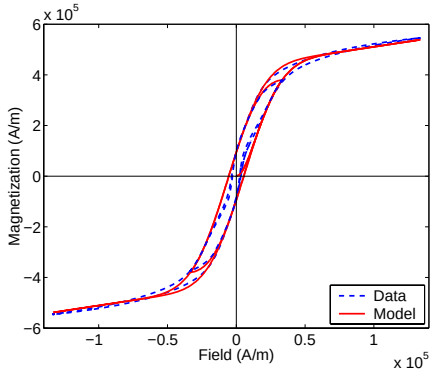

Figure 2.12: Validation of the free energy hysteresis model against Terfenol-D data.

2.3.1 Free Energy Model Implementation Algorithm

For numerical implementation of the free energy hysteresis model, the distributions for the effective field and coercive field are evaluated using a composite quadrature rule. Because of the exponential decay of the distributions, they can be truncated to speed computation. Applying a quadrature method, equation (2.37) can be approximated by

$$[M(H)](t) = C \sum_{i=1}^{N_i} \sum_{j=1}^{N_j} \left[\overline{M}\left(\mathcal{H}_j + H; H_{c_i}, \xi_i\right)\right](t) e^{\mathcal{H}_j^2/\overline{b}} e^{-(H_{c_i} - \overline{H}_c)^2/b} v_i w_j \tag{2.38}$$

where the abscissas are denoted $\mathcal{H}_j$ and H_{c_i} and v_i and w_j are the corresponding quadrature weights. For $H = 0$ and $M = 0$, the initial moment distribution ξ_i correspond to the quadrature points. An equivalent method to (2.31) to determine whether the effective field value $\mathcal{H}_j$ has switched with respect to the coercive field value H_{c_i} is to specify the local magnetization as

$$\overline{M} = \frac{H}{\eta} + M_R \Delta \tag{2.39}$$

where $\Delta = 1$ if evaluating on the upper branch of the limiting case magnetization (2.31) and $\Delta = -1$ if evaluating on the lower branch. For the approximation (2.38), Δ is a $N_i \times N_j$ matrix whose ijth component specifies whether $\mathcal{H}_j$ has reached H_{c_i}.

To state the numerical algorithm for determining the magnetization, we define the following the weight vectors

$$W^T = \left[w_1 e^{-\mathcal{H}_1^2/\overline{b}}, \cdots, w_{N_j} e^{-\mathcal{H}_{N_j}^2/\overline{b}} \right]_{1 \times N_j}$$

$$V^T = \left[v_1 e^{-(H_{c_i} - \overline{H}_c)^2/b}, \cdots, v_{N_i} e^{-(H_{c_{N_i}} - \overline{H}_c)^2/b} \right]_{1 \times N_i}.$$

We also define the matrices

$$\Delta_{init} = \begin{bmatrix} -1 & \cdots & 1 & 1 & \cdots & 1 \\ \vdots & & \vdots & \vdots & & \vdots \\ -1 & \cdots & 1 & 1 & \cdots & 1 \end{bmatrix}_{N_i \times N_j} \qquad \mathcal{H}_c = \begin{bmatrix} H_{c_1} & \cdots & H_{c_1} \\ \vdots & & \vdots \\ H_{c_{N_i}} & \cdots & H_{c_{N_i}} \end{bmatrix}_{N_i \times N_j}$$

$$\mathcal{H}_k = \begin{bmatrix} H_k + \mathcal{H}_1 & \cdots & H_k + \mathcal{H}_{N_j} \\ \vdots & & \vdots \\ H_k + \mathcal{H}_1 & \cdots & H_k + \mathcal{H}_{N_j} \end{bmatrix}_{N_i \times N_j} \qquad \mathcal{O} = \begin{bmatrix} 1 & \cdots & 1 \\ \vdots & & \vdots \\ 1 & \cdots & 1 \end{bmatrix}_{N_i \times N_j}$$

where $H_k = H(t_k)$ is the kth applied field value. Denoting the magnetization value $M_k \approx M(H_k)$, we give the following algorithm for the implementation of the free energy model.

Algorithm 1.

$$
\begin{aligned}
&\Delta = \Delta_{init} \\
&\widehat{M} = M_R\mathcal{O} + \tfrac{1}{\eta}H_c \\
&\text{for } k = 1 : N_k \\
&\quad \overline{M} = \tfrac{1}{\eta}\mathcal{H}_k + M_R\Delta \\
&\quad dH = H_k - H_{k-1} \\
&\quad \text{if } dE > 0 \\
&\qquad \Delta = \text{sign}(\mathcal{H}_k - H_c).*(\overline{M} - \widehat{M}).*\overline{M} \\
&\quad \text{else} \\
&\qquad \Delta = \text{sign}(\mathcal{H}_k + H_c).*(\overline{M} + \widehat{M}).*\overline{M} \\
&\quad \text{end} \quad \overline{M} = \tfrac{1}{\eta}\mathcal{H}_k + M_R\Delta \\
&\quad M_k = CW^T\overline{M}V \\
&\text{end}
\end{aligned}
\tag{2.40}
$$

Here $.*$ denotes componentwise matrix multiplication.

2.3.2 Inverse Energy Hysteresis Model

To construct an inverse compensator, the monotonicity of the hysteresis model is exploited. To determine the magnetic field required to create a desired magnetization, the hysteresis model is advanced until the desired magnetization is surpassed. Then the magnetic field is computed by a linear interpolation between the last two points. The computational speed of the inverse compensator depends on the size of the step taken in advancing the hysteresis model. Larger steps will increase the speed while decreasing the accuracy of the inverse compensator. To facilitate real time control, a larger step size is desired therefore the control method must be designed to reject a significant amount of error in the linearization of the hysteresis.

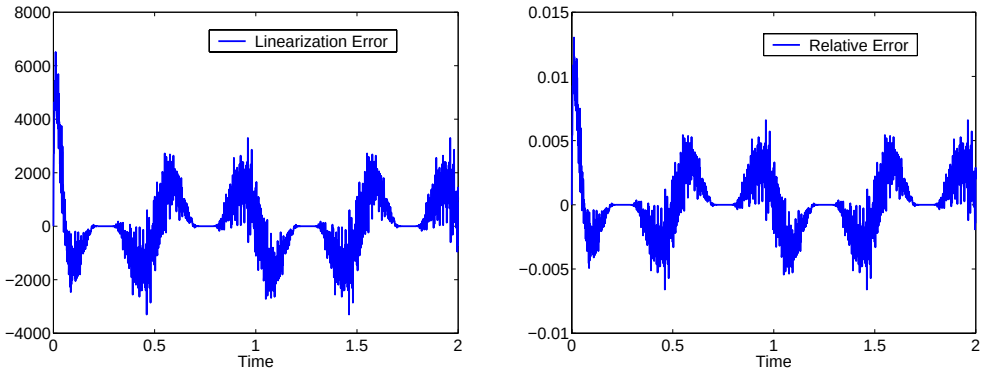

(a) (b)

Figure 2.13: (a) Hysteresis linearization error and (b) relative error.

The linearization error for an input signal with a frequency of 1 Hz and a step size of $\Delta H = 1$ employed in the inverse model is plotted in Figure 2.13a. While the error appears quite large, the relative error, illustrated in Figure 2.13b, is reasonable. Any control design utilizing the free energy model inverse as a filter must be able to reject this error to the input of the plant.

2.4 Concluding Remarks

This chapter summarized three models for the hysteretic behavior displayed by magnetostrictive materials and inverse compensators for each model. Although the models presented were developed to describe the inherent hysteresis in magnetostrictives, all of the modeling techniques can be applied to several smart materials including piezoceramics and, under certain conditions, shape memory alloys. The domain wall model quantifies the energy required to rotate magnetic moments in the material and assumes that one source of hysteresis is the impediment of motion of the moment caused by domain walls. This model provides an accurate description of major loop

behavior and of symmetric minor loop behavior but lack the ability to accurately predict biased minor loop behavior in magnetostrictives. While the implementation of the full inverse of the domain wall hysteresis model is difficult in real time, a partial inverse can be constructed by inverting the anhysteretic component of the model.

The next model discussed is a straight line Preisach hysteresis model and the corresponding inverse. The model is based on a linear kernel and therefore cannot incorporate the nonlinearities displayed by magnetostrictive materials. One benefit of this model is that its linear structure lends it to development of a linear adaptive control technique described in Section 5.1.

The third, and most accurate model described, quantifies the energy required to reorient the moments in the magnetostrictive material. This model utilizes stochastic homogenization techniques to accommodate variation in coercive and effective fields. Employing quadrature approximations, the model can be implemented algebraically and from this implementation algorithm an inverse compensator can be developed.

Chapter 3

Full Transducer Model

The three models developed in the previous section quantify the hysteretic relationship between an applied magnetic field and the resulting magnetization for a magnetostrictive material. In this section, the strains, forces and displacements generated by the changes in magnetization for a prototypical magnetostrictive transducer, illustrated in Figure 1.3, are quantified.

3.1 Rod Dynamics

In the previous chapter, models for the relationship between the applied field H and the magnetization M in a magnetostrictive material were described. However, the magnetoelastic coupling which provides these materials with magnetostrictive properties was not addressed. In applications where stress anisotropies dominate crystalline anisotropies, experimental evidence suggests there is a quadratic dependence of strain on magnetization. This can be quantified, as detailed in [18], by the incorporation of magnetoelastic coupling in the Helmholtz free energy relation

$$\psi_e(M, e) = \psi(M) + \frac{1}{2}Ye^2 - Y\gamma eM^2 \tag{3.1}$$

and the corresponding Gibbs energy relation

$$G(H, M, e) = \psi(M) + \frac{1}{2}Ye^2 - Y\gamma eM^2 - HM - \sigma e \tag{3.2}$$

where Y is the Young's modulus, $\psi(M)$ is given by (2.24) and γ is magnetoelastic coupling coefficient. The equilibrium condition $\dfrac{\partial G}{\partial e} = 0$ is utilized to determine the elastic constitutive relation

$$\sigma = Ye - Y\gamma M^2. \tag{3.3}$$

This relationship quantifies the linear relationship between stresses σ and strains e in the Terfenol-D rod as well as the nonlinear hysteretic dependence of the stress on applied fields H through the magnetization M. The magnetization may be modeled by either the domain wall hysteresis model (2.8), the straight line Preisach model (2.17) or the free energy hysteresis model (2.37).

The left end of the Terfenol-D rod ($x = 0$) is assumed to be fixed while the other end ($x = L$) is constrained by a damped oscillator and has a point mass attached, as depicted in Figure 3.1. The Kelvin-Voigt damping coefficient, density and point mass are respectively denoted by c_D, ρ, and M_L. The damping spring has stiffness k_L and damping coefficient c_L. The strains are given in terms of the longitudinal rod displacement w by $e = \dfrac{\partial w}{\partial x}$.

The direct use of the constitutive relation (3.3) will yield an undamped model for the Terfenol-D rod. We assume that stress is proportional to strain and strain rate to incorporate Kelvin-Voigt damping . Thus, the stress at any point x, $0 \leq x \leq L$, is given by

$$\sigma(t, x) = Y\frac{\partial w}{\partial x}(t, x) + c_D\frac{\partial^2 w}{\partial x \partial t}(t, x) - Y\gamma M^2(t, x). \tag{3.4}$$

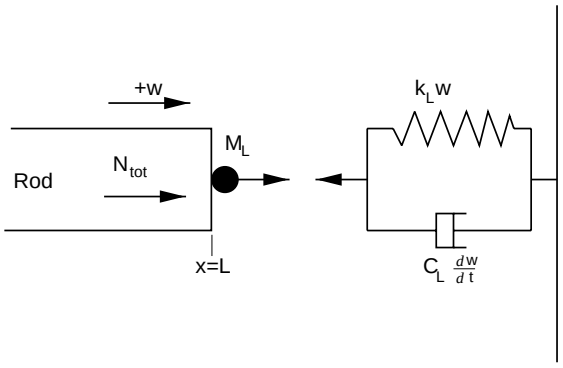

Figure 3.1: Rod model for Terfenol-D transducer.

The relation (3.4) is identical to the relation obtained in [7] if the coupling coefficient is defined as $\gamma = \lambda_s/M_s$ with λ_s and M_s denoting the saturation magnetostriction and saturation magnetization, respectively.

Balancing forces yields

$$\rho A \frac{\partial^2 w}{\partial t^2} = \frac{\partial N_{tot}}{\partial x} \tag{3.5}$$

where A is the cross sectional area of the Terfenol-D rod and the resultant is specified by

$$N_{tot}(t,x) = YA\frac{\partial w}{\partial w}(t,x) + c_D A \frac{\partial^2 w}{\partial x \partial t}(t,x) - YA\gamma M(t,x)^2. \tag{3.6}$$

To obtain appropriate boundary conditions, we first note that $w(t,0) = 0$. Balancing forces at $x = L$ gives

$$N_{tot}(t,L) = -k_L w(t,L) - c_L \frac{\partial w}{\partial t}(t,L) - M_L \frac{\partial^2 w}{\partial x \partial t}(t,L).$$

Initial conditions are taken to be $w(0,x) = 0$ and $\dfrac{\partial w}{\partial x}(0,x) = 0$.

To pose the PDE (3.5) in a form which facilitates approximation, we consider a weak form of the model with a state space of $X = L^2(0,L)$ and the space of test

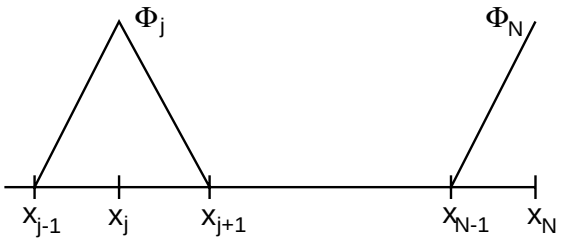

Figure 3.2: Basis elements.

functions is taken to be $V = H_L^1(0, L) \equiv \{\phi \in H^1(0, L) \mid \phi(0) = 0\}$. Multiplication of (3.5) by a test function followed by an integration by parts yields the weak form

$$\begin{aligned} \int_0^L \rho A \frac{\partial^2 w}{\partial t^2} \phi dx &= -\int_0^L \left[YA\frac{\partial u}{\partial x} + c_D A \frac{\partial^2 u}{\partial x} \partial t - YA\gamma M^2 \right] \frac{\partial \phi}{\partial x} dx \\ &\quad - \left[k_L w(t, L) + c_L \frac{\partial w}{\partial t}(t, L) + M_L \frac{\partial^2 w}{\partial t^2}(t, L) \right] \phi(L) \end{aligned} \tag{3.7}$$

which must be satisfied for all $\phi \in H_L^1(0, L)$.

3.1.1 Finite Element Method

For simulation and control implementation, it is necessary to discretize the infinite dimensional model (3.7) in the manner described in [7]. A Galerkin discretization in space is used to reduce equation (3.7) to a temporal system as detailed in [17]. Consider a uniform partition of $[0, L]$ with interval length $h = L/N$. The spatial basis $\{\phi_i\}_{i=1}^N$ is comprised of linear splines of the form

$$\phi_i(x) = \frac{1}{h} \begin{cases} (x - x_{i-1}), & x_{i-1} \le x \le x_i \\ (x_{i+1} - x), & x_i \le x \le x_{i+1} \\ 0, & \text{otherwise} \end{cases} \quad \text{for } i = 1, \cdots, N-1 \tag{3.8}$$

and

$$\phi_N(x) = \frac{1}{h} \begin{cases} (x - x_{N-1}), & x_{N-1} \leq x \leq x_N \\ 0, & \text{otherwise.} \end{cases}$$

Figure 3.2 depicts the basis elements (see [7] for details). The solution, $w(t,x)$, of the weak form (3.7) is approximated by

$$w^N(t,x) = \sum_{j=1}^{N} w_j(t)\phi_j(x). \tag{3.9}$$

Note that (3.9) satisfies $w^N(t,0) = 0$ and, since $H^N = \text{span}\{\phi_i\}_{i=1}^N \subset H_L^1(0,L)$, can attain arbitrary displacements at $x = L$.

The projection of problem (3.7) onto the finite dimensional subspace H^N yields the second-order semidiscrete system

$$Q\ddot{\vec{w}}(t) + C\dot{\vec{w}}(t) + K\vec{w}(t) = \vec{f}(t) \tag{3.10}$$

where $\vec{w}(t) = [w_1(t), \cdots, w_N(t)]$ and Q, C, and K, denoting the mass, stiffness, and damping matrices, respectively, are defined as

$$[Q]_{ij} = \begin{cases} \displaystyle\int_0^L \rho A \phi_i \phi_j dx & i \neq N \text{ or } j \neq N \\ \displaystyle\int_0^L \rho A \phi_i \phi_j dx + M_L & i = N \text{ and } j = N \end{cases}$$

$$[K]_{ij} = \begin{cases} \displaystyle\int_0^L Y A \phi_i' \phi_j' dx & i \neq N \text{ or } j \neq N \\ \displaystyle\int_0^L Y A \phi_i' \phi_j' dx + k_L & i = N \text{ and } j = N \end{cases}$$

$$[C]_{ij} = \begin{cases} \displaystyle\int_0^L c_D A \phi_i' \phi_j' dx & i \neq N \text{ or } j \neq N \\ \displaystyle\int_0^L d_D A \phi_i' \phi_j' dx + c_L & i = N \text{ and } j = N. \end{cases}$$

The forcing vector $\vec{f}$ is defined as

$$\left[\vec{f}(t)\right]_i = \int_0^L Y A \gamma M^2(t,x) \phi_i' dx.$$

Letting $\vec{y}(t) = \left[\vec{w}(t), \dot{\vec{w}}(t)\right]^T$ and

$$A = \begin{bmatrix} 0 & I \\ -Q^{-1}K & -Q^{-1}C \end{bmatrix}, \qquad \vec{F}(t) = \begin{bmatrix} 0 \\ Q^{-1}\vec{f}(t) \end{bmatrix} \tag{3.11}$$

the system in (3.10) can be written as

$$\begin{aligned} \dot{\vec{y}}(t) &= A\vec{y}(t) + \vec{F}(t) \\ \vec{y}(0) &= \vec{y}_0 \end{aligned} \tag{3.12}$$

where the $2N \times 1$ vector $\vec{y}_0$ denotes the projection of the initial conditions into the approximation space. The response of the system (3.12) for several numbers of basis elements is shown in Figure 3.3.

3.1.2 Linearized Model

A linear ordinary differential equation with a nonlinear hysteretic input has been described in (3.12). To further simplify our system, we assert that the magnetization of the Terfenol-D rod can be taken as uniform over the length of the rod. Hence, $H(t,x) = H(t)$ and subsequently $M(t,x) = M(t)$. This is reasonable since in many present actuator design, flux shaping via the surrounding magnet (see Figure 1.3) can

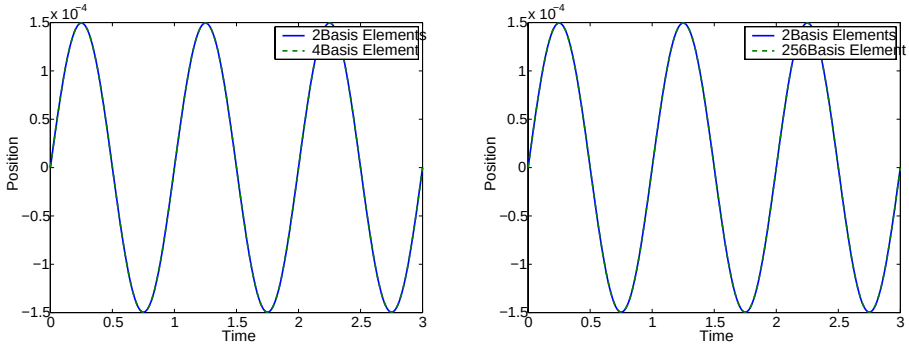

Figure 3.3: Response of finite element method for (a) 4 basis elements, and (b) 256 basis elements plotted against the response for 2 basis elements.

be used to minimize end effects in the rod. This assumption allows us to formulate the model for the dynamics of the rod as

$$\dot{\vec{y}}(t) = A\vec{y}(t) + BM^2(t)$$

$$\vec{y}(0) = y_0 \tag{3.13}$$

where A is given by (3.11) and B is given by

$$B = \begin{bmatrix} 0 \\ Q^{-1}\vec{v} \end{bmatrix} \qquad \vec{v} = \begin{bmatrix} 0 \\ YA\gamma \end{bmatrix}. \tag{3.14}$$

To further simplify the dynamics of the Terfenol-D transducer we shall linearize the magnetostrictive relationship about a biasing magnetization level M_0. This is motivated by the physical observation that transducers operating about a biased field produced by the permanent magnet exhibit a nearly linear relation between magnetization and strains for moderate drive level regimes. We can now approximate

the forcing term $\vec{f}$ as $\vec{\beta}M(t)$ where

$$\vec{\beta}_i = \begin{cases} 0, & i \neq N \\ 2YA\gamma M_0, & i = N. \end{cases} \tag{3.15}$$

Therefore, we can represent the dynamics of the Terfenol-D transducer by

$$\begin{aligned} \dot{\vec{x}}(t) &= A\vec{x}(t) + \widehat{B}M(t) \\ \vec{x}(0) &= x_0 \end{aligned} \tag{3.16}$$

where $A = \begin{bmatrix} 0 & I \\ -Q^{-1}K & -Q^{-1}C \end{bmatrix}$, as previously defined, and $\widehat{B} = \begin{bmatrix} 0 \\ Q^{-1}\vec{\beta} \end{bmatrix}$. Since only the displacement at the tip of the rod is observed, the observation vector is taken to be $C = [0, 0, \ldots, 1, 0, \ldots, 0] \in \mathbb{R}^{2N}$. Note that the hysteretic behavior of the transducer is still present in (3.16) by means of the hysteretic relationship between the applied field H and the magnetization M.

3.2 ODE Model for Transducer Dynamics

Since a Galerkin approximation method was utilized, the matrix A and vector $\widehat{B}$ in the linearized model (3.16) are dependent on the number of basis elements required to achieve convergence. For transducer construction in which flux shaping via the permanent magnet can be employed to reduce spatial variability in the rod, the PDE rod model can be adequately approximated by an ODE elastic model. In this case, the model for the Terfenol-D transducer is given by

$$\begin{aligned} \ddot{x} + k\dot{x} + cx &= bM(t) \\ x(0) = 0 \quad \dot{x}(0) &= 0 \end{aligned} \tag{3.17}$$

where the scalars k, c and b need to be determined by a fit to the Galerkin approximation (3.16) or experimental data. For the purposes of this dissertation, the ODE model (3.17) is fit to the Galerkin approximation model (3.16).

The parameters in (3.17) are determined by means of the transfer function representation. The transfer function for (3.17) is given as

$$\widehat{G}(s) = \frac{b}{s^2 + ks + c}. \tag{3.18}$$

Examination of the zeros and poles of the transfer function representation of the finite element formulation (3.16) with various numbers of basis elements illustrated that every pole is approximately a zero of the transfer function, with the exception of two (see Table 3.1 and Table 3.2). Therefore, for any number of basis elements the transfer function representation of (3.16) approximately represents a second order ODE. Therefore, we need (3.18) to be equivalent to

$$\tilde{G}(s) = \frac{q}{(s - p_1)(s - p_2)} \tag{3.19}$$

where p_1 and p_2 are the poles of the transfer function resulting from the finite element formulation which are not effectively cancelled by a zero and q is the gain. In order

2 Basis Functions

Zeros	Poles
-2.8392×10^5	-2.9864×10^5
-1.0365×10^4	-1.0343×10^4
	$-3.9450 \times 10^3 - 6.9777 \times 10^3 i$
	$-3.9450 \times 10^3 + 6.9777 \times 10^3 i$

Table 3.1: Zeros and poles of (3.16) utilizing 2 basis functions.

Zeros	Poles
-1.6826×10^7	-1.6830×10^7
-1.2424×10^7	-1.2434×10^7
-8.0409×10^6	-8.0549×10^6
-4.6985×10^6	-4.7134×10^6
-2.4298×10^6	-2.4442×10^6
-1.0088×10^6	-1.0226×10^6
-2.3472×10^5	-2.4803×10^5
-1.0445×10^4	-1.0416×10^4
-1.0100×10^4	-1.0099×10^4
-1.0041×10^4	-1.0041×10^4
-1.0021×10^4	-1.0021×10^4
-1.0012×10^4	-1.0012×10^4
-1.0006×10^4	-1.0006×10^4
-1.0008×10^4	-1.0008×10^4
	$-3.9430 \times 10^3 - 6.9770 \times 10^3 i$
	$-3.9430 \times 10^3 + 6.9770 \times 10^3 i$

Table 3.2: Zeros and poles of (3.16) utilizing 8 basis functions.

to achieve an accurate transfer function, the poles are obtained from the finite element system with a sufficient number of basis elements to ensure convergence, namely $N = 32$. The parameters k and c can be determined from p_1 and p_2. Determining the gain b in (3.18) is not as simple as determining k and c due to the fact that the similar poles and zeros do not exactly cancel. The gain b can be found utilizing an optimization technique with the cost function being the maximum difference between the response of (3.17) and (3.16) with the appropriate number of basis elements. A Nelder-Mead simplex method was employed for this optimization and the parameters employed in the ODE model of the transducer (3.17) are given in Table 3.3.

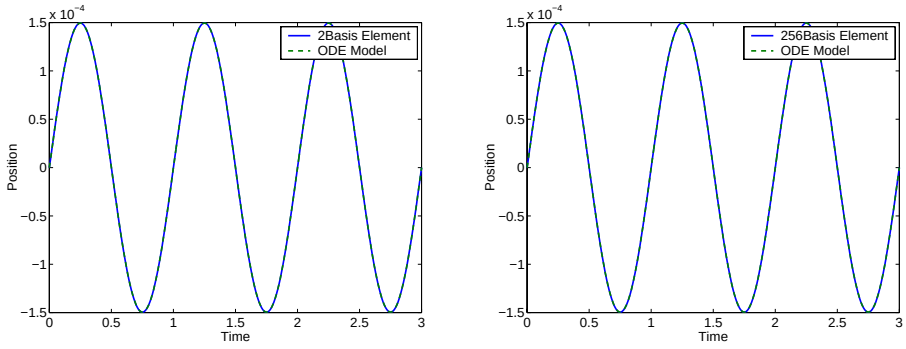

Figure 3.4: Finite element verses spring model response.

Figure 3.4 illustrates the response of the damped spring mass model as compared the finite element formulation for various basis sizes. The infimum of the absolute value of the differences between the responses of (3.17) and (3.16) driven by a sinusoidal force are given in Table 3.4. The small errors validate the use of the ODE model (3.17) to represent the dynamics of the Terfenol-D transducer if we can assume the magnetostriction is uniform along the rod. This places the emphasis on the design of the transducer to minimize end effects in the magnetic fields.

If the permanent magnet in the Terfenol-D transducer were not designed to minimize the end effects of the magnetic field, the finite element model could be employed in the subsequent control designs. The main difference being the number of states in the transducer model would be greater which may increase the number of states in a model-based controller.

b	k	c
1.3724×10^{-2}	7.8899×10^{3}	6.4251×10^{7}

Table 3.3: ODE model parameters for Terfenol-D transducer.

N	2	4	8	16	32
Error	6.29×10^{-8}	1.62×10^{-8}	3.95×10^{-9}	8.48×10^{-10}	7.08×10^{-11}

N	64	128	256
Error	2.48×10^{-10}	2.96×10^{-10}	3.08×10^{-10}

Table 3.4: Maximum error between finite element model and ODE model.

3.3 Concluding Remarks

This chapter summarized techniques for modeling the forces, strains and displacements in a prototypical magnetostrictive transducer. Under certain conditions on the design of the transducer, the transducer can be accurately modeled as a second order ODE. While the transducer model in this chapter is developed in the context of a magnetostrictive material, namely Terfenol-D, the techniques can be applied to model transducers incorporating many smart material including piezoceramics.

Chapter 4

Nonlinear Parameter Estimation

In Chapters 2 and 3, models describing a prototypical Terfenol-D transducer were summarized. Both the domain wall and free energy models of the hysteretic behavior inherent in the magnetostrictive material have nonlinearly occurring material dependent parameters. In this chapter, we develop an adaptive parameter estimation method to determine these nonlinearly occurring parameters in an efficient manner. The method proposed here requires only the measurement of the tip of the Terfenol-D rod and can be employed in a control setting. This chapter utilizes the domain wall model (2.8) but it is noted that this can also be employed to estimate parameters in the free energy model (2.37).

Data fitting techniques to determine material parameters require a significant amount of data and time and must be done prior to the activation of the transducer. However, the parameter estimation techniques summarized here may be employed while the transducer is operating and can provide either continuous or periodical tuning of parameters which may vary during the operation. In particular, Ohmic heating in the wire solenoid may affect the behavior of the inherent hysteresis in the material and the parameter a in the domain wall model may need to be adjusted to reflect this change. Figure 4.1 illustrates the affect of variations in the value of a.

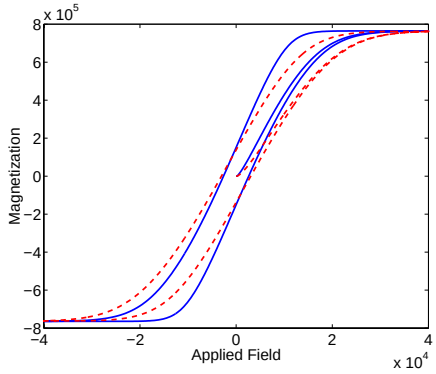

Figure 4.1: Domain wall hysteresis models for two values of a.

A significant difficulty in the development of nonlinear parameter adaptation techniques is the fact that a gradient method is not always sufficient for a nonlinearly occurring parameter. To illustrate, consider an error model of the form

$$\dot{e} = -ke + f(\phi, \theta) - f(\phi, \widehat{\theta}) \tag{4.1}$$

where e is the tracking error, $k > 0$, ϕ is a measurable state, $\theta \in \mathbb{R}^m$ is a vector of nonlinearly occurring parameters , $\widehat{\theta} \in \mathbb{R}^m$ is the parameter estimates and f is a nonlinear, scalar valued function. Consider the gradient update law

$$\dot{\widehat{\theta}} = e \nabla f_{\hat{\theta}} \tag{4.2}$$

where $\nabla f_{\hat{\theta}}$ denotes the gradient of f with respect to $\widehat{\theta}$. Choosing a standard Lyapunov candidate

$$V = \frac{1}{2}(e^2 + \tilde{\theta}^2) \tag{4.3}$$

where $\tilde{\theta} = \widehat{\theta} - \theta$ and substituting (4.2) into the derivative of (4.3) we obtain

$$\dot{V} = -ke^2 + e\left[f(\phi,\theta) - f(\phi,\widehat{\theta}) + \widehat{\theta}\nabla f_{\hat{\theta}}\right] \ . \tag{4.4}$$

Equation (4.4) indicates that if $e < 0$, we need $\nabla f_{\hat{\theta}}(\theta - \widehat{\theta}) \leq f(\phi,\theta) - f(\phi,\widehat{\theta})$ to ensure $\dot{V} \leq 0$. This is true if f is convex with respect to θ. Likewise if $e > 0$, then $\dot{V} \leq 0$ if f is concave. As the nonlinear function f is possibly convex in some regions and concave in others, the gradient method (4.2) does not ensure stability for all $\widehat{\theta}$.

A gradient method applied to a nonlinear parameterized system may not only be insufficient but may lead to instability. The method summarized in this chapter does not strictly rely on a gradient rule but differs depending on the sign of the error. The parameter update relies on the convexity or concavity of the nonlinear function as is indicated by the Lyapunov candidate (4.3).

4.1 Scalar Equation Case

We summarize first the nonlinear parameterization techniques developed in [9, 14] which are based on the assumption that all of the states are available. It will be shown that this method provides a stable adaptive parameter estimation algorithm and the convergence of the parameters is ensured given certain persistent excitation conditions are satisfied. The proposed method can track a reference signal to a desired accuracy, $\epsilon > 0$, and identifies parameters for general systems of the form

$$\dot{y} = -ky + f(u(t),\theta) \tag{4.5}$$

where $\theta \in \Theta$ is an unknown vector of nonlinearly occurring parameters, Θ is a bounded subset of $\mathbb{R}^m$, and $k > 0$ is a scalar. The function f is a scalar valued nonlinear

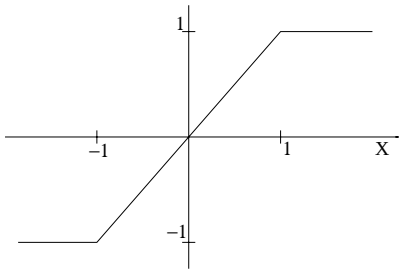

Figure 4.2: Saturation function $\mathrm{sat}(x)$.

function of the input $u(t)$. The nonlinear parameter estimation algorithm developed in [9, 14] can be formulated as

$$\begin{aligned}
\dot{\widehat{y}} &= -k\left[\widehat{y} - \epsilon\ sat(\tfrac{\tilde{y}}{\epsilon})\right] + f(u,\widehat{\theta}) - a^{*}\mathrm{sat}\left(\tfrac{\tilde{y}}{\epsilon}\right) \\
\dot{\widehat{\theta}} &= -\tilde{y}_{\epsilon}\phi^{*} \\
\tilde{y}_{\epsilon} &= \tilde{y} - \epsilon\ \mathrm{sat}\left(\tfrac{\tilde{y}}{\epsilon}\right) \\
\tilde{y} &= \widehat{y} - y
\end{aligned} \tag{4.6}$$

where $\epsilon > 0$, $\mathrm{sat}(\cdot)$ is the saturation function which is illustrated in Figure 4.2 and defined as

$$\mathrm{sat}(x) = \begin{cases} 1, & x \geq 1 \\ x, & |x| < 1 \\ -1, & x \leq -1 \end{cases} \tag{4.7}$$

and a^{*} and ϕ^{*} are the solution of

$$\begin{aligned}
a^{*} &= \min_{\phi\in\mathbb{R}^{m}} \max_{\theta\in\Theta}\ J(\theta,\phi) \\
\phi^{*} &= arg \min_{\phi\in\mathbb{R}^{m}} \max_{\theta\in\Theta}\ J(\theta,\phi) \\
J(\theta,\phi) &= \mathrm{sat}(\tfrac{\tilde{y}}{\epsilon})(f(u,\widehat{\theta}) - f(u,\theta) - \phi^{T}(\widehat{\theta}-\theta))\ .
\end{aligned} \tag{4.8}$$

It is noted that when $|\tilde{y}| < \epsilon$, the adaptation of the parameters stops. This imposes what is termed a dead-zone. The importance of this dead-zone will be investigated when the persistent excitation conditions are discussed. The purpose of the min/max algorithm is to handle the regions of nonconvexity of f where the gradient method is insufficient. The use of a tuning error $\tilde{y}_\epsilon$ rather than a tracking error $\tilde{y}$ is to ensure continuity of the adaptation. This is also the motivation for employing a saturation function rather than a signum function [14]. The assumption that the parameters and the parameter estimates are bounded is not needed for stability but is needed to compute the closed form solution of (4.8) [14].

Defining $\tilde{\theta} = \widehat{\theta} - \theta$ and $x = [\tilde{y}, \tilde{\theta}^T]^T$, it can be shown that the system (4.6) is stable about $x = 0$ by proving that $V = \tilde{y}_\epsilon^2 + \tilde{\theta}^2$ is a Lyapunov function. We provide below details illustrating the original proof from [14]. We first note that

$$\dot{V} = 2\tilde{y}_\epsilon \dot{\tilde{y}}_\epsilon + 2\tilde{\theta}\dot{\tilde{\theta}}. \tag{4.9}$$

If $|\tilde{y}| \leq \epsilon$ then $\tilde{y}_\epsilon = 0$ so $\dot{V} = 0$. We need to show that $\dot{V} \leq 0$ if $|\tilde{y}| > \epsilon$. We first represent $\dot{V}$ as

$$\begin{aligned}
\dot{V} &= 2\tilde{y}_\epsilon(-k\left(\widehat{y} - \epsilon \text{ sat}\left(\tfrac{\tilde{y}}{\epsilon}\right)\right) + f(u,\widehat{\theta}) - a^* \text{sat}\left(\tfrac{\tilde{y}}{\epsilon}\right) + \alpha y - f(u,\theta)) - 2\tilde{\theta}\tilde{y}_\epsilon\phi^* \\
&= -2k\tilde{y}_\epsilon\ \tilde{y}_\epsilon + 2\tilde{y}_\epsilon(f(u,\widehat{\theta}) - f(u,\theta) - \tilde{\theta}\phi^* - a^* \text{sat}\left(\tfrac{\tilde{y}}{\epsilon}\right)) \\
&= -2k\tilde{y}_\epsilon^2 + 2\tilde{y}_\epsilon((f(u,\widehat{\theta}) - f(u,w) - \tilde{\theta}\phi^*) - a^* \text{sat}\left(\tfrac{\tilde{y}}{\epsilon}\right)).
\end{aligned} \tag{4.10}$$

If $\tilde{y} > 0$ then $\text{sat}\left(\frac{\tilde{y}}{\epsilon}\right) = 1$ so we must have

$$a^* \geq \text{sat}\left(\frac{\tilde{y}}{\epsilon}\right)(f(u,\widehat{\theta}) - f(u,\theta) - \tilde{w}\phi^*)\ \forall\theta \in \Theta. \tag{4.11}$$

This implies that we can let

$$a^* = \max_{\theta \in \Theta} \text{sat}\left(\frac{\tilde{y}}{\epsilon}\right)(f(u,\widehat{\theta}) - f(u,\theta) - \tilde{w}\phi^*) \text{ for any } \phi^*. \tag{4.12}$$

The inequality (4.11) is satisfied by the definition of ϕ^* and a^*, hence $\dot{V} \leq 0$.
If $\tilde{y} < 0$ then $\text{sat}\left(\frac{\tilde{y}}{\epsilon}\right) = -1$ so we must have

$$a^* \geq -(f(u,\widehat{\theta}) - f(u,\theta) - \tilde{\theta}\phi^*) \; \forall \theta \in \Theta. \tag{4.13}$$

or

$$a^* \geq \text{sat}\left(\frac{\tilde{y}}{\epsilon}\right)(f(u,\widehat{\theta}) - f(u,\theta) - \tilde{w}\phi^*) \quad \forall \theta \in \Theta. \tag{4.14}$$

Again we can let

$$a^* = \max_{\theta \in \Theta} \text{sat}\left(\frac{\tilde{y}}{\epsilon}\right)(f(u,\widehat{\theta}) - f(u,\theta) - \tilde{w}\phi^*) \text{ for any } \phi^*. \tag{4.15}$$

By the definition of ϕ^* and a^* the inequality (4.14) is satisfied, hence $\dot{V} \leq 0$.

To implement the system (4.6) we must solve the min/max problem (4.8). To do this, a concave cover $\underline{F}(\theta)$ and a convex cover $\overline{F}(\theta)$ are constructed such that $\underline{F}(\theta) \geq f - \widehat{f}$ and $\overline{F}(\theta) \leq f - \widehat{f}$ where $\widehat{f} = f(u,\widehat{\theta})$. To determine these covers, we employ the following definitions.

Definition 1: A point $\theta^0 \in \theta_c$ if $\theta^0 \in \Theta$ and

$$\nabla f_{\theta^0}(\theta - \theta^0) \geq f - f^0$$

where $\nabla f_{\theta^0} \equiv \left.\dfrac{\partial f}{\partial \theta}\right|_{\theta^0}$ and $f^0 = f(\phi, \theta^0)$.

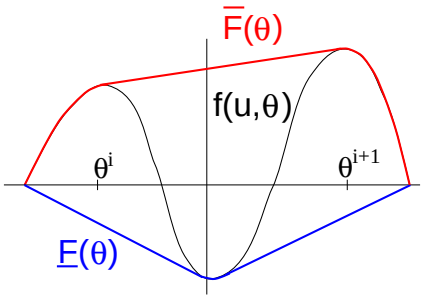

Figure 4.3: Concave and convex covers.

Definition 2: $\tilde{\theta}_c \equiv \overline{\theta}_c \cap \Theta$ where $\overline{\theta}_c$ is the complement of θ_c.

If f is not concave over Θ then $\tilde{\theta}_c = \{\theta^{12}, \theta^{34}, \ldots, \theta^{mn}\}$ where $\theta^{ij} = [\theta^i \ \theta^j]$ are the regions where f is not concave, $\theta^j \geq \theta^j$. Using Definitions 1 and 2 we can construct the concave cover of f on Θ as

$$\underline{F}(\theta) = \begin{cases} f - \widehat{f}, & \forall \theta \in \theta_c \\ \phi^{ij}\theta + c^{ij}, & \forall \theta \in \theta^{ij} \in \tilde{\theta}_c \end{cases} \tag{4.16}$$

where

$$\phi^{ij} = \frac{f^j - f^i}{\theta^j - \theta^i}, \qquad c^{ij} = f^i - \hat{f} - \phi^{ij}\theta^i, \quad \text{and} \quad f^i = f(\phi, \theta^i).$$

Similarly a convex cover of f is constructed by defining

$$\begin{aligned} \theta_v &\equiv \{\theta^0 \mid \nabla f_{\theta^0}(\theta - \theta^0) \leq f - f^0\} \\ \tilde{\theta}_v &\equiv \overline{\theta}_v \cap \Theta \end{aligned}$$

and

$$\overline{F}(\theta) = \begin{cases} f - \widehat{f}, & \forall \theta \in \theta_v \\ \phi^{ij}\theta + c^{ij}, & \forall \theta \in \theta^{ij} \in \tilde{\theta}_v \ . \end{cases} \tag{4.17}$$

Examples of a convex and a concave cover of a function are illustrated in Figure 4.3.

Once we have constructed $\underline{F}(\theta)$ and $\overline{F}(\theta)$, a close form solution to the min/max problem (4.8) can be determined as illustrated in the following theorem.

Theorem 4.1: The solution of the min/max problem (4.8) is given by

$$\begin{aligned} a^* &= \underline{F}(\widehat{\theta}) \\ \phi^* &= \begin{cases} \nabla f_{\hat{\theta}}, \text{ if } \widehat{\theta} \in \theta_c & \text{if } \tilde{y}_\epsilon > 0 \\ \phi^{ij}, \text{ if } \widehat{\theta} \in \theta^{ij} \in \tilde{\theta}_c \end{cases} \\ a^* &= -\overline{F}(\widehat{\theta}) \\ \phi^* &= \begin{cases} \nabla f_{\hat{\theta}}, \text{ if } \widehat{\theta} \in \theta_v & \text{if } \tilde{y}_\epsilon < 0 \\ \phi^{ij}, \text{ if } \widehat{\theta} \in \theta^{ij} \in \tilde{\theta}_v \end{cases} \end{aligned} \quad . \tag{4.18}$$

The proof of Theorem 4.1 can be found in Appendix 1.

These results establish the stability of the method via the solution of the min/max problem. We seek to determine sufficient conditions for uniform asymptotic stability of the system (4.6). The following theorem from [9] states a condition guaranteeing convergence of the parameters and tracking error.

Theorem 4.2: If for every $t_1 > t_0$, there exists $T_0,\ \epsilon_0,\ \delta_0$, and a subinterval $[t_2,\ t_2 + \delta_0] \in\ [t_1,\ t_1 + T_0]$ such that

$$\beta \int_{t_2}^{t_2+\delta_0} \left((t_2) f\left(u, \widehat{\theta}(t_2)\right) - f(u, \theta) \right)\ d\tau \geq 2\epsilon + \epsilon_0 ||\tilde{\theta}(t_2)||, \tag{4.19}$$

then the origin $x = 0$ is uniform asymptotically stable.

A proof of Theorem 4.2 can be found in [9].

In Theorem 4.2, $\beta = 1$ if $f\left(u, \widehat{\theta}\right)$ is convex and $\beta = -1$ if $f\left(u, \widehat{\theta}\right)$ is concave. There are several differences to notice between this condition and the condition for a linear parameterization. First, the sign of the integral is important. The sign is not strictly determined by $f\left(u, \widehat{\theta}\right) - f(u, \theta)$ but rather by the convexity or concavity of f as displayed by β. This coupling arises from the min/max algorithm and is necessary but not sufficient to ensure that the method will leave the dead-zone $|\tilde{y}| \leq \epsilon$. The integral must be large enough to leave the dead-zone thus necessitating the term incorporating ϵ on the right of (4.19).

The excitation conditions have been placed on f in the Theorem 4.2. Theorem 4.2 does not explicitly give conditions on the input u to satisfy the inequality (4.19) nor does it guarantee that such an input exists. By examining the inequality (4.19), conditions on u can be derived to ensure uniform asymptotic stability. The inequality (4.19) includes two components, the first being that the magnitude of the integrand must be sufficiently large. This states that for a large parameter error, the input must be such that the difference between the function evaluated at the actual parameter and the parameter estimate must be adequately large. Secondly, the integral must be the same sign as β. This states that if f is convex, the integrand should be positive and likewise if f is concave the integrand should be negative. Since parameter convergence is ensured by updating based on gradient information, the min/max feature of the algorithm will give stability but an acceptable input must be used to guarantee parameter convergence. To ensure parameter convergence, one of the following conditions must hold.

1) For the given $\tilde{\theta}$, u must reverse the sign of the integrand of (4.19) while keeping the convexity/concavity of f fixed.

2) For the given $\tilde{\theta}$, u must reverse the convexity/concavity of f, while preserving the sign of the integrand of (4.19).

4.2 Vector System

The nonlinear parameter identification algorithm (4.6) is formulated for scalar differential equations. It is necessary to extend the method proposed in [9, 14] to a system of equations since many physical systems with inherent hysteresis, including the Terfenol-D transducer, are modeled by higher order equations. Recall that the transducer has been represented by a second order ODE (3.17) with

$$A = \begin{bmatrix} 0 & 1 \\ -c & -k \end{bmatrix} \qquad\qquad B = \begin{bmatrix} 0 \\ \omega \end{bmatrix} \tag{4.20}$$

where $c,\ k$ and ω are given in Table 3.3. In this section we will extend the nonlinear parameter identification algorithm to asymptotically stable second-order systems to address such applications.

To adapt the method for vector systems, we must redefine several of the variables from the scalar case. Since we want to use the solution to the min/max problem (4.8), we must ensure that we do not affect that aspect of the formulation. Consider the identification of the parameter θ for the matrix system

$$\dot{y} = Ay + Bf(u, \theta) \tag{4.21}$$

where $A \in \mathbb{R}^{2\times 2}$ and $B \in \mathbb{R}^{2\times 1}$. We then consider the adaptation algorithm

$$\begin{aligned} \dot{\widehat{y}} &= A\widehat{y} + B\left(f(u,\widehat{\theta}) - a^*\text{sat}\left(\tfrac{\tilde{y}_\epsilon}{\epsilon}\right)\right) \\ \dot{\widehat{\theta}} &= -\gamma\tilde{y}_\epsilon\phi^* \\ \tilde{y} &= \widehat{y} - y \\ \tilde{y}_\epsilon &= B_2p_2\tilde{y}_1 + B_2p_3\tilde{y}_2 \end{aligned} \tag{4.22}$$

where p_2 and p_3 are scalars to be determined, $\gamma > 0$ is a scalar gain, B_2 is the (2,1) component of vector B, and a^* and ϕ^* are solutions of the min/max problem

$$\begin{aligned} a^* &= \min_{\phi\in\mathbb{R}^m} \max_{\theta\in\Theta} g(\theta,\phi) \\ \phi^* &= arg \min_{\phi\in\mathbb{R}^m} \max_{\theta\in\Theta} g(\theta,\phi) \\ g(\theta,\phi) &= \text{sat}\left(\tfrac{\tilde{y}_\epsilon}{\epsilon}\right)\left(f(u,\widehat{\theta}) - f(u,\theta) - \phi^T(\widehat{\theta}-\theta)\right). \end{aligned} \tag{4.23}$$

It is important to note that the solution to the min/max problem (4.23) is the solution to (4.8) so this aspect of the adaptive estimation is the same as the scalar case. A notable differences between the matrix system method (4.23) and the scalar method (4.8) is the definition of $\tilde{y}_\epsilon$. The alteration of $\tilde{y}_\epsilon$ is necessary for the Lyapunov candidate utilized for the vector system. Note that the adaptation algorithm does not have the dead-zone observed in the scalar method.

The following theorem ensures the globally asymptotic stability of the adaptive parameters estimation method (4.22).

Theorem 4.3: If the vector system (4.21) is globally asymptotically stable, the adaptive parameter estimation algorithm (4.22) is globally asymptotically stable.

Proof: To prove Theorem 4.3, we consider the Lyapunov function

$$V = \gamma\tilde{y}^T P\tilde{y} + \tilde{\theta}^2 \tag{4.24}$$

where P is a symmetric positive definite matrix. Taking the derivative of (4.24) yields

$$\dot{V} = \gamma\dot{\tilde{y}}^T P\tilde{y} + \gamma\tilde{y}^T P\dot{\tilde{y}} + 2\tilde{\theta}\dot{\widehat{\theta}} \tag{4.25}$$

with

$$\dot{\tilde{y}} = A\tilde{y} + B\left(\hat{f} - f - a^* \text{sat}\left(\frac{y_\epsilon}{\epsilon}\right)\right) . \tag{4.26}$$

Employing the definitions of $\dot{\tilde{y}}$ and $\dot{\widehat{\theta}}$, we can now write

$$\begin{aligned} \dot{V} &= \gamma\left(\tilde{y}^T A^T P\tilde{y} + \tilde{y}^T PA\tilde{y}\right) \\ &\quad +2\gamma\left(\left(\hat{f} - f - a^* \text{sat}\left(\tfrac{y_\epsilon}{\epsilon}\right)\right) B^T P\tilde{y} - \tilde{y}_\epsilon \tilde{\theta}\phi^*\right) . \end{aligned} \tag{4.27}$$

Since A is globally asymptotically stable, for any symmetric positive definite matrix Q there exists a symmetric positive definite matrix P such that $A^T P + PA = -Q$ [2]. Denoting

$$P = \begin{bmatrix} p_1 & p_2 \\ p_2 & p_3 \end{bmatrix} , \tag{4.28}$$

we have $B^T P\tilde{y} = \omega p_2 \tilde{y}_1 + \omega p_3 \tilde{y}_2 = \tilde{y}_\epsilon$. Substituting this into (4.27) gives

$$\dot{V} = -\gamma\left(\tilde{y}^T Q\tilde{y}\right) + 2\gamma\tilde{y}_\epsilon\left(\hat{f} - f - \tilde{\theta}\phi^* - a^* \text{sat}\left(\frac{y_\epsilon}{\epsilon}\right)\right) . \tag{4.29}$$

The proof that $\dot{V} < 0$ is completed by utilizing the definitions of a^* and ϕ^* as the solutions of (4.23) in a manner similar to that employed in the proof in the scalar case. Note that the parameters p_2 and p_3 can be determined for any symmetric positive definite choice of Q. Notable alteration of the parameter estimation algorithm from the scalar case includes the lack of a dead-zone as well as the omission of the $\epsilon\ sat(\frac{\tilde{y}}{\epsilon})$ term in the definition of $\dot{\hat{y}}$. These alterations are necessitated by the form of the Lyapunov function.

4.3 Numerical Examples

A scalar and matrix example will be provided to demonstrate the ability of the nonlinear adaptive parameter estimation method.

4.3.1 Scalar Case

First, we shall examine the scalar case. The dynamics of the system specified by the differential equation

$$\dot{y} = -ky + M(H, a) \tag{4.30}$$

where $M(H, a)$ is the solution of the domain wall model for the hysteretic material as given by (2.8) for a given applied field H. The parameter a in the domain wall model was chosen as it may vary with temperature. As the transducer operates, small changes in the temperature will occur due in part to Ohmic heating in the solenoids (see Figure 1.3). As previously stated, it would be beneficial to periodically tune the value of a to reflect the changes in the behavior of the Terfenol-D due to the temperature changes without having to turn off the actuator. This can be accomplished by the proposed adaptive parameter estimation algorithm.

The parameter estimate $\widehat{a}$ was assumed to be bounded with $\widehat{a} \in [6300,\ 7300]$ and $\widehat{a}(0) = 6990$. The actual value of a is taken to be 7012 and the remaining constants in the domain wall model are given in Table 2.1. The scalar k is taken as 100.

One difficulty in the adaptive parameter estimation utilized is constructing an input $H(t)$ which will provide persistent excitation. The conditions imposed for excitation prompt the use of a signal that does not cause the function to change signs. It is observed that a monotonically increasing input provides persistent excitation as well as quick convergence. The input applied field $H(t)$ chosen was a hyperbolic tangent function which would drive the hysteresis to a level near the saturation level.

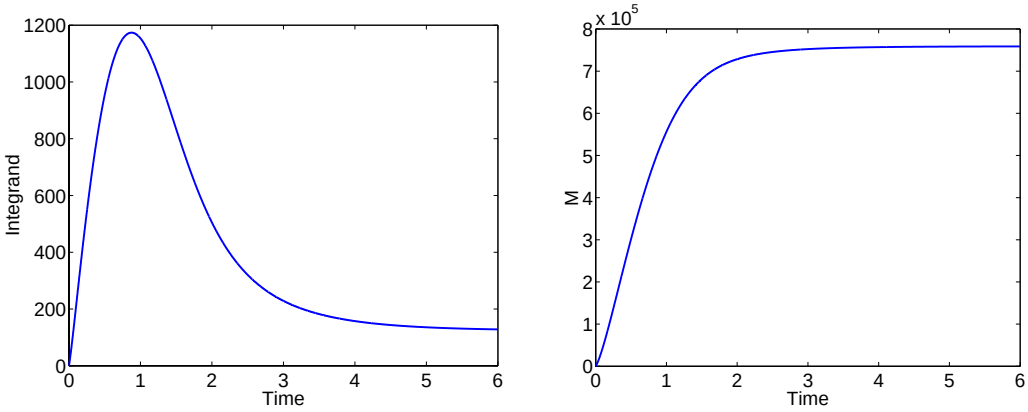

(a) (b)

Figure 4.4: (a) Value of integrand of eq. (4.19), and (b) value of $M(u, \widehat{a})$.

This signal was chosen to provide persistent excitation as well as evaluating the hysteresis model at levels which most noticeably differ with respect to the parameter a. Figure 4.4a depicts the integrand of (4.19) for a given value of $\tilde{\theta}$ to show that persistent excitation condition 2 is met. The integrand remains positive while switching the convexity/concavity of the function M as seen in Figure 4.4b.

Figure 4.5 illustrates the capability of the scalar nonlinear parameter estimation method to accurately estimate the unknown parameter a. Figure 4.5a depicts the evolution of the parameter estimate $\widehat{a}$ which quickly converges to the actual value of a. The tracking error $\tilde{y}$ is illustrated in Figure 4.5b. The speed of convergence of the parameter estimation is notable since this identification method could potentially be combined with a control technique.

4.3.2 Vector System

We now illustrate the nonlinear adaptive parameter estimates for a vector system as developed in Section 4.2. The system we shall consider is a damped spring mass

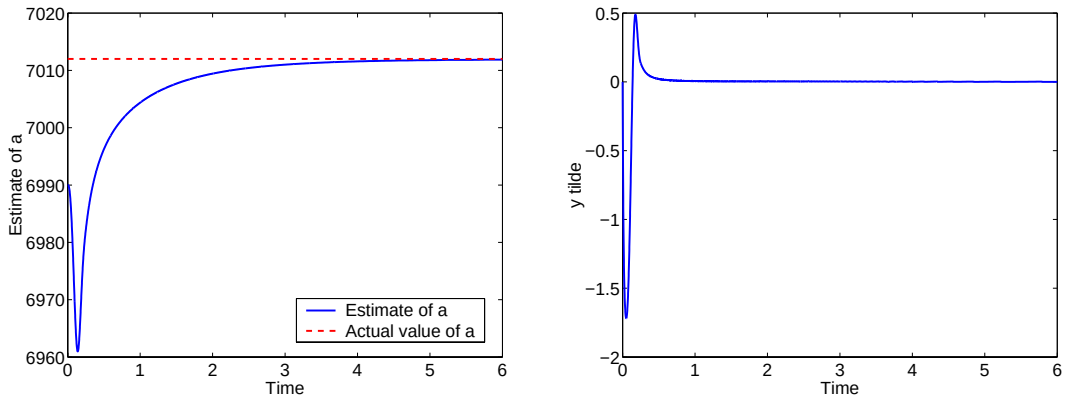

(a) (b)

Figure 4.5: (a) Parameter estimate value, and (b) tracking error for scalar case.

system which can be used to model the transducer dynamics of the smart material transducer given by equation (3.17) with the values of the domain wall model parameters taken from Table 2.1. Again, the parameter a is to be determined because of its temperature dependence. The gain γ is taken to be 5×10^{10} and P is found utilizing a matrix

$$Q = \begin{bmatrix} 1 \times 10^{10} & 0 \\ 0 & 1 \times 10^{-8} \end{bmatrix}. \tag{4.31}$$

We employ the same applied magnetic field as in the scalar example.

The method's ability to estimate the parameter for the matrix example is illustrated in Figure 4.6. Figure 4.6 shows the convergence of the estimate to the actual parameter value $a = 7012$. Figure 4.7 illustrates the tracking error of the adaptive system for the vector system in which $\tilde{y}$ is also a vector. This example illustrates the convergence of the adaptive parameter estimation algorithm for vector systems.

For the implementation of the scalar or matrix system there are a number of numerical issues. The models must be solved numerically and since implicit methods

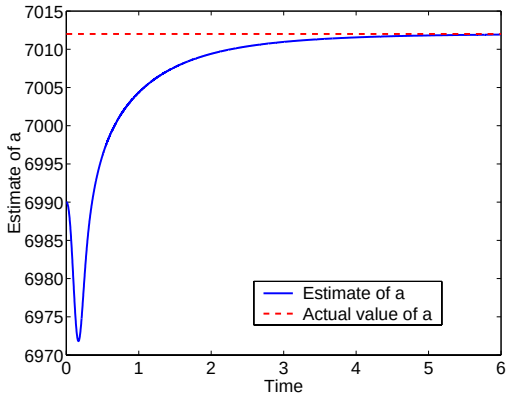

Figure 4.6: Parameter estimate value for matrix case.

are not feasible because of the unknown forcing function at the next time step, the time step must be sufficiently small to ensure accurate solutions of the model. Any inaccuracy of the solution can cause the value of $\tilde{y}$ to have discontinuous jump from positive to negative values. This phenomena causes the min/max solution to jump between utilizing the convex cover and concave cover which, in turn, can cause highly oscillatory behavior in the parameter updates.

4.4 Concluding Remarks

The nonlinear parameter identification technique developed in [9, 14] has shown to be effective for identifying a parameter in the nonlinear domain wall model incorporated as the forcing function in a scalar ODE. We have also extended this parameter identification method to apply to second order systems. In this latter framework, this adaptive parameter estimation algorithm can be used to estimate and update parameters in a wide range of hysteretic systems including SMAs, ferroelectrics and ferromagnetics. Due to the persistent excitation conditions placed on the input to the

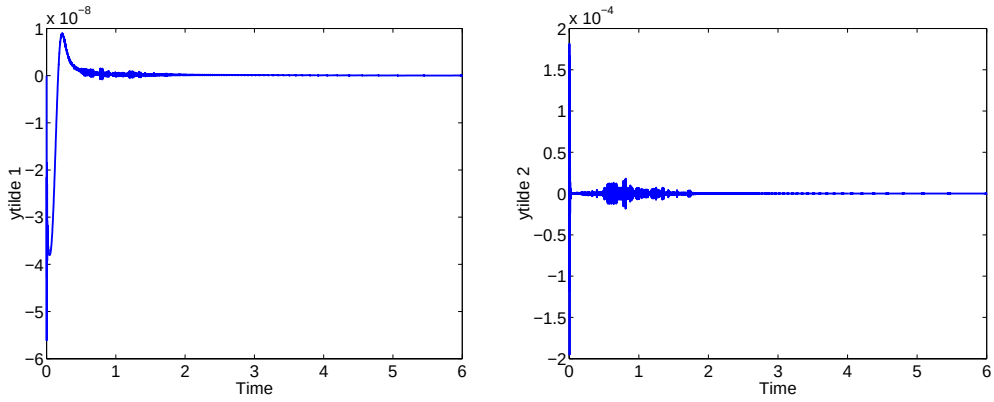

(a) (b)

Figure 4.7: (a) $\tilde{y}_1$, and (b) $\tilde{y}_2$ for matrix case

hysteresis model, there are potential difficulties in employing the scalar method as a closed-loop nonlinear adaptive control method by considering the nonlinear function in the dynamics to be the composition of an approximate inverse and the hysteresis function as was done linearly in [10, 11]. The vector method does not require persistent excitation conditions, therefore, may be amenable to the extension to an adaptive control method.

One possible control method utilizing this parameter identification method could be to identify the temperature dependent parameter a in the domain wall hysteresis model while the transducer is being initialized. Once the hysteresis model is completely determined, a partial inverse compensation method, e.g. [4] or [16], could be applied. The method in this paper could be employed to periodically re-identify the parameters in the hysteresis model to ensure accurate modeling as the parameters slowly vary due to the internal heat generated by many industrial applications. This may be more efficient and accurate than current methods of parameter identification, such as least square fits to data, and can be performed on-line. The next step

would be to apply this method to multiple unknown parameters, i.e., $\theta \in \mathbb{R}^m$. This method potentially could provide a new method to identify the full set of parameters, $\{a,\ k,\ c,\ \alpha,\ P_s\}$, simultaneously. While theoretically the method can provide multiple parameter identification, there are numerical difficulties in identifying the regions of concavity and convexity. In the one parameter case we need only to identify linear functions to cover the nonconvex or nonconcave sections of the nonlinear function whereas in a multiple parameter identification bounding hyperplanes are required.

Chapter 5

Preliminary Control Methods

In the following sections, we develop several preliminary control laws for the placement of the tip of the Terfenol-D transducer illustrated in Figure 1.3. All of the control designs will employ inverse compensation based on one of the three hysteresis models described in Chapter 2 to attenuate the nonlinearities and hysteretic behavior in the Terfenol-D transducer. The limitations of each control scheme will be addressed.

First, a linear adaptive control method utilizing the Preisach hysteresis model (2.17) and corresponding approximate inverse (2.23) will be summarized. This method adaptively tunes the parameters in the approximate inverse to the actual parameter values while tracking a reference response. The second control method discussed is a PID control law combined with inverse compensation based on both the domain wall hysteresis model (2.8) and the free energy hysteresis model (2.37). A PID control design is presented since it is a simple, commonly employed, model independent method. Finally, an optimal LQR control formulation is presented. This is a model-based method which has an extensive mathematical foundation. The PID and LQR control methods will illustrate the deficiencies of control designs which do not incorporate the presence of the inherent disturbances to the Terfenol-D transducer such as hysteretic behavior and sensor noise.

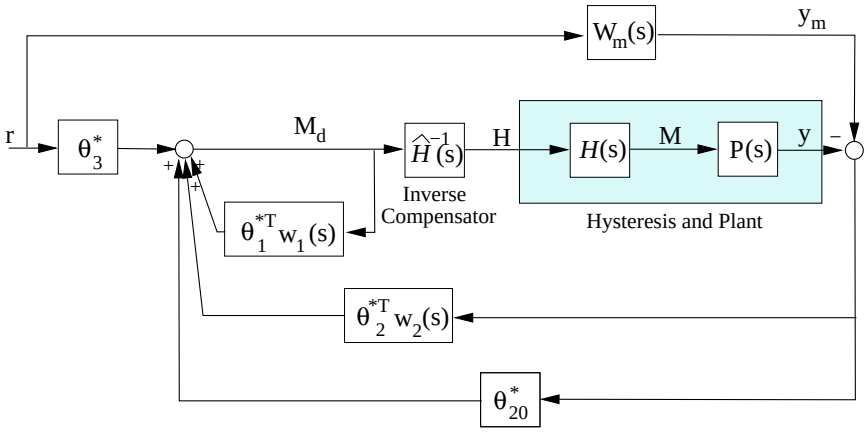

Figure 5.1: Linear adaptive inverse control scheme.

5.1 Linear Adaptive Control

In Chapter 4, a nonlinear parameter estimation algorithm capable of identifying nonlinearly occurring parameters in hysteresis models was developed. The emphasis in this section is the implementation of a linear adaptive control scheme for a system with unknown hysteresis. Here, the Preisach model for a hysteretic material will be utilized to develop the linear adaptive control method because its linear structure allows the outputs of the hysteresis and hysteresis inverse to be represented as linear combinations of the parameters. This ability is crucial to the design of the adaptive inverse approach discussed here. This method was developed by Kokotović and Tao [10, 11] and employs an approximate inverse (2.23) of the Preisach hysteresis model to compensate for the hysteretic effects of the smart material and a modified gradient adaptation law to tune the parameter estimates in the inverse compensator. As was done in Section 2.2.1, we assume that the inverse is parameterized by $\widehat{m}_t(t)$, $\widehat{c}_t(t)$, $\widehat{m}_b(t)$, $\widehat{c}_b(t)$, $\widehat{m}_r(t)$, $\widehat{c}_r(t)$, $\widehat{m}_l(t)$, and $\widehat{c}_l(t)$ and the goal is to drive these estimates

to the true values. During the discussion of the linear adaptive method we shall assume that the parameter estimates are bounded.

As depicted in Figure 5.1, the tracking error is a measure of the difference between the response of our system $P(s)$, given by the second order ODE (3.18), and the response of a reference model $W_m(s) = P_m^{-1}(s)$ to a reference signal $r(t)$. Here $W_m(s)$ is chosen to have dynamics we wish the output of the plant $P(s)$ to emulate and $P_m(s)$ is a stable polynomial with the same relative degree as the linear plant $P(s)$. Since it is a rational transfer function, we can represent $P(s)$ by

$$P(s) = k_p \frac{N(s)}{D(s)} \tag{5.1}$$

where $N(s)$ and $D(s)$ are monic polynomials and k_p is a constant scalar.

Previous adaptive control techniques are inadequate for the smart material transducer application since they are not applicable to nondifferential nonlinearities. The Preisach model (2.17) has sharp corners and therefore is not differentiable. The adaptive control method described in this section is unique in that it is able to express the control error as a linear parameterization in spite of the nondifferentiability of the hysteresis model due in part to the indicator functions defined in the next section [11].

5.1.1 Update Law

To begin, we express the output of the tunable inverse and output of the Preisach straight line hysteresis model as linear functions of the parameters and parameter estimates. To this end, indicator functions are defined to determine the location of the signals in both the hysteresis loop and the hysteresis inverse. Denoting M_d as the control input which is fed into the tunable inverse, H as the output of the inverse and the input to the hysteresis model, and M as the output of the hysteresis model

(see Figure 5.1), the indicator functions are defined as

$$\chi_t(t_k) = \begin{cases} 1, & \text{if } M(t_k) = m_t H(t_k) + c_t \\ 0, & \text{else} \end{cases} \tag{5.2}$$

$$\chi_b(t_k) = \begin{cases} 1, & \text{if } M(t_k) = m_b H(t_k) + c_b \\ 0, & \text{else} \end{cases} \tag{5.3}$$

$$\chi_r(t_k) = \begin{cases} 1, & \text{if } M(t_k) = m_r (H(t_k) - c_r) \\ 0, & \text{else} \end{cases} \tag{5.4}$$

$$\chi_l(t_k) = \begin{cases} 1, & \text{if } M(t_k) = m_l (H(t_k) - c_l) \\ 0, & \text{else} \end{cases} \tag{5.5}$$

$$\chi_d(t_k) = \begin{cases} 1, & \text{if } M(t_k) = m_t H(t_k) + c_d(t_k) \\ 0, & \text{else} \end{cases} \tag{5.6}$$

$$\chi_u(t_k) = \begin{cases} 1, & \text{if } M(t_k) = m_b H(t_k) + c_u(t_k) \\ 0, & \text{else} \end{cases} \tag{5.7}$$

$$\widehat{\chi}_t(t_k) = \begin{cases} 1, & \text{if } H(t_k) = \dfrac{1}{\widehat{m}_t}(M_d(t_k) - \widehat{c}_t) \\ 0, & \text{else} \end{cases} \tag{5.8}$$

$$\widehat{\chi}_b(t_k) = \begin{cases} 1, & \text{if } H(t_k) = \dfrac{1}{\widehat{m}_b}(M_d(t_k) - \widehat{c}_b) \\ 0, & \text{else} \end{cases} \tag{5.9}$$

$$\widehat{\chi}_r(t_k) = \begin{cases} 1, & \text{if } H(t_k) = \dfrac{1}{\widehat{m}_r} M_d(t_k) + \widehat{c}_r \\ 0, & \text{else} \end{cases} \tag{5.10}$$

$$\widehat{\chi}_l(t_k) = \begin{cases} 1, & \text{if } H(t_k) = \dfrac{1}{\widehat{m}_l} M_d(t_k) + \widehat{c}_l \\ 0, & \text{else} \end{cases} \tag{5.11}$$

$$\widehat{\chi}_d(t_k) = \begin{cases} 1, & \text{if } H(t_k) = \dfrac{1}{\widehat{m}_t}(M_d(t_k) - \widehat{c}_d(t_k)) \text{ and } \widehat{c}_b(t_k) < \widehat{c}_d(t_k) < \widehat{c}_t(t_k) \\ 0, & \text{else} \end{cases} \tag{5.12}$$

$$\widehat{\chi}_u(t_k) = \begin{cases} 1, & \text{if } H(t_k) = \dfrac{1}{\widehat{m}_b}(M_d(t_k) - \widehat{c}_u(t_k)) \text{ and } \widehat{c}_b(t_k) < \widehat{c}_u(t_k) < \widehat{c}_t(t_k) \\ 0, & \text{else.} \end{cases} \tag{5.13}$$

For example, if the input to the hysteresis model is such that the resulting magnetization lies on the top half line (see Figure 2.5), then $\chi_t = 1$. One important issue is that at any time t_k, $\widehat{\chi}_t + \widehat{\chi}_b + \widehat{\chi}_r + \widehat{\chi}_l + \widehat{\chi}_u + \widehat{\chi}_d = 1$, so we must not repeatedly count any intersection of the line segments and half-line. For example, if $\widehat{\chi}_t = 1$, then $\widehat{\chi}_r = 0$, and if $\widehat{\chi}_r = 1$, then $\widehat{\chi}_d = 0$. A similar condition holds for the $\chi(t_k)$ functions.

The indicator functions can be used to express the output of the hysteresis loop M as

$$\begin{aligned} M(t_k) = \; & M_d(t_k) + \widehat{\chi}_t(t_k)\,(m_t H(t_k) + c_t - \widehat{\chi}_t(t_k) M_d(t_k)) \\ & + \widehat{\chi}_b(t_k)\,(m_b H(t_k) + c_b - \widehat{\chi}_b(t_k) M_d(t_k)) + \widehat{\chi}_r(t_k)\,(m_r(H(t_k) + c_r) \\ & - \widehat{\chi}_r(t_k) M_d(t_k)) + \widehat{\chi}_l(t_k)\,(m_l(H(t_k) + c_l) - \widehat{\chi}_l(t_k) M_d(t_k)) \\ & + \widehat{\chi}_u(t)\,(m_t H(t_k) + c_u - \widehat{\chi}_u(t_k) M_d(t_k)) + \widehat{\chi}_d(t_k)\,(m_t H(t_k) \\ & + c_d - \widehat{\chi}_d(t_k) M_d(t_k)) + d_1(t_k) \end{aligned} \tag{5.14}$$

where

$$\begin{aligned} d_1(t_k) = \; & (\chi_t(t_k) - \widehat{\chi}_t(t_k))(m_t H(t_k) + c_t) + (\chi_b(t_k) - \widehat{\chi}_b(t_k))(m_b H(t_k) \\ & + c_b) + (\chi_r(t_k) - \widehat{\chi}_r(t_k))(m_r(H(t_k) - c_r)) + (\chi_l(t_k) - \widehat{\chi}_l(t_k)) \\ & (m_l(H(t_k) - c_l)) + (\chi_d(t_k) - \widehat{\chi}_d(t_k))(m_t H(t_k) + c_d(t_k)) \\ & + (\chi_u(t_k) - \widehat{\chi}_u(t_k))(m_b H(t_k) + c_u(t_k)) \; . \end{aligned} \tag{5.15}$$

Note that, with the assumption that the parameters are bounded, $d_1(t_k)$ is bounded. Also, if $(M_d(t_k), H(t_k))$ lies outside the hysteresis inverse loop and $(H(t_k), M(t_k))$ lies outside the hysteresis loop, then $d_1(t_k)$=0. Utilizing the indicator functions, the

output of the approximate inverse can be express as

$$\begin{aligned} H(t_k) = \; & \widehat{\chi}_t \left(\frac{1}{\widehat{m}_t(t_k)} (M_d(t_k) - \widehat{c}_t(t_k)) \right) + \widehat{\chi}_b \left(\frac{1}{\widehat{m}_b(t_k)} (M_d(t_k) - \widehat{c}_b(t_k)) \right) \\ & + \widehat{\chi}_r \left(\frac{1}{\widehat{m}_r(t_k)} (M_d(t_k) - \widehat{m}_r(t_k)\widehat{c}_r(t_k)) \right) + \widehat{\chi}_l \left(\frac{1}{\widehat{m}_l(t_k)} (M_d(t_k) \right. \\ & \left. - \widehat{m}_l(t_k)\widehat{c}_l(t_k)) \right) + \widehat{\chi}_u \left(\frac{1}{\widehat{m}_b(t_k)} (M_d(t_k) - \widehat{c}_u(t_k)) \right) \\ & + \widehat{\chi}_d \left(\frac{1}{\widehat{m}_t(t_k)} (M_d(t_k) - \widehat{c}_d(t_k)) \right). \end{aligned} \tag{5.16}$$

Employing (5.14) and (5.16), we can derive a linear parameterization of the control error $M(t_k) - M_d(t_k)$. To simplify notation, define $\widehat{m_r c_r}(t_k) = \widehat{m}_r(t_k)\widehat{c}_r(t_k)$ and likewise $\widehat{m_l c_l}(t_k) = \widehat{m}_l(t_k)\widehat{c}_l(t_k)$. Since the hysteresis loop is symmetric, the vector of parameters can be defined by

$$\theta_h^* = (m_t, c_t, m_r, m_r c_r)^T \tag{5.17}$$

and the parameters estimates by

$$\theta_h(t_k) = \left(\widehat{m}_t(t_k), \widehat{c}_t(t_k), \widehat{m}_r(t_k), \widehat{m_r c_r}(t_k) \right)^T. \tag{5.18}$$

To represent the control error, we must define the signal

$$\begin{aligned} \omega_h(t_k) \; = \; & \left(- \left(\widehat{\chi}_t(t_k) + \widehat{\chi}_c(t_k) + \widehat{\chi}_b(t_k) \right) H(t_k), \right. \\ & \left. - \left(\widehat{\chi}_t(t_k) - \widehat{\chi}_b(t_k) \right), - \left(\widehat{\chi}_r(t_k) + \widehat{\chi}_l(t_k) \right) H(t_k), \; \widehat{\chi}_t(t_k) - \widehat{\chi}_l(t_k) \right)^T \end{aligned} \tag{5.19}$$

and the parameter error

$$\psi_h(t_k) = \theta_h(t_k) - \theta_h^*. \tag{5.20}$$

Combining (5.14) and (5.16) and employing (5.19) and (5.20), the control error can be expressed as

$$M(t_k) - M_d(t_k) = \psi_h^T(t_k)\omega_h(t_k) + d_h(t_k) \tag{5.21}$$

where

$$d_h(t_k) = d_1(t_k) + \widehat{\chi}_d(t_k)(c_d(t_k) - \widehat{c}_d(t_k)) + \widehat{\chi}_u(t_k)(c_u(t_k) - \widehat{c}_u(t_k)) \ . \tag{5.22}$$

The unknown disturbance $d_h(t_k)$ is bounded since $\widehat{\chi}_l = \widehat{\chi}_r = \widehat{\chi}_u = \widehat{\chi}_d = 0$ for large $H(t_k)$ and $d_1(t_k)$ is bounded and clearly reduces to zero as the parameter error $\psi_h(t_k)$ goes to zero.

Now, the adaptive control law is given by

$$M_d(t_{k+1}) = \theta_1^*\omega_1(t) + \theta_2^*\omega_2(t) + \theta_{20}^* y(t) + \theta_3^* r(t). \tag{5.23}$$

Here $\omega_1(t) = \dfrac{a(s)}{\Lambda(s)}[M_d](t)$ and $\omega_2(t) = \dfrac{a(s)}{\Lambda(s)}[y](t)$ where $a(s) = (1, s, s^2, ..., s^{n-2})^T$. The relative degree of $P(s)$ is denoted by n. The notation $x(t) = T(s)[y](t)$ states that $x(t)$ is the response of the system $T(s)$ to an input $y(t)$. The monic Hurwitz polynomial $\Lambda(s)$ is of degree $n-1$ and the control design gains $\theta_1^*, \theta_2^* \in \mathbb{R}^{n-1}, \theta_{20}^* \in \mathbb{R}$ and $\theta_3^* \in \mathbb{R}$ are chosen to satisfy the Diophantine equation

$$\begin{aligned} \theta_1^* a(s)P(s) + (\theta_2^* a(s) + \theta_{20}^* \Lambda(s))(\theta_3^*)^{-1}N(s) = \\ \Lambda(s)(P(s) - (\theta_3^*)^{-1}\theta_3^* N(s)P_m(s)) \ . \end{aligned} \tag{5.24}$$

To determine the tracking error $e(t) = y(t) - y_m(t)$, where $y_m(t) = W_m(s)[r](t)$ and $y(t) = G(s)[M](t)$, we define

$$F(s) = \theta_3^* W_m(s)\left(1 - \theta_1^* \frac{a(s)}{\Lambda(s)}\right). \tag{5.25}$$

The tracking error can then be written as

$$e(t) = F(s)[\psi_h^T \omega_h](t) - F(s)[d_h](t) \ . \tag{5.26}$$

Note that $F(s)$ is a known, stable and strictly proper transfer function.

To formulate the differential equation utilized in the parameter estimates update law, we first must define the following equations:

$$\zeta_h(t) = F(s)[\omega_h](t) \tag{5.27}$$

$$\xi_h(t) = \theta_h^T(t)\zeta_h(t) - F(s)[\theta_h^T \omega_h](t) \tag{5.28}$$

$$\epsilon_h(t) = e(t) + \xi_h(t). \tag{5.29}$$

Now, we update $\theta_h(t)$ with a modified gradient law given as

$$\dot{\theta}_h(t) = -\frac{\Gamma_h \zeta_h(t)\epsilon_h(t)}{1 + \zeta_h^T(t)\zeta_h(t) + \xi_h^2(t)} - \Gamma_h \sigma(\theta_h, M_h, \sigma_0)\theta_h(t) \tag{5.30}$$

where Γ_h is symmetric positive definite matrix. Here σ is a '*switching sigma*' signal that uses *a priori* knowledge on M_h, an upper bound of the Euclidean norm of θ_h, and a constant parameter $\sigma_0 > 0$, and is given by

$$\sigma = \begin{cases} 0, & \text{if } ||\theta_h(t_k)|| < M_h \\ \sigma_0(\frac{||\theta_h(t_k)||}{M_h} - 1), & \text{if } M_h \leq ||\theta_h(t_k)|| \text{ and } ||\theta_h(t_k)|| < 2M_h \\ \sigma_0, & \text{if } ||\theta_h(t_k)|| \geq 2M_h \ . \end{cases} \tag{5.31}$$

A lemma guaranteeing the boundedness of the parameter estimates ¿from [10] can now be stated.

Lemma 5.1: The adaptive law (5.30) guarantees the following conditions:
1) $\theta_h(t)$, $\dot{\theta}_h(t)$, $(\epsilon_h^2(t)\zeta_h^T(t) + \xi_h^2(t)) \in L_\infty$.
2) For some constants $k_1 > 0$ and $k_2 > 0$ and all $t_2 > t_1 \geq 0$,

$$\int_{t_1}^{t_2} \|\dot{\theta}_h(t)\|^2 dt \leq k_1 + \int_{t_1}^{t_2} \frac{k_2}{1 + \zeta_h^T(t)\zeta_h(t) + \xi_h^2(t)} dt \tag{5.32}$$

and

$$\int_{t_1}^{t_2} \frac{\epsilon_h^2(t)}{1 + \zeta_h^T(t)\zeta_h(t) + \xi_h^2(t)} dt \leq k_1 + \int_{t_1}^{t_2} \frac{k_2}{1 + \zeta_h^T(t)\zeta_h(t) + \xi_h^2(t)} dt \ . \tag{5.33}$$

A proof of Lemma 5.1 can be found in [10]. Lemma 5.1 shows the boundedness of $\theta_h(t)$ and the L_2 properties of the adaptive law (5.30). Finally, it must be shown that all closed loop signal in the adaptive inverse algorithm remain bounded.

Theorem 5.1: If the hysteresis loop is such that $m_t = m_b$, all closed loop signals are bounded.

A proof ensuring the boundedness of all closed loop signals, assuming $m_t = m_b$, can be found in [11].

5.1.2 Numerical Example

In this section, the adaptive control method is implemented to control the position of the tip of a Terfenol-D rod. Recall that the Terfenol-D transducer shown in Figure 1.3 has been modeled as a transfer function $P(s) = k_p(N(s)/D(s))$ with $k_p = \omega$, $N(s) = 1$ and $D(s) = s^2 + ks + c$ where ω, k, and c are given in Table 3.3. The relative degree

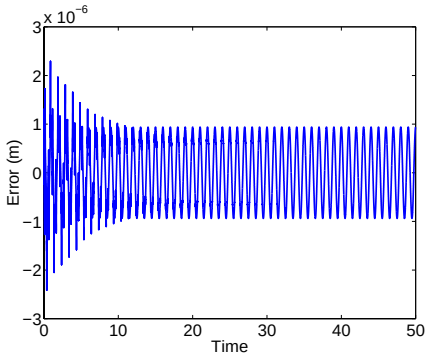

Figure 5.2: Tracking error obtained with linear adaptive control method.

of $P(s)$ is 2 so we take $\Lambda(s) = (s + k)$ and $a(s) = 1$ making

$$\omega_1(t) = \frac{1}{s+k}[u_d](t) \text{ and } \omega_2(t) = \frac{1}{s+k}[y](t). \tag{5.34}$$

The reference model is taken to be $D^{-1}(s)$, yielding

$$W_m(s) = \frac{1}{s^2 + ks + c} \ . \tag{5.35}$$

This implies that the reference signal should be scaled by a factor of ω. Employing the given reference model (5.35), we take $\theta_1^* = \theta_2^* = \theta_{20}^* = 0$ and $\theta_3^* = 1/\omega$ which satisfy the Diophantine equation (5.24). With this choice of parameters, the stable function $F(s) = P(s)$. The parameter values for the Preisach hysteresis model are given in Table 2.2. The remaining adaptive control method parameters are given in Table 5.1.

Figure 5.2 illustrates the effectiveness of the adaptive control method. Figure 5.2 shows the error between the output of the plant and reference signal. The decay in the error corresponds to the convergence of the parameter estimates in the approximate inverse to the true parameter values. The convergence of the parameter estimates $\widehat{\theta}$ is

$\widehat{m}_t(0) = \widehat{m}_b(0)$	1.9785
$\widehat{c}_t(0) = -\widehat{c}_b(0)$	7×10^5
$\widehat{m}_r(0) = \widehat{m}_l(0)$	40.824
$\widehat{c}_r(0) = -\widehat{c}_l(0)$	3.2362×10^3
Γ_h	$\begin{bmatrix} 1 \times 10^{10} & 0 & 0 & 0 \\ 0 & 1 \times 10^{19} & 0 & 0 \\ 0 & 0 & 1 \times 10^{10} & 0 \\ 0 & 0 & 0 & 1 \times 10^{17} \end{bmatrix}$
σ_0	.15
M_h	7×10^5

Table 5.1: Adaptive control method parameters.

illustrated in Figures 5.3a-5.3d. The figures indicate that the parameter estimates are tuned to the actual values. Therefore the control schemes provides a viable method for tracking a reference response while tuning the approximate inverse to the true inverse thereby significantly attenuating the phase delay effects commonly produced by hysteresis.

The linear adaptive control method with a tunable inverse compensator, as proposed by Kokotović and Tao in [10, 11], has proven to be effective in tracking a reference signal in the presence of hysteretic behavior for models having linear parameterizations. A limitation of such a method is the fact that the outputs of the hysteresis and hysteresis inverse must be written as linear combinations of the parameter estimates. Therefore, of the hysteresis models described in Chapter 2, only the Preisach model can be employed with this method. While this formulation of the Preisach model can describe some of the characteristics of a hysteretic material, such as energy loss, it does not accurately describe the nonlinearity of these materials nor does it efficiently quantify minor loops. These problems motivate the investigation

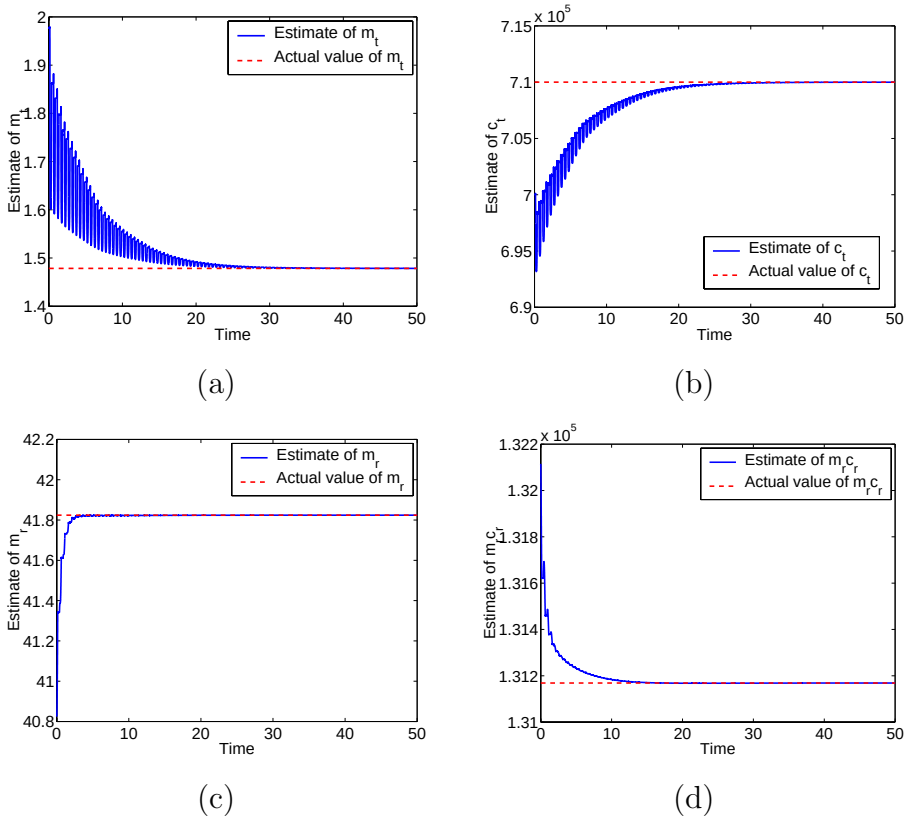

Figure 5.3: Evolutions of the parameters estimates: (a) $\widehat{m}_t$, (b) $\widehat{c}_t$, (c) $\widehat{m}_r$ and (d) $\widehat{m_r c_r}$.

of other control strategies which may be able to incorporate more accurate models of hysteretic behavior, such as the domain wall model (2.8) and the free energy model (2.37).

5.2 PID Control

In the previous section, a Preisach hysteresis model was utilized in the development of a linear adaptive control algorithm to control a magnetostrictive transducer. It was noted that this formulation of the Preisach hysteresis model lacks the ability to

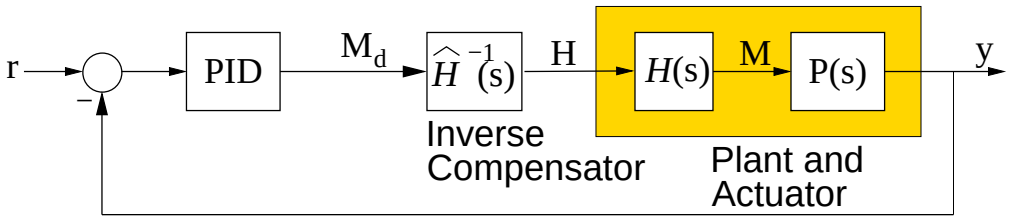

Figure 5.4: PID control formulation.

model the nonlinear behavior of the Terfenol-D. Therefore, it is beneficial to consider control laws which can incorporate other, more accurate, hysteresis models.

This section concentrates on the employment of inverse compensation combined with a PID (Proportional-Integral-Derivative) control law to control the movement of the tip of the Terfenol-D transducer. To begin, the inverse compensator will be constructed using the partial inverse of the domain wall model (2.11). The domain wall model will be employed to simulated the hysteresis inherent in the transducer with the model parameters given in Table 2.1. As indicated in Section 2.1 and illustrated in Figure 2.4, a partial inverse compensator only considers the inverse of the anhysteretic curve and therefore does not diminish the phase delay problem as a full inverse would. Recall that the partial inverse is given as

$$M^{-1} = a\left[tanh^{-1}(\frac{H}{M_s})\right] - \alpha H. \tag{5.36}$$

While the partial inverse compensation alleviates the nonlinear behavior of the Terfenol-D transducer, a PID controller will be utilized to enhance the tracking performance of our system. The standard form of such a controller is given as

$$M_d(t) = K\left[e(t) + \frac{1}{T_i}\int_0^t e(s)ds + T_d\frac{\partial e(t)}{\partial t}\right] \tag{5.37}$$

where K, T_i and T_d are gains to be tuned and $e(t)$ is the error between the reference signal r and the position of the tip of the rod y as depicted in Figure 5.4. The ODE model for the Terfenol-D transducer, given in Section 3.2 by equation (3.18), is denoted by $P(s)$.

The standard method for determining K, T_i and T_d, as described in detail in [3], is to introduce a step input into the system and find the point of maximal slope for the system's response. The parameters are then determined from this slope. However, the standard parameters values for the PID controller must be improved upon for our transducer. A possible explanation for poor tracking performance with the recommended parameters is, in addition to the phase delay caused by the hysteresis, the magnitude of the output is small relative to the input. This means the error needs to be magnified and the integral term should be weighted more to attack the phase delay caused by the inherent hysteresis. Conversely, if the integral term is weighted too highly the controller may overreact to the error. The integral of the error does not change sign until the error has changed sign for an adequate length of time. This integral lag up can cause the feedback control system to be driven to periods of over and under estimation [3].

To fully analyze the PID control method, several control designs utilizing a PID control law will be compared. To begin, we illustrate the effect of the partial inverse compensation by examining the open loop response, i.e., no PID control is employed. The results are plotted in Figure 5.5. Figure 5.5a depicts the commanded and measured position. With no control applied, the error, shown in Figure 5.5b, is significant. For the open loop case, the phase delay between the reference signal and the measured position is not attenuated.

Next, the PID control law is employed without a partial inverse compensator to test the ability of the PID scheme. In particular, the PID controller's ability to attenuate the phase delay is of interest. The parameters utilized in the PID law for the

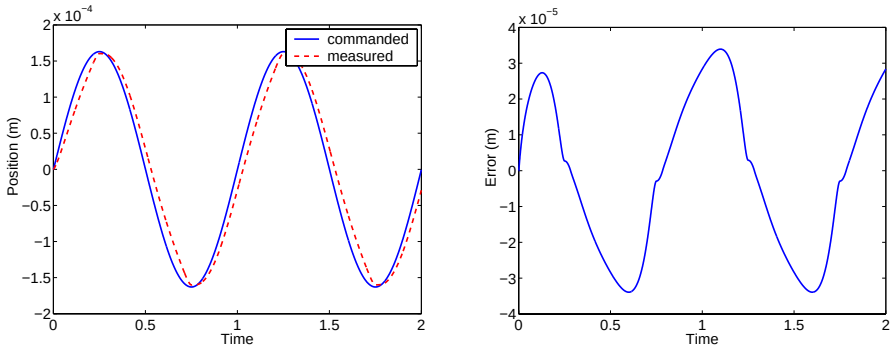

(a) (b)

Figure 5.5: (a) Position, and (b) tracking error for open loop system with partial inverse compensation.

simulation are $T_i = 5 \times 10^{-7}$, $T_d = 2.5 \times 10^{-5}$ and $K = 4.802 \times 10^4$. These values were found by hand tuning the gains until the best level of tracking was achieved. This method of hand tuning is computationally inefficient yet necessary due to the previously discussed problems in the standard gain formulations. Figure 5.6b illustrates an improvement in the tracking error due to the PID feedback control law. Figure 5.6a illustrates the measured and commanded positions and shows that the PID control is able to attenuate much of the phase delay caused by the hysteresis at a low frequency drive with no inverse compensation.

To determine whether including an inverse filter is beneficial, we now combine the partial inverse compensator and the PID control law. The parameters employed for this simulation are $T_i = 7.139 \times 10^{-9}$, $T_d = 7.853 \times 10^{-5}$ and $K = 3.389 \times 10^4$. Figure 5.7 depicts the accurate tracking achieved by the partial inverse combined with a PID control law. Since the partial inverse is algebraic, the computational cost is negligible. Therefore, any improvement in tracking is worth the inclusion of the inverse compensator. After one period, the maximum error with inverse compensation and a PID control law 1.2×10^{-6} m whereas the maximum error without inverse

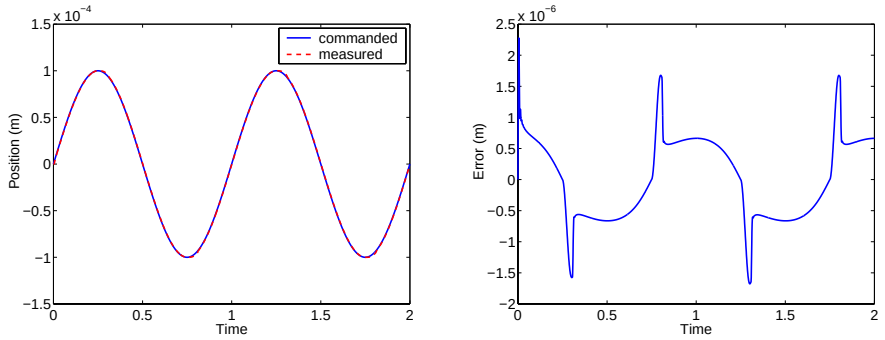

(a) (b)

Figure 5.6: (a) Position, and (b) tracking error for PID control with no inverse compensation.

compensation is 1.7×10^{-6} m. Figure 5.7b shows a great reduction in the phase delay caused by the hysteresis with small errors at the turning point. The error at these changes in the sign of the derivative of the reference signal can be justified by recalling that the PID control law requires a small amount of time to decrease the error after a change in the sign of the error.

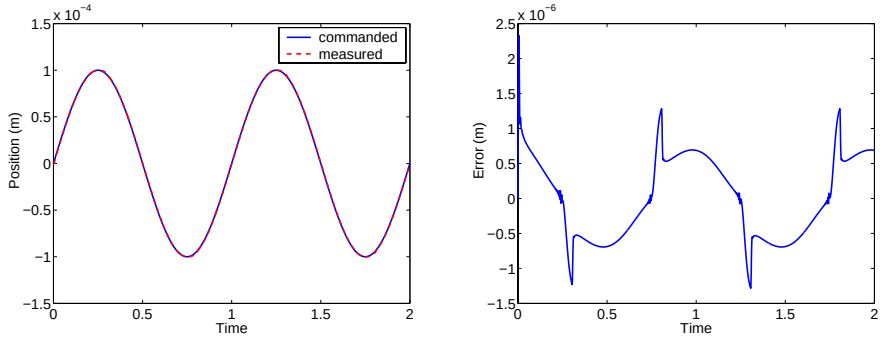

(a) (b)

Figure 5.7: (a) Position, and (b) tracking error for PID control with partial inverse compensation.

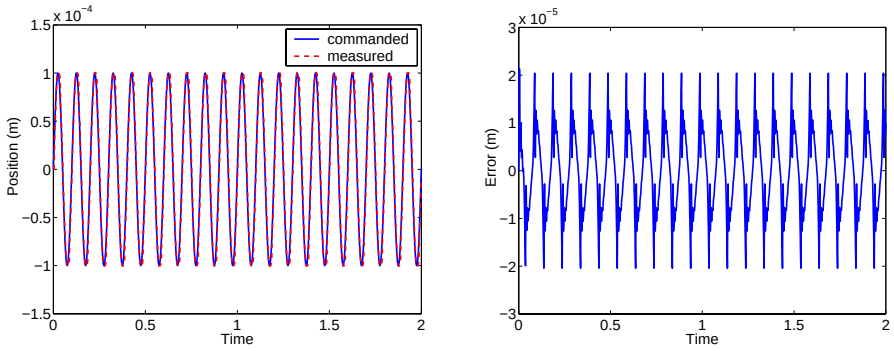

(a) (b)

Figure 5.8: (a) Position, and (b) tracking error for PID control with partial inverse compensation for high frequency tracking.

These numerical results imply significant reduction in the tracking error can be achieved by employing both a partial hysteresis inverse and a PID controller for low drive frequencies. Of concern, however, is the ability of the control design to perform under various operating conditions, in particular high frequency tracking and the presence of sensor noise.

To test the first concern, we increase the frequency of the reference signal to be tracked. Figure 5.8 illustrates the inability of a PID controller combined with a partial inverse compensator to track high frequency reference signals. The tracking error in Figure 5.8b shows a significant increase in the error compared to Figure 5.7b. A large portion of the error occurs at the change of the direction of the reference signal and thus, as the frequency is increased, the PID does not have sufficient time to reduce the error before the direction of the reference signal changes again. PID control is ineffective for tracking reference signals with frequencies which are large compared to the step size taken in the numerical solution or control implementation. As a goal of the control strategy is real time implementation, this puts a significant limit on the utility of PID control.

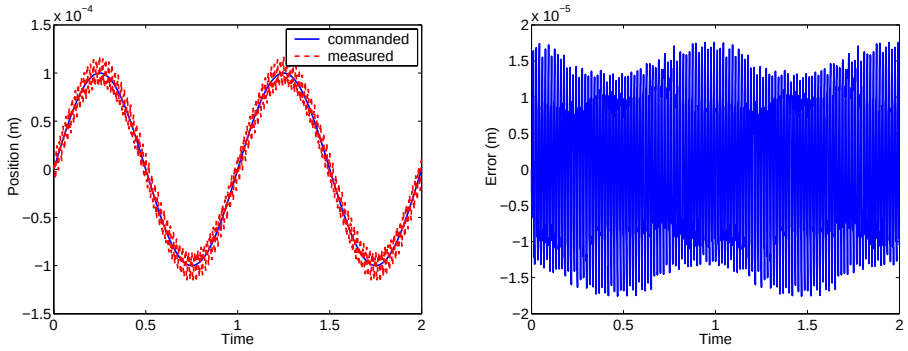

(a) (b)

Figure 5.9: (a) Position, and (b) tracking error a for PID control with partial inverse compensation and sensor noise.

Sensor noise is included in the system to further test the robustness of the PID control law with a partial inverse compensator. As previously stated, robustness with respect to noise is crucial to control design as every sensing device contributes a degree of noise. Figure 5.9 depicts the response of the PID control law with partial inverse filter and the inclusion of noise in the measurement of position of the tip of the Terfenol-D rod. The imposed noise signal has a frequency of 60 Hz and an amplitude of 1×10^{-5} m. It is clear from Figure 5.9 that the PID does not effectively handle the presence of such sensor noise which is approximately 10% of the reference signal. In Figure 5.9b, we note that the error in tracking is on the same order as the noise signal. This occurs because the system is feeding back on the noise in the measurements. While a magnitude of 10% of the measured position may be an over estimate of the amount of sensor noise present in industrial applications, this example illustrates the PID control law's lack of noise rejection. In the next chapter, robust control laws which can attenuate this level of noise will be developed.

It has been shown that the inclusion of the partial inverse compensator (2.11) is beneficial for tracking a low frequency reference signal using a PID control law.

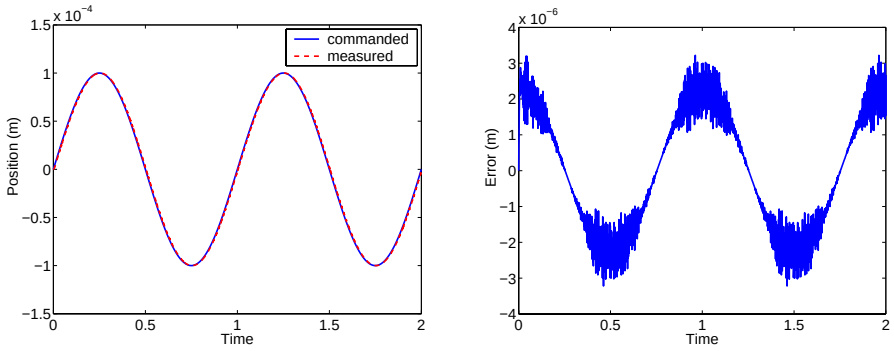

(a) (b)

Figure 5.10: (a) Position, and (b) tracking error and for PID control with full inverse compensation.

For the sake of comparison, the PID control scheme is also applied utilizing the full inverse of the free energy model for hysteretic material (2.37) with the parameters in the model given in Table 2.3. The full inverse compensator provides better attenuation of the phase delay than the partial inverse, yet we must be aware of the error in the linearization of the input by the full inverse compensator as seen in Figure 2.13. The hysteresis inverse utilizes 4 quadratures points, 20 divisions in the coercive field integration, 40 divisions in the effective field integration and a step size of $\Delta H = 1$. These parameters were chosen to allow the possibility of real time implementation. The performance of the PID control law with a full inverse compensator is depicted in Figure 5.10. As was the case with sensor noise, the PID controller doesn't provide sufficient attenuation of the disturbance due to the error cause by the inexact hysteresis inverse. The error signal shown in Figure 5.10b clearly illustrates the effects of the high frequency error caused by the implementation of the full inverse of the free energy model.

In this section, we have shown that the inclusion of a partial inverse compensator based on the anhysteretic component of the domain wall model can be easily

implemented and provides increased tracking performance when combined with a PID control law. While we can provide accurate tracking at low frequencies, certain limitations of the PID control law were illustrated. The PID control formulation had diminished accuracy in high frequency regimes and in the presence of sensor noise. The implementation of a full inverse compensator based on the free energy model was also examined. At low frequencies and ignoring sensor noise, the partial inverse filter performed better than the full inverse filter due to the PID control law's inability to attenuate the high frequency error to the input of the plant. These limitations motivate the study of other, more robust, control strategies.

5.3 LQR Control

The abilities and limitations of a PID control law combined with inverse compensation were summarized in the previous section. In this section, we investigate a linear quadratic tracking feedback control scheme as detailed in [12]. For this section of the dissertation, we employ the full inverse compensator based on the free energy model (2.37) of a hysteretic material. It has been noted that there is error in the linearization provided by the inverse compensator and, in fact, there will always be error in a realistic setting as the free energy model is not an exact representation of the hysteresis measured in an actual transducer. The robustness of an LQR control with respect to the error in the linearization of the hysteresis as well as the inclusion of sensor noise is examined in this section through numerical simulations.

As in previous sections, we denote the reference signal to be tracked by $r(t)$ and the position of the tip of the Terfenol-D rod by $y(t)$. The dynamics of the transducer are represented by the second order ODE (3.17). As detailed in [12], the corresponding

quadratic cost functional is given as

$$\begin{aligned} J(0) = \tfrac{1}{2}\left[y(T) - r(T)\right]^T M \left[y(T) - r(T)\right] \\ + \tfrac{1}{2}\int_0^T \left\{ \left[y(t) - r(t)\right]^T Q \left[y(t) - r(t)\right] + u^T R u \right\} \, dt. \end{aligned} \tag{5.38}$$

Here $u(t)$ is the control input, M and Q are symmetric positive definite matrices and R is a symmetric positive semi-definite matrix.

Following a standard optimal control strategy of appending the system model to the cost functional with Lagrange multipliers as described in [12], the state equation, costate equation, stationary condition and boundary conditions can be formulated.

The state equation is given by

$$\dot{x} = Ax + Bu \tag{5.39}$$

where A and B are given by the state space representation of the transducer as detailed in Section 3.2. The costate equation is given by

$$-\dot{\lambda} = A^T \lambda + C^T Q C x - C^T Q r \tag{5.40}$$

where C is the observation matrix of the transducer system and the stationary condition is specified as

$$0 = B^T \lambda + Ru. \tag{5.41}$$

The boundary conditions can now be given by

$$\begin{aligned} x(0) \text{ is given} \\ \lambda(T) = C^T M \left[y(T) - r(T)\right]. \end{aligned} \tag{5.42}$$

According to the stationary condition (5.41), the optimal feedback can be formulated as

$$u(t) = -R^{-1}B^T\lambda(t). \tag{5.43}$$

Substituting (5.43) into (5.39) yields the differential equation

$$\dot{x} = Ax - BR^{-1}B^t\lambda. \tag{5.44}$$

Using the sweep method [12], the optimal linear quadratic tracking feedback laws can be expressed as

$$\begin{aligned} u(t) &= -K(t)x(t) + R^{-1}B^T v(t) \\ K(t) &= R^{-1}B^T S(t) \\ -\dot{S}(t) &= A^T S(t) + S(t)A - S(t)BR^{-1}B^T S(t) + C^T QC \\ S(T) &= C^T P(T)C \\ -\dot{v}(t) &= (A - BK)^T v(t) + C^T Qr(t) \\ v(T) &= C^T Mr(T)\ . \end{aligned} \tag{5.45}$$

For our purposes, given a final time T, the control gains K and v can be computed off-line. For the simulation results, the final time was take as two periods of the reference signal. Suboptimal techniques to reduce the amount of storage can be employed [12], but since we are concerned with illustrating the limitations of linear quadratic tracking we shall omit these techniques.

First, we employ a linear quadratic tracking formulation for the transducer with the hysteresis omitted to provide a basis for comparison. This corresponds to an exact cancellation of the hysteretic effects by the inverse compensator. The gains in the cost functional (5.38) were taken as $P = 1 \times 10^5$, $Q = 1 \times 10^{17}$ and $R = 1 \times 10^{-14}$. These gains were found by hand-tuning, in the same manner as the PID gains in the

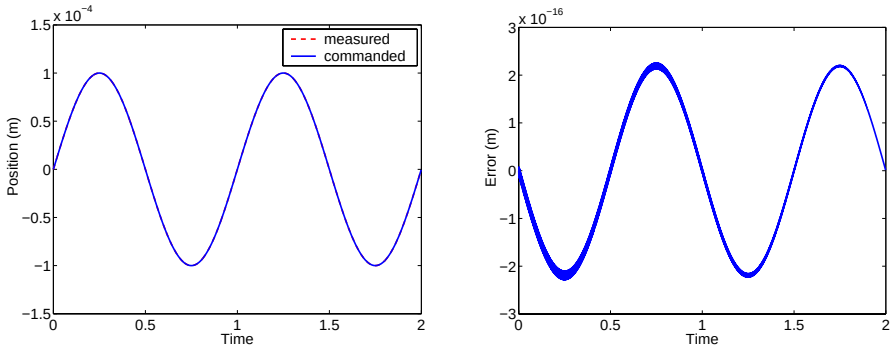

(a) (b)

Figure 5.11: (a) Position, and (b) tracking error for a linear quadratic tracking control law with no hysteresis present.

previous section. Figure 5.11 illustrates the abilities of a linear quadratic tracking method. The control law designed provides extremely accurate tracking when no disturbances to the system are included as can be seen by the error in Figure 5.11b.

As this situation is unreasonable, we include the full inverse compensator and the free energy model for the hysteresis (2.37). The parameters utilized for the hysteresis model are given in Table 2.3. The hysteresis inverse is computed utilizing 4 quadratures points, 20 divisions in the coercive field integration, 40 divisions in the effective field integration and a step size of $\Delta H = 1$. These parameters are chosen to allow the possibility of real time implementation of the inverse compensation LQR control strategy, sacrificing accuracy for computational speed (see Figure 2.13). The gain matrices are taken to be the same as in the previous simulation. Figure 5.12 displays the results of including the hysteresis and inverse filter. The effects of the error in the linearization of the hysteresis are evident in Figure 5.12b and are similar to the results obtained with a PID control method, depicted in Figure 5.10. Although the inverse filter creates relatively small errors, the linear quadratic tracking method does not accommodate these errors.

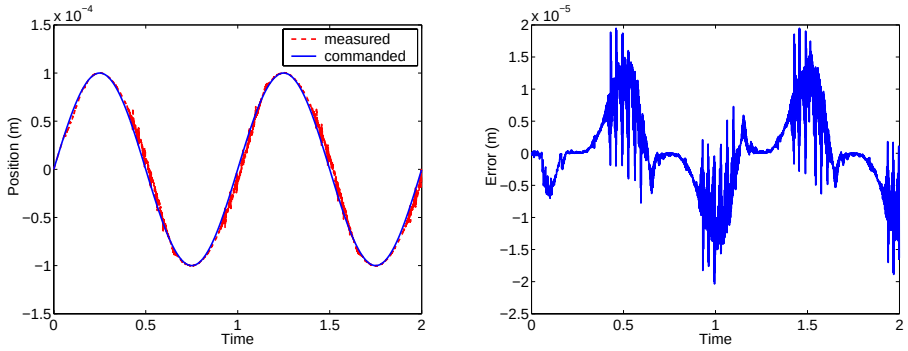

(a) (b)

Figure 5.12: (a) Position, and (b) tracking error for a linear quadratic tracking control law with inverse compensation.

As was seen with the PID control law, the linear quadratic tracking method is unable to attenuate any noise in the measurement of the position of the tip of the Terfenol-D rod. The results of a simulation with sensor noise included are illustrated in Figure 5.13. The noise signal has frequency of a 60 Hz and magnitude 1×10^{-5} m, and the same hysteresis and hysteresis inverse model parameters and gain matrices are employed as in the previous example. The error shown in Figure 5.13b is on the same order as the noise signal since the linear quadratic tracking method feeds back on the noise, much the same as the PID control method.

5.4 Concluding Remarks

The first section in this chapter demonstrated a linear adaptive control technique utilizing the straight line Preisach hysteresis model. The method was shown to provide accurate tracking of a reference response and tune the parameters in the approximate inverse to the actual parameter values. This method is restricted to employing the straight line Preisach hysteresis model and corresponding inverse and therefore

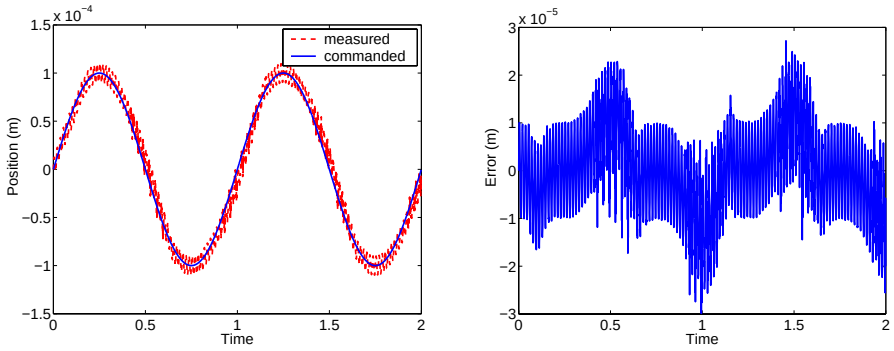

(a) (b)

Figure 5.13: (a) Position, and (b) tracking error for a linear quadratic tracking control law with hysteresis compensation and sensor noise.

may lack the ability to achieve the required accuracy depending on the given criteria. The linear adaptive control technique is best suited for magnetostrictive systems with moderate performance requirements or other problems in which the hysteresis can be more accurately described by the straight line Preisach model such as gear systems [11].

PID and LQR control techniques were investigated for the control of the Terfenol-D transducer. Inverse compensation methods incorporated into the control system proved to improve the performance of PID control while an LQR optimal control method was unable to provide accurate tracking for the system due to the inherent hysteresis in the actuator. The limitations of the PID and linear quadratic tracking schemes to attenuate disturbances in the system motivate the investigation of robust control laws which consider the existence of external disturbances and seek to minimize their effects on tracking performance. Robust control designs capable of compensating for external disturbances will be investigated in the next chapter.

Chapter 6

Robust Control Methods

We illustrated in the previous chapter the deficiencies in robustness of several control methods. The inherent hysteresis in the magnetostrictive material leads to a disturbance in the control system which can not be ignored in the control design even if an inverse compensator is employed. This implies that the control design must accommodate a certain level of error in the input to the plant. It is also necessary to attenuate the effects of any sensor noise in the measurements of the position of the tip of the Terfenol-D rod. These requirements can be met by employing robust control designs utilizing an inverse compensator.

We will summarized three techniques for the synthesis of a robust controller. The first two control design employ a single measure of robustness to the entire system. We will describe the design of an H_2 optimal controller and an H_∞ sub-optimal controller. A multiobjective control technique which is capable of combining several measure of robustness with respect to the different performance criteria is also discussed in this chapter.

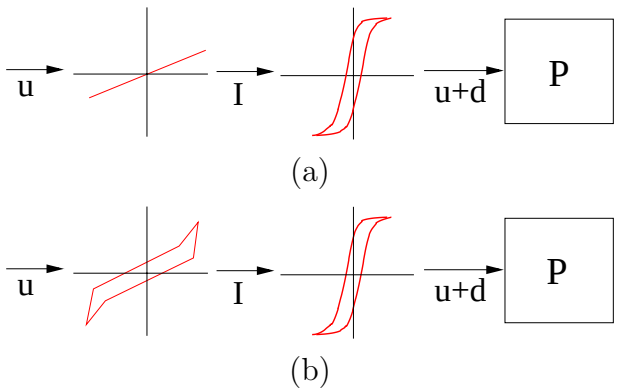

Figure 6.1: Two control design methods employing (a) a scaling factor, and (b) an inverse compensator based on the free energy hysteresis model (2.37).

6.1 H_2 and H_∞ Designs

When constructing robust control designs, we consider two control design systems employing different filters to the input of the plant. First, a constant scaling factor will be employed to attenuate the scaling difference from the input of the hysteresis to the output. This method is illustrated in Figure 6.1a. The signal which is fed into the plant P consists of the prescribed input signal u and the error d created by the hysteresis loop. The scaling factor will not accommodate the nonlinear hysteretic behavior of the magnetostrictive material as is illustrated by the phase diagram of the input signal u and the output of the hysteresis $u + d$ depicted in Figure 6.2a.

Secondly, an inverse compensator based on the free energy hysteresis model (2.37) will be employed to attenuate the hysteresis inherent in the Terfenol-D transducer.This method is depicted in Figure 6.1b. The phase diagram of u and $u + d$ in Figure 6.2b depicts a nearly linear relationship. This reflects the benefit of employing an inverse filter based on the hysteresis model. Recall from Section 2.3.2 that the relationship between u and $u + d$ is not actually linear and there is error in the linearization of the hysteresis by the inverse compensator as shown in Figure 2.13. Both of these

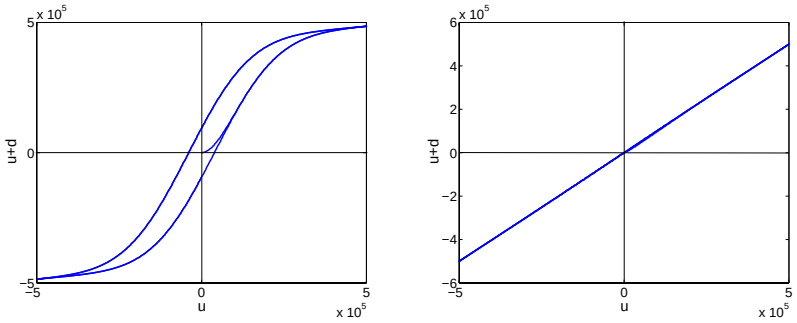

(a) (b)

Figure 6.2: Phase diagram of u and $u+d$ for (a) a scaling factor, and (b) an inverse compensator based on the free energy hysteresis model (2.37).

design methods will be implemented to determine whether the inclusion of an inverse compensator based on the free energy hysteresis model (2.37) provides a significant increase in the control performance for a Terfenol-D transducer.

6.1.1 System Representation

Figure 6.3 depicts the block diagram for the control design system which we consider. In the diagram, P represents the transducer model given by the transfer function (3.18) and y denotes the position of the tip of the Terfenol-D rod. The signal to be tracked is denoted by r and the signal d represents the error to the input of the plant as discussed above. Noise in the measurement of y is separated into two signals, s and n. We assume a 60 Hz noise signal due to the sensing apparatus which is represented by s. The signal n represents higher frequency noise which may be attributed to the sensing device, other external disturbances or, in a numerical simulation, numerical noise. These two signals are separated since we wish to weight them independently. The output signals e and $\widehat{u}$ denote the weighted tracking error and weighted output of the controller K, respectively. Here W_u, W_d, W_e, W_r, W_s and W_n

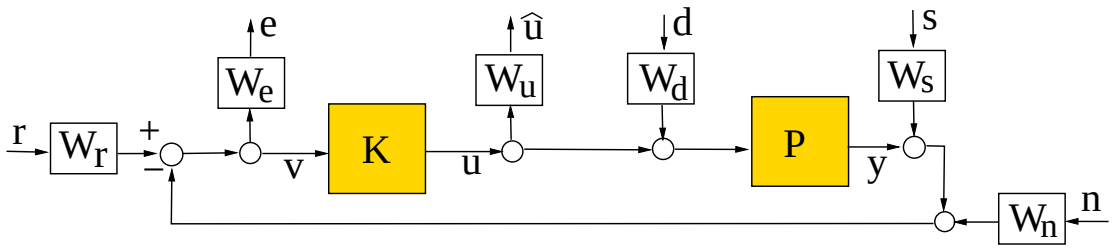

Figure 6.3: Robust control design system incorporating error created by the inherent hysteresis and sensor noise in the transducer.

are weighting functions chosen to maximize the performance of the controller utilizing *a priori* knowledge of the characteristics of the corresponding signals as detailed in Section 6.1.3.

We now represent the transfer functions of the open loop system. The maps from the inputs r, d, s and n to the outputs $\widehat{u}$, e and v are given by

$$\begin{aligned} v &= W_r[r] - (P[W_d[d] + u] + W_n[n] + W_s[s]) \\ &= W_r[r] - P[W_d[d]] - W_n[n] - W_s[s] - P[u] \\ e &= W_e[v] \\ \widehat{u} &= W_u[u] \ . \end{aligned} \tag{6.1}$$

Denoting the transfer function matrix from the inputs r, d, n, s and u to the outputs e, $\widehat{u}$, and v as G, we have

$$G = \begin{bmatrix} W_e W_r & -W_e P W_d & -W_e W_n & -W_e W_s & -W_e P \\ 0 & 0 & 0 & 0 & W_u \\ W_r & -P W_d & -W_n & -W_s & -P \end{bmatrix} . \tag{6.2}$$

The closed loop system can subsequently be represented as a linear fractional transformation as shown in Figure 6.4.

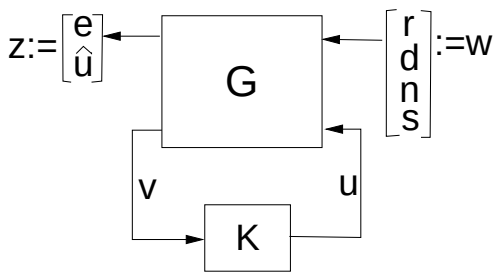

Figure 6.4: Linear fractional transformation (LFT) representation of the transducer model.

To standardize the system formulation to fulfill the assumptions of the theorems guaranteeing the existence of optimal or sub-optimal controllers, we chose a class of weighting functions W_u which have a nonzero D matrix in the corresponding state space representation. The state space representation of either W_n or W_s is required to have a nonzero D matrix and W_e should satisfy $D = 0$. For this selection of weighting functions, the open loop system can be partitioned as

$$G(s) = \left[\begin{array}{c|cc} A & B_1 & B_2 \\ \hline C_1 & 0 & D_{12} \\ C_2 & D_{21} & 0 \end{array}\right] = \begin{bmatrix} G_{11} & G_{12} \\ G_{21} & G_{22} \end{bmatrix} \tag{6.3}$$

where

$$\begin{aligned} G_{11} &= \left[\begin{array}{c|c} A & B_1 \\ \hline C_1 & 0 \end{array}\right], \quad G_{12} = \left[\begin{array}{c|c} A & B_2 \\ \hline C_1 & D_{12} \end{array}\right] \\ G_{21} &= \left[\begin{array}{c|c} A & B_1 \\ \hline C_2 & D_{21} \end{array}\right], \quad G_{22} = \left[\begin{array}{c|c} A & B_2 \\ \hline C_2 & 0 \end{array}\right] \end{aligned} \tag{6.4}$$

represent the transfer functions from w to z, u to z, w to v, and u to v, respectively, as depicted in Figure 6.4.

We make the following assumptions on our system:

1. $(A,\ B_1)$ is controllable and $(C_1,\ A)$ is observable.

2. $(A,\ B_2)$ is stabilizable and $(C_2,\ A)$ is detectable.

3. $D_{12} = \begin{bmatrix} 0 \\ I \end{bmatrix}$ and $D_{21} = [\ 0\ I\ ]$.

4. $\begin{bmatrix} A - j\omega I & B_2 \\ C_1 & D_{12} \end{bmatrix}$ has full column rank for all ω.

5. $\begin{bmatrix} A - j\omega I & B_1 \\ C_2 & D_{21} \end{bmatrix}$ has full row rank for all ω.

Assumption 2 is necessary to guarantee the existence of a stabilizing controller. Assumptions 4 and 5 together with 2 guarantee the existence of solutions to the corresponding Riccati equations. Assumption 3 ensures the H_2 and H_∞ problems are nonsingular. If D_{12} has full column rank and D_{21} has full row rank but they do not satisfy Assumption 3, a normalizing procedure can be performed as described in [26].

6.1.2 Minimal realization

There are only two internal states in the model for the magnetostrictive transducer given in (3.18) yet the inclusion of several weighting functions can greatly increase the number of states in the system. To simplify the numerics of the control formulation,

it is beneficial to remove unobservable and uncontrollable states from the open-loop system. To this end, we define the open loop system as

$$G = \left[\begin{array}{c|c} A & \overline{B} \\ \hline \overline{C} & D \end{array}\right] \tag{6.5}$$

where

$$\overline{B} = [B_1 \; B_2], \quad \overline{C} = \begin{bmatrix} C_1 \\ C_2 \end{bmatrix} \quad \text{and } D = \begin{bmatrix} 0 & D_{12} \\ D_{21} & 0 \end{bmatrix}. \tag{6.6}$$

Suppose there exists a matrix

$$P = P^* = \left[\begin{array}{c|c} P_1 & 0 \\ \hline 0 & 0 \end{array}\right] \tag{6.7}$$

such that $AP + PA^* + \overline{BB}^* = 0$. Partitioning G as

$$G = \left[\begin{array}{cc|c} A_{11} & A_{12} & \overline{B}_1 \\ A_{21} & A_{22} & \overline{B}_2 \\ \hline \overline{C}_1 & \overline{C}_2 & D \end{array}\right], \tag{6.8}$$

we can define a controllable realization of G as

$$G_c = \left[\begin{array}{c|c} A_{11} & \overline{B}_1 \\ \hline \overline{C}_1 & D \end{array}\right]. \tag{6.9}$$

Similarly, we can remove the unobservable states from the open loop system. Suppose there exists a matrix

$$Q = Q^* = \left[\begin{array}{c|c} Q_1 & 0 \\ \hline 0 & 0 \end{array}\right] \tag{6.10}$$

such that $A_{11}^* Q + Q A_{11} + \overline{C}_1^* \overline{C}_1 = 0$. Partitioning G_c as

$$G_c = \left[\begin{array}{cc|c} \widehat{A}_{11} & \widehat{A}_{12} & \widehat{B}_1 \\ \widehat{A}_{21} & \widehat{A}_{22} & \widehat{B}_2 \\ \hline \widehat{C}_1 & \widehat{C}_2 & D \end{array}\right], \tag{6.11}$$

a controllable and observable realization of G can be given as

$$G_{co} = \left[\begin{array}{c|c} \widehat{A}_{11} & \widehat{B}_1 \\ \hline \widehat{C}_1 & D \end{array}\right]. \tag{6.12}$$

Here, G_{co} is called a minimal realization of the system G. This provides a method for eliminating uncontrollable and unobservable states from the open loop system which aides in the formulation of the controller by reducing the size of the Riccati equations to be solved. For a more detailed description of minimal realizations see [26].

6.1.3 Weighting Functions

The majority of effort in designing a robust controller lies in the choice of the weighting functions. Discussions on techniques for choosing these function can be found in [13, 26]. The frequency of the noise s can be accurately determined for the sensor measuring the position of the tip of the Terfenol-D rod. The weight W_s is chosen to heavily weight frequencies in a bandwidth around the expected noise frequency and

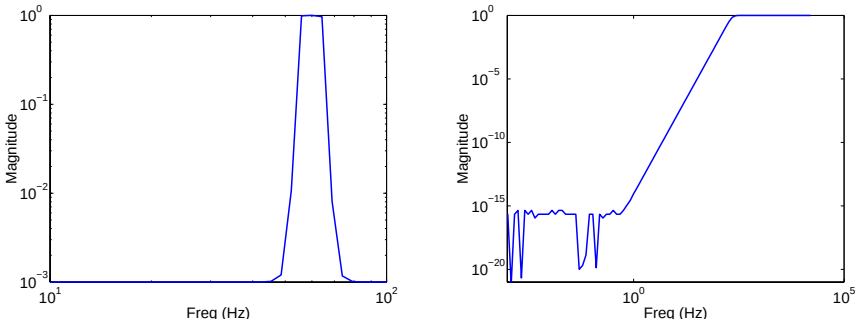

(a) (b)

Figure 6.5: Frequency response of (a) W_s, and (b) W_n.

assign low weights to frequencies above and below the specified bandwidth. For the simulations, a noise frequency of 60 Hz is added to the system and, therefore, W_s is taken to be a sixth-order pass-band Chebyshev filter with a bandwidth of 10 Hz centered at 60 Hz. An n^{th} order Chebyshev filter is a system whose frequency response function satisfies

$$|H_{cb}(\omega)| = \frac{1}{1 + \epsilon_p C_n^2 \left(\frac{\omega}{\omega_s}\right)} \tag{6.13}$$

where ω_s is the sampling frequency, ϵ_p is a parameter which controls the speed of the roll-off, and the polynomials C_n are the n^{th} order Chebyshev polynomials defined by the recursion

$$C_0(\omega) = 1, \quad C_1(\omega) = \omega C_0(\omega) \quad C_{n+1}(\omega) = 2\omega C_n(\omega) - C_{n-1}(\omega). \tag{6.14}$$

Recall that W_s or W_n was required to have a nonzero D matrix in the state space realization. The Chebyshev filter W_s is appended to force a nonzero D to satisfy this requirement. The frequency response of W_s is illustrated in Figure 6.5a.

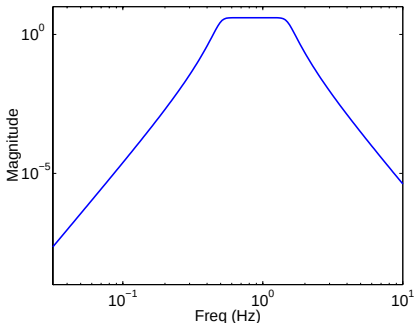

Figure 6.6: Frequency response of W_r.

To weight high frequency noise, W_n is taken to be a high-pass filter. The fourth-order Butterworth filter, plotted in Figure 6.5b, is employed in the numerical simulations. An n^{th} order Butterworth filter is a system where the frequency response function satisfies

$$|H_{bw}(\omega)| = \frac{1}{\sqrt{1 + \left(\frac{\omega}{\omega_s}\right)^{2n}}}. \tag{6.15}$$

Again, ω_s denotes the sampling frequency. A detailed discussion on Chebyshev and Butterworth filters is provided in [13].

The weight W_r is taken as a sixth-order pass-band Chebyshev filter. Since the frequency of the reference signal r is known to be 1 Hz, we can design W_r to have a narrow bandwidth which is taken as 1 Hz centered at 1 Hz. The frequency response of W_r is shown in Figure 6.6.

The weighting function W_d employed in the numerical simulations depends on whether the scaling factor or the inverse compensator is utilized in the control system. To determine W_d, a signal with the same frequency as the reference signal was applied to the given filter and then fed into the free energy hysteresis model. The Fourier transform of the output of the hysteresis model was then analyzed to determine W_d. For simulations employing a scaling factor, the weight W_d is taken as a fourth-order

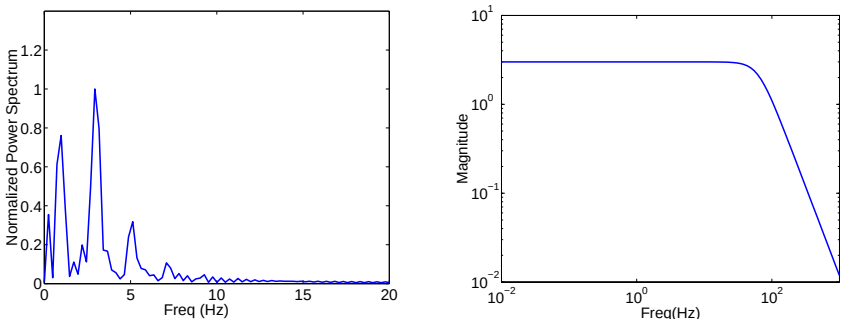

(a) (b)

Figure 6.7: (a) Power spectrum of d, and (b) frequency response of W_d for linear scaling factor.

low-pass Butterworth filter with a cut-off frequency of 10 Hz. This choice of W_d reflects the significant frequencies in the power spectrum of d for the employment of a scaling factor. The power spectrum of d and the frequency response of W_d, in this case, are depicted in Figure 6.7.

Figure 6.8a illustrates the power spectrum of the disturbance d if the inverse compensator based on the free energy hysteresis model is employed. From this figure, it is clear that W_d should weight frequencies below 350 Hz heavily. Therefore, W_d is taken as a low-pass Butterworth filter with a cut-off frequency of 400 Hz. The frequency response of W_d is shown in Figure 6.8b. Higher order filters could be used if a steeper roll-off outside of the frequency band is desired although we have chosen to limit the number of states in the state space representation of our open loop system.

The weighting function on the error signal is specified as $W_e = \dfrac{\gamma_e}{s + \epsilon_e}$ with $\gamma_e = 3.2 \times 10^6$ and $\epsilon_e = 1 \times 10^{-8}$. An integrator is chosen to prevent the error from achieving steady state at a nonzero value and the pole was shifted slightly off zero to ensure that the controller is realizable. We take the weighting function on the controller output to be $W_u = 5 \times 10^{-6}$. Since we do not experience any problems

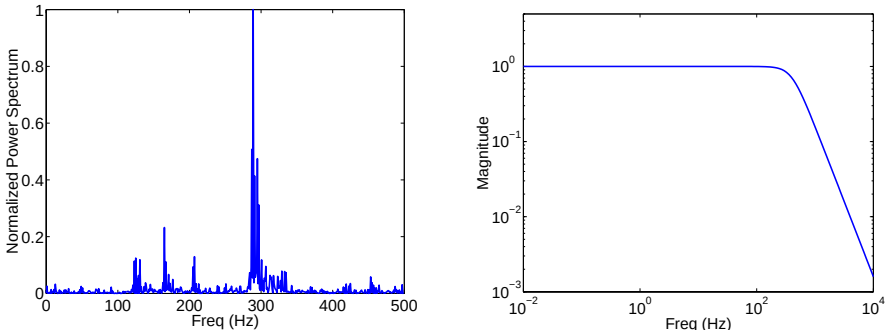

(a) (b)

Figure 6.8: (a) Power spectrum of d, and (b) frequency response of W_d for inverse compensation based on free energy hysteresis model.

with saturation, or other such effects, we minimally weight $\widehat{u}$ to focus the controller on tracking and disturbance rejection. Note that the functions W_e and W_u satisfy the requirement placed on them in Section 6.1.1, i.e., $D = 0$ in the state space realization of W_e and $D = 5 \times 10^{-6}$ in the realization of W_u.

6.1.4 H_2 Optimal Control Design

Now that the open loop system has been represented and the weighting functions have been chosen, we proceed by designing a controller which minimizes a given norm of the closed loop system. To begin, we consider the H_2 norm of the closed loop system T given by

$$\|T\|_2^2 = \frac{1}{2\pi} \int_{-\infty}^{\infty} \text{trace}\left[T^*(i\omega)T(i\omega)\right] d\omega. \tag{6.16}$$

Employing the notation defined in (6.4), the design of the optimal H_2 controller incorporates two Hamiltonian matrices

$$H_2 = \begin{bmatrix} A - B_2 R_1^{-1} D_{12}^* C_1 & -B_2 R_1^{-1} B_2^* \\ -C_1^*(I - D_{12} R_1^{-1} D_{12}^*) C_1 & -(A - B_2 R_1^{-1} D_{12}^* C_1)^* \end{bmatrix} \tag{6.17}$$

and

$$J_2 = \begin{bmatrix} (A - B_2 R_1^{-1} D_{12}^* C_1)^* & -C_2^* R_2^{-1} C_2 \\ -B_1(I - D_{21}^* R_2^{-1} D_{21}) B_1^* & -(A - B_2 R_1^{-1} D_{12}^* C_1) \end{bmatrix} \tag{6.18}$$

where $R_1 = D_{12}^* D_{12} > 0$ and $R_2 = D_{21} D_{21}^* > 0$.

These Hamiltonian matrices give rise to two Riccati equations

$$\begin{aligned} (A - B_2 R_1^{-1} D_{12}^* C_1)^* X_2 + X_2(A - B_2 R_1^{-1} D_{12}^* C_1) + X_2(-B_2 R_1^{-1} B_2^*) X_2 \\ -C_1^*(I - D_{12} R_1^{-1} D_{12}^*) C_1 = 0 \end{aligned} \tag{6.19}$$

and

$$\begin{aligned} (A - B_2 R_1^{-1} D_{12}^* C_1) Y_2 + Y_2(A - B_2 R_1^{-1} D_{12}^* C_1)^* + Y_2(-C_2^* R_2^{-1} C_2) Y_2 \\ -B_1(I - D_{21}^* R_2^{-1} D_{21}) B_1^* = 0. \end{aligned} \tag{6.20}$$

Once the Riccati equations have been defined, the following theorem from [26] guaranteeing an H_2 optimal controller can be employed.

Theorem 6.1: There exists a unique controller which minimizes the H_2 norm of the closed loop system if:

1. $H_2 \in$dom(Ric) and $X_2 :=$Ric$(H_2) > 0$

2. $J_2 \in$dom(Ric) and $Y_2 :=$Ric$(J_2) > 0$.

The H_2 optimal controller is given by

$$K \equiv \left[\begin{array}{c|c} A_2 & -L_2 \\ \hline F_2 & 0 \end{array}\right] \tag{6.21}$$

where

$$A_2 \equiv A + B_2F_2 + L_2C_2, \quad F_2 \equiv -R_1^{-1}(B_2^*X_2 + D_{12}^*C_1),$$

$$L_2 \equiv -(Y_2C_2^* + B_1D_{21}^*)R_2^{-1}. \tag{6.22}$$

Assumptions 2, 3 and 4 from Section 6.1.1 guarantee that $H_2 \in$dom(Ric) and Assumptions 1, 3 and 5 guarantee that $J_2 \in$dom(Ric). See [26] for a detailed proof.

The numerical results for the H_2 robust control laws are now presented. All of the following results include a noise signal s with a frequency of 60 Hz and magnitude of 1×10^{-5} m which is approximately 10% of the signal. The free energy model (2.37) is utilized to simulate the inherent hysteresis with the model parameters given in Table 2.3.

To determine the most effective control strategy, three examples will be examined. First, the H_2 controller will be designed for a system with no hysteresis present. Then a system with inherent hysteresis is considered. We will investigate the performance of an inverse compensator combined with an H_2 control designed without the consideration of a disturbance to the input d. Next, an H_2 controller designed with the consideration of inherent hysteresis and the inclusion of a scaling factor is presented. Finally, the controller is designed under the consideration of the inherent hysteresis and the inverse compensator based on the free energy hysteresis model.

Example 1a. To begin, we examine the performance of the H_2 formulation. For the sake of comparison, the performance of an H_2 robust control designed without

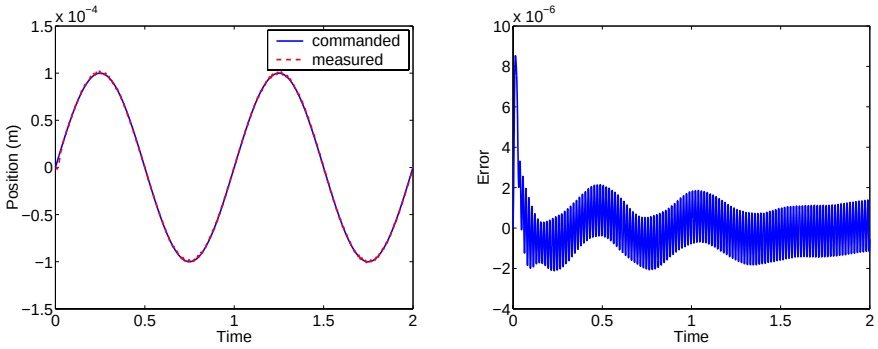

(a) (b)

Figure 6.9: H_2 optimal control results for a system with no hysteresis present. (a) Tracking response, and (b) error.

including a disturbance d at the input to the plant in the design system is examined. If the hysteresis is omitted, or equivalently, the inverse filter is an exact inverse of the hysteretic behavior, the sensor noise can be significantly reduced. Figure 6.9 illustrates the performance of an H_2 control design with no hysteresis considered in the design or simulation. The error, depicted in Figure 6.9b, shows that a significant attenuation of the sensor noise is achieved and a tracking error within 2 microns is reached. It is noted that the H_2 optimal control design is equivalent to an LQR optimal control design applied to the transducer system incorporating the reference signal r and the sensor noise n as inputs and the weighted error e and control output $\widehat{u}$ as outputs of the system [26].

Example 1b. Next, we include the inverse compensator based on the free energy hysteresis model and the free energy hysteresis model in the simulation of the controller design without consideration of a disturbance d. Figure 6.10 clearly shows the effects

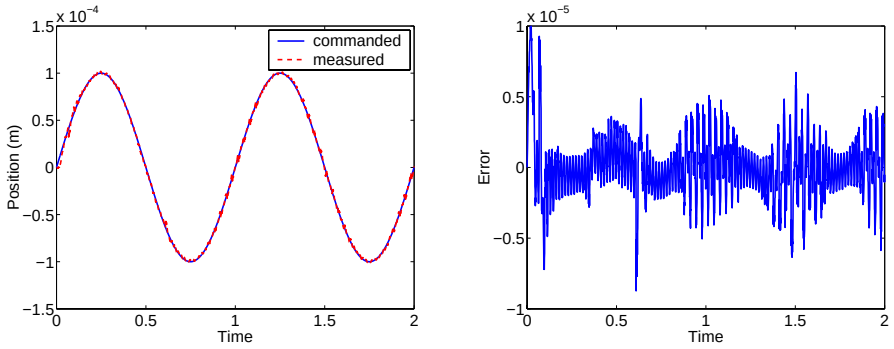

(a) (b)

Figure 6.10: H_2 optimal control results for a controller designed with no consideration of error due to hysteresis. The controller was applied to a system with hysteresis which employed an inverse compensator based on the free energy model (2.37). The (a) tracking response, and (b) error.

of not considering robustness with respect to the disturbance d in the control formulation if there is an error to the input of the plant caused by inherent hysteresis. The error, shown in Figure 6.10b, illustrates the insufficient attenuation of the disturbance to the input of the plant. This example demonstrates the necessity of considering an error to the input of the plant in the control design system for a hysteretic transducer.

The following two examples illustrate the benefit of including the disturbance d in the control design.

Example 1c. Initially, we consider the constant scaling factor and employ the corresponding weighting function W_d in the controller design. Figure 6.11a illustrates the inability of this method to attenuate the hysteretic behavior. The controller is not sufficiently robust to reject the hysteresis retained in this case. The phase delay

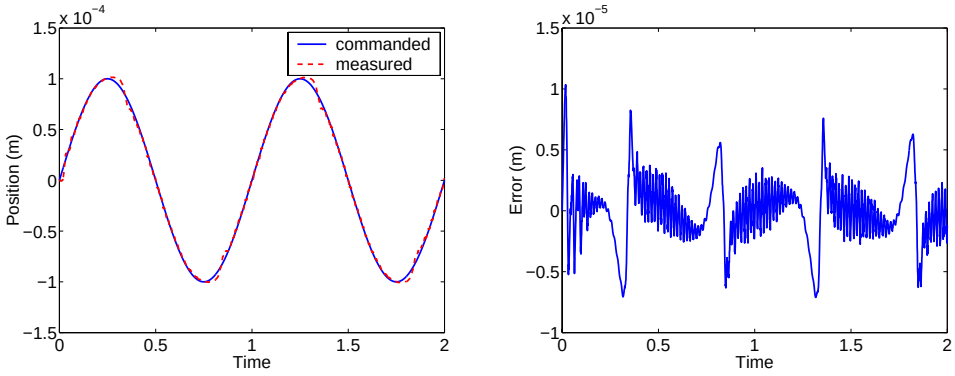

(a) (b)

Figure 6.11: H_2 optimal control results for a system employing a scaling factor in the design and simulation. The (a) tracking response, and (b) error.

induced by the hysteresis loop is evident in Figure 6.11a. The error, shown if Figure 6.11b, depicts a large error at the peaks of the reference signal invoked by the phase delay follow by a period where the controller is able to decrease the error.

Example 1d. The tracking performance of the H_2 optimal control design utilizing an inverse compensator based on the free energy model (2.37) and the corresponding weighting function W_d is illustrated in Figure 6.12. Figure 6.12a demonstrates the capability of the controller to track the reference signal and reject the noise and disturbance signals. A tracking error less than 2 microns is achieved after a short period and the noise signal and effects of the inverse compensation for the hysteresis are effectively attenuated, as illustrated in Figure 6.12b. The utilization of an inverse compensator based on the free energy hysteresis model is able to attenuate a sufficient amount of the hysteretic behavior as to allow the controller to attenuate the remaining disturbance.

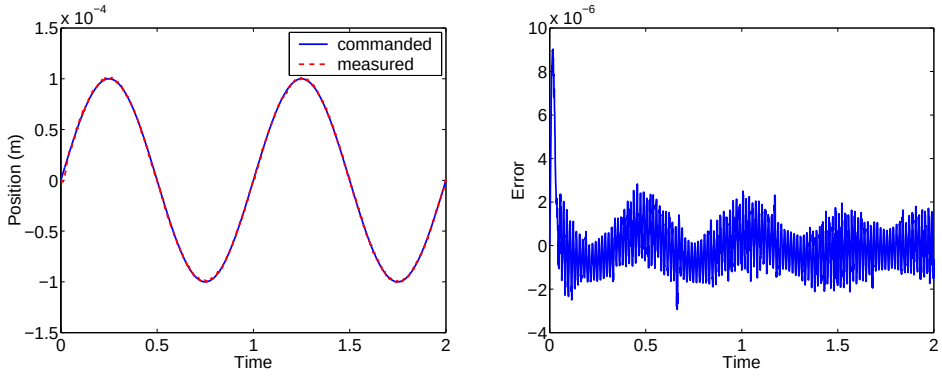

(a) (b)

Figure 6.12: H_2 optimal control results for a system employing an inverse compensator based on the free energy hysteresis model (2.37) in the design and simulation. The (a) tracking response, and (b) error.

To further verify the robustness of the H_2 optimal controller design for the last example, the closed loop transfer functions from the inputs to the tracking error $\overline{e} = r - y$ are examined. These functions are defined by

$$\overline{e} = r - (n + s + P\left[d + K\left[\overline{e}\right]\right])$$

$$\overline{e} = r - n - s - P[d] - PK[\overline{e}] \ . \tag{6.23}$$

From (6.23), we define the sensitivity function

$$S = (I + PK)^{-1} \tag{6.24}$$

and the disturbance sensitivity function

$$S_d = (I + PK)^{-1} P \ . \tag{6.25}$$

We can now represent the tracking error as

$$\overline{e} = S[r] - S[n] - S[s] - S_d[d] \ . \tag{6.26}$$

Since the sensitivity function is the map from the inputs r, n and s to the tracking error $\overline{e}$, we can analyze the robustness to certain frequency inputs by examining the frequency response of S. Figure 6.13a illustrates the frequency response of S. The magnitude of the response at a frequency of 1 Hz is -57 dB. This indicates good tracking performance for the reference signal which has a frequency of 1 Hz. Recall that the noise signal s has a frequency of 60 Hz. The sensitivity function in Figure 6.13a also exhibits a dip in the magnitude of the frequency response of S around 60 Hz with the magnitude being -0.8 dB at 60 Hz. Moreover, the magnitude of the response remains under 0 dB for larger frequencies because of the rejection of higher frequency noise imposed by the signal n. Figure 6.13b illustrates the magnitude of the frequency response of the disturbance sensitivity function S_d. Since S_d is the transfer function from d to $\overline{e}$, it should have small magnitude for frequencies less than 400 Hz which is evident in Figure 6.13b.

6.1.5 H_∞ Sub-optimal Control Design

In addition to the H_2-norm, another norm which can be utilized in the design of robust controllers is the H_∞-norm

$$\|T\|_\infty = \sup_{\omega \in \mathbb{R}} \overline{\sigma}[T(j\omega)] \tag{6.27}$$

where $\overline{\sigma}[T(j\omega)]$ denotes the maximal singular values of the closed loop map T. Employing the notation defined in (6.4), the design of a sub-optimal H_∞ controller which gives $\|T\|_\infty < \gamma$ yields two Hamiltonian matrices

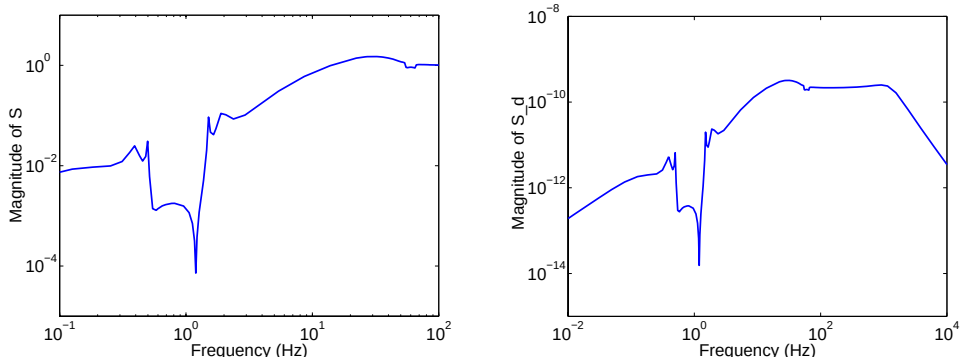

(a) (b)

Figure 6.13: (a) H_2 sensitivity function, and (b) H_2 disturbance sensitivity function.

$$H_\infty = \begin{bmatrix} A & \gamma^{-2}B_1B_1^* - B_2B_2^* \\ -C_1^*C_1 & -A^* \end{bmatrix} \tag{6.28}$$

and

$$J_\infty = \begin{bmatrix} A^* & \gamma^{-2}C_1^*C_1 - C_2^*C_2 \\ -B_1B_1^* & -A \end{bmatrix}. \tag{6.29}$$

These Hamiltonian matrices give rise to two Riccati equations

$$A^*X_\infty + X_\infty A + X_\infty \left(\gamma^{-2}B_1B_1^* - B_2B_2^*\right) X_\infty + C_1^*C_1 = 0 \tag{6.30}$$

and

$$AY_\infty + Y_\infty A^* + Y_\infty \left(\gamma^{-2}C_1^*C_1 - C_2^*C_2\right) Y_\infty + B_1B_1^* = 0\ . \tag{6.31}$$

The main difference between the Hamiltonian matrices given here and the Hamiltonian matrices corresponding to the H_2 formulation is that the (1,2) blocks of H_∞ and J_∞ are not sign definite. Therefore, a solution to the Ricatti equations can not be

guaranteed for all γ. Note that as γ approaches infinity the H_∞ Hamiltonians (6.28) and (6.29) become equivalent to the H_2 Hamiltonians (6.17) and (6.18).

The following theorem from [26] guarantees the existence of an H_∞ sub-optimal controller.

Theorem 6.2: There exists an admissible controller such that $\|T\|_\infty < \gamma$ iff:

1. $H_\infty \in$dom(Ric) and $X_\infty :=$Ric$(H_\infty) > 0$
2. $J_\infty \in$dom(Ric) and $Y_\infty :=$Ric$(J_\infty) > 0$
3. $\rho(X_\infty Y_\infty) < \gamma^2$.

The H_∞ sub-optimal controller is given by

$$K \equiv \left[\begin{array}{c|c} A_\infty & -Z_\infty L_\infty \\ \hline F_\infty & 0 \end{array}\right] \tag{6.32}$$

where

$$\begin{gathered} A_\infty \equiv A + \gamma^{-2} B_1 B_1^* X_\infty + B_2 F_\infty + Z_\infty L_\infty C_2 \\ F_\infty \equiv -B_2^* X_\infty \quad L_\infty \equiv -Y_\infty C_2^* \ . \end{gathered} \tag{6.33}$$

While the controller given in (6.32) is sub-optimal in that it gives a closed loop system with an H_∞-norm less than γ, the *Matlab* routine *hinfsyn* can be utilized to decrease γ until an assumption of Theorem 6.2 is violated. This gives a control design method which is close to optimal.

Now, the performance of the H_∞ control design is illustrated. We consider H_∞ sub-optimal control designs for a system without sensor noise and with sensor noise. Both cases are designed with consideration of an inverse compensator based on the

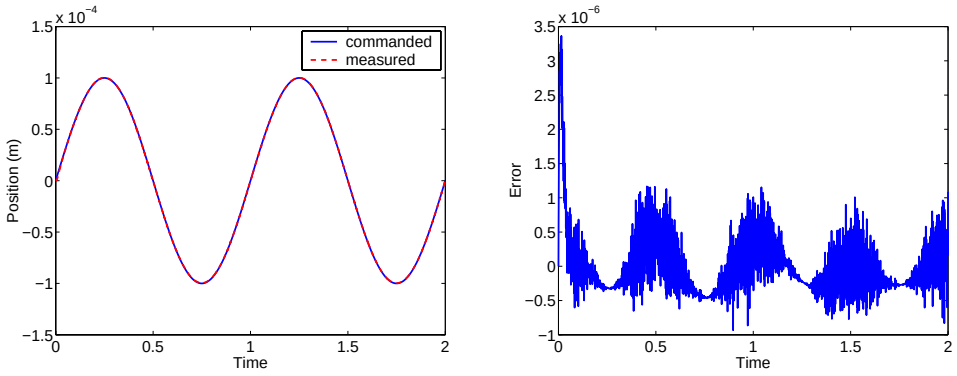

(a) (b)

Figure 6.14: H_∞ sub-optimal control results for a system employing an inverse compensator based on the free energy hysteresis model (2.37) with no sensor noise. The (a) tracking performance, and (b) tracking error.

free energy hysteresis model and the corresponding weight W_d as the previous examples demonstrated the superiority of this method. The parameters in the inverse compensator and free energy hysteresis model are the same as in the H_2 control examples.

Example 2a. The tracking performance in the absence of sensor noise is illustrated in Figure 6.14a. The ability of the H_∞ controller to effectively reject the disturbance d due to the hysteresis is evident from Figure 6.14b. The incorporation of an inverse compensator to an H_∞ sub-optimal control design has proved to effective in tracking a reference signal while rejecting the disturbance to the input of the plant caused by the hysteresis and inverse compensator.

Example 2b. The tracking performance in the presence of sensor noise is illustrated in Figure 6.15. Figure 6.15a illustrates the capability of the controller to track the

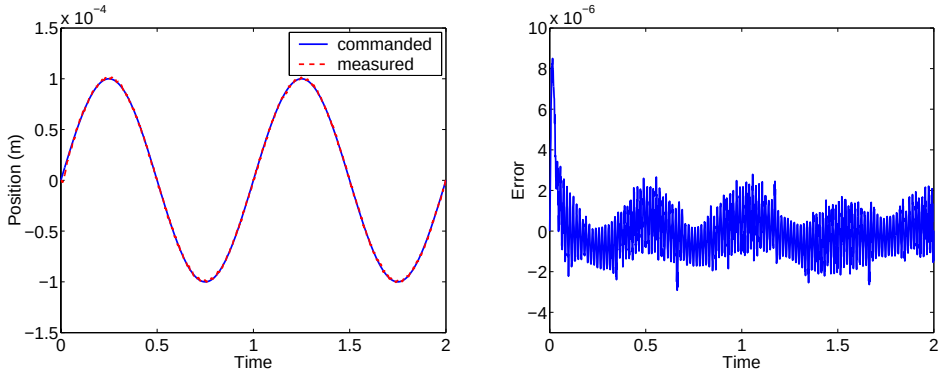

(a) (b)

Figure 6.15: H_∞ sub-optimal control results for a system employing an inverse compensator based on the free energy hysteresis model (2.37) with sensor noise. The (a) tracking performance, and (b) tracking error.

reference signal and reject the noise and disturbance signals. Again, a tracking error of approximately 2 microns is achieved after a short period, as illustrated in Figure 6.15b.

As was done with the H_2 optimal control formulation, the sensitivity and disturbance sensitivity functions with the H_∞ sub-optimal controller are examined to ensure robustness. Figure 6.16 depicts the magnitude of the frequency responses of the sensitivity and disturbance sensitivity functions for the H_∞ control design. As was seen with the H_2 controllers, the magnitude of S is small at the expected frequencies of the inputs r, n and s. The sensitivity function has magnitudes of -49 dB at 1 Hz and -0.7 dB at 60 Hz. Also note that the magnitude of S_d, illustrated in Figure 6.16b, is small for frequencies less than 400 Hz as imposed by W_d.

This section has outlined the formulation and numerical results of an H_2 optimal and H_∞ sub-optimal robust control design for a Terfenol-D transducer. It was shown that the inclusion of an inverse compensator based on the free energy hysteresis model

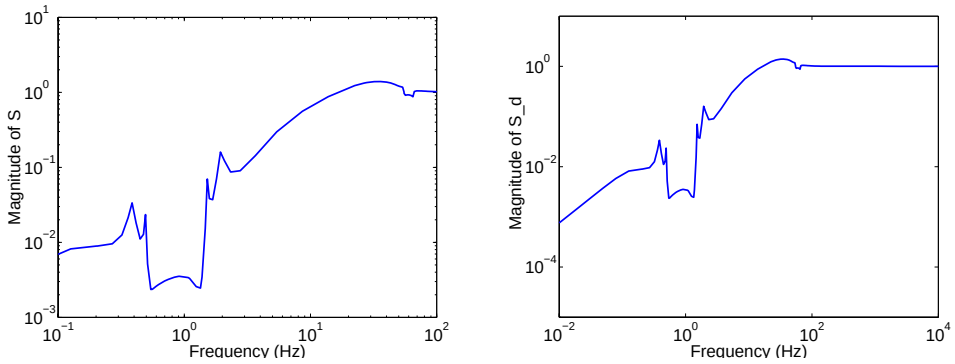

(a) (b)

Figure 6.16: (a) H_∞ sensitivity function, and (b) H_∞ disturbance sensitivity function.

in an H_2 or H_∞ control design provides accurate tracking while successfully attenuating sensor noise and a disturbance due to the inexact inverse filter. The same methodology can be used to include other disturbances to the system if necessary. Details were provided regarding the choice of weighting functions, or filters, since this step in the robust control formulation is crucial for achieving the balance between tracking requirements and disturbance rejection needed for a particular application.

6.2 Multiobjective Control

The last section demonstrated the design of controllers utilizing performance measures given by either H_2 or H_∞ norms. Performance with respect to one norm does not imply performance with respect to another, and applications often contain diverse uncertainties imposed on the system which necessitate multiple distinct quantification of the controller's performance. For example, the Terfenol-D transducer requires accurate tracking while rejecting sensor noise and the disturbance due to the inherent

hysteresis. Multiobjective controllers are capable of incorporating several measure of robustness into a single system. In the discussion that follows, we summarize a multiobjective formulation developed by Qi, Khammash, and Salapaka in [23, 24] and apply this control design to the Terfenol-D transducer. The previous section also demonstrated that the incorporation of an inverse compensator based on the free energy model (2.37) in the control design provides significant attenuation of the inherent hysteresis and allows the control to reject the error caused by the hysteresis. Therefore, the controllers designed in this section will employ this inverse compensation technique.

The multiobjective control design summarized here is implemented in discrete time. First, we define the λ transform which corresponds to the discrete version of the Laplace transform. The λ transform of a signal $x = (x(0), x(1), \ldots)$ is given as

$$\overline{x}(\lambda) = \sum_{k=0}^{\infty} x(k)\lambda^k \tag{6.34}$$

and the λ transform of a linear time-invariant system

$$G = \left[\begin{array}{c|c} A & B \\ \hline C & D \end{array}\right] \tag{6.35}$$

is defined by

$$\overline{G}(\lambda) = \lambda C \left(I - \lambda A\right)^{-1} B + D. \tag{6.36}$$

For simplicity, we denote the convolution of two system T and S as $T * S = TS$.

To define the multiobjective control problem, consider a general closed loop system which is represented by the linear fraction transformation depicted in Figure 6.17. Here G is a general discrete, linear, time-invariant plant and K is the controller to be synthesized. The map G from inputs to outputs may be partitioned as

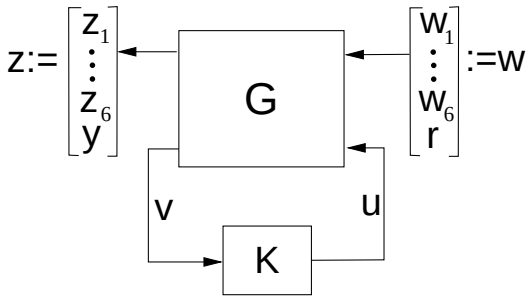

Figure 6.17: LFT for a general closed loop system.

$$G = \begin{bmatrix} G_{11} & G_{12} \\ G_{21} & G_{22} \end{bmatrix} \tag{6.37}$$

where G_{11} denotes the map from w to z, G_{12} denotes the map from w to v, G_{21} denotes the map from u to z and G_{22} denotes the map from u to v. We assume the system G is stabilizable from u and detectable from v therefore a controller stabilizes G if and only if it stabilizes G_{22} [6]. Hence, to parameterize all possible stabilizing controllers for G, we need only parameterize all possible stabilizing controllers for G_{22}. This can be accomplished utilizing a Youla parameterization.

The parameterization of all stabilizing controllers is only summarized here and a detailed discussion of this topic can be found in [6, 26]. A double-coprime factorization of G_{22} is defined as the set of maps M, N, $\tilde{M}$ and $\tilde{N}$ with $G_{22} = NM^{-1} = \tilde{M}^{-1}\tilde{N}$ satisfying

$$\begin{pmatrix} \tilde{X} & -\tilde{Y} \\ -\tilde{N} & \tilde{M} \end{pmatrix} \begin{pmatrix} M & Y \\ N & X \end{pmatrix} \tag{6.38}$$

for some stable maps X, Y, $\tilde{X}$, and $\tilde{Y}$. Now, [6] states that all the stabilizing controllers of G are represented by

$$K = (Y - MQ)(X - NQ)^{-1} \tag{6.39}$$

for some stable free parameter $Q \in l_1$. From (6.39) and the LFT representation depicted in Figure 6.17, it follows that all the achievable closed loop maps R from the inputs w to outputs z are represented by

$$R = H - UQ\ V \tag{6.40}$$

where

$$H = G_{11} + G_{12}Y\tilde{M}G_{21}, \quad U = G_{12}M, \quad V = \tilde{M}G_{21}. \tag{6.41}$$

To simplify notation, we denoting the map from input w_i to z_i, parameterized by Q, as $R^i(Q)$ for $i = 1, \ldots, 6$ and the map from r to y as $R^7(Q)$. Employing this notation, without loss of generality, we consider the case when r is a step input [24]. In order to include time domain constraints in the multiobjective control formulation, the time response of the closed loop system due to the input r is specified as $y = R^7(Q) * r = A_t R^7(Q)$ where

$$A_t = \begin{bmatrix} 1 & 0 & 0 & \cdots \\ 1 & 1 & 0 & \cdots \\ \vdots & \vdots & \ddots & \ddots \end{bmatrix}. \tag{6.42}$$

The general multiobjective control problem for the system depicted in the linear fractional transformation in Figure 6.17 is now defined as

$$\mu = \inf_{Q \in l_1} c_1 \|R^1(Q)\|_1 + c_2 \|R^2(Q)\|_2^2 + c_3 \|\overline{R}^3(Q)\|_{H_\infty}$$

subject to

$$\begin{aligned} &\|R^4(Q)\|_1 \leq c_4 \\ &\|R^5(Q)\|_2^2 \leq c_5 \\ &\|\overline{R}^6(Q)\|_{H_\infty} \leq c_6 \\ &a_t(k) \leq \left[A_t R^7(Q)\right](k) \leq b_t(k), \text{ for all } k \end{aligned} \tag{6.43}$$

where $c_i > 0,\ i = 1, \ldots, 6$ and a_t and b_t are specified infinite sequences [24].

In the general case, (6.43) is difficult to solve so, to facilitate the solution, an auxiliary problem is defined in [24] given by

$$\nu = \inf_{Q \in l_1} c_1 \|R^1(Q)\|_1 + c_2 \|R^2(Q)\|_2^2 + c_3 \|\overline{R}^3(Q)\|_{H_\infty}$$

subject to

$$\begin{aligned} &\|Q\|_1 \leq \gamma \\ &\|R^4(Q)\|_1 \leq c_4 \\ &\|R^5(Q)\|_2^2 \leq c_5 \\ &\|\overline{R}^6(Q)\|_{H_\infty} \leq c_6 \\ &a_t(k) \leq \left[A_t R^7(Q)\right](k) \leq b_t(k), \text{ for all } k. \end{aligned} \tag{6.44}$$

This auxiliary problem improves the numerical solution of the multiobjective problem by allowing a regularization as detailed in [15]. Also, it is possible that the problem (6.43) does not admit a solution with a bounded one norm on Q. In such a case it would be reasonable to impose a bound on $\|Q\|_1$ although, typically, this bound is redundant.

To numerically implement a multiobjective control design, a sequence of finite dimensional convex optimization problems are derived. The objective values of this sequence converge to the objective value of the infinite dimensional problem (6.44) monotonically from below given that for all k, $a_t(k) < b_t(k)$ and that there exists N_1 and N_2 so that $a_t(k) = a_t(N_1)$, for all $k \geq N_1$ and $b_t(k) = b_t(N_2)$, for all $k \geq N_2$. The finite dimensional system is specified in [24] by

$$\nu_n = \inf_{Q \in l_1} c_1 \|P_n(R^1(Q))\|_1 + c_2 \|P_n(R^2(Q))\|_2^2 + c_3 \|T_{3,n}(Q)\|$$

subject to

$$\begin{aligned} &\|Q\|_1 \leq \gamma \\ &\|P_n(R^4(Q))\|_1 \leq c_4 \\ &\|P_n(R^5(Q))\|_2^2 \leq c_5 \\ &\|T_{6,n}(Q)\| \leq c_6 \\ &a_t(k) \leq \left[A_t R^7(Q)\right](k) \leq b_t(k), \quad k = 0, \ldots, n. \end{aligned} \tag{6.45}$$

Here, P_n denotes the truncation operator defined as

$$P_n(x) = (x(0), x(1), \ldots, x(n), 0, 0, \ldots), \tag{6.46}$$

and

$$T_{i,n}(Q) = \begin{bmatrix} R^i(0) & 0 & \cdots & 0 \\ \vdots & \ddots & \ddots & 0 \\ R^i(n) & \cdots & \cdots & R^i(0) \end{bmatrix}, \quad i = 3, 6. \tag{6.47}$$

A theorem providing the existence of a solution to (6.45) and the monotonic convergence of ν_n to ν from below as $n \to \infty$ is proved in [15].

An upper bound sequence of finite dimensional systems is also defined in [24] and is given by

$$\nu^n = \inf_{Q \in l_1} c_1 \|R^1(Q)\|_1 + c_2 \|R^2(Q)\|_2^2 + c_3 \|\overline{R}^3(Q)\|_{H_\infty}$$

subject to

$$\begin{aligned} &\|Q\|_1 \leq \gamma \\ &\|R^4(Q)\|_1 \leq c_4 \\ &\|R^5(Q)\|_2^2 \leq c_5 \\ &\|\overline{R}^6(Q)\|_{H_\infty} \leq c_6 a_t(k) \leq \left[A_t R^7(Q)\right](k) \leq b_t(k), \text{ for all } k \\ &Q(k) = 0 \text{ if } k > n. \end{aligned} \tag{6.48}$$

A second theorem provided in [15] ensures the existence of a solution to (6.48) and the monotonic convergence of ν^n to ν from above as $n \to \infty$. Note that in the lower (6.45) and upper (6.48) bound problems, only the parameters $Q(0), \ldots, Q(n)$ occur in the optimization. This yields solvable finite dimension optimization problems.

6.2.1 System Representation

Now that the general multiobjective problem and the finite dimension upper and lower bound problems have been formulated, we apply these formulations to the control of the Terfenol-D actuator. Since we are working in discrete space, a zero-order hold discretization of the model (3.18) is employed for the plant which is denoted P. Figure 6.18 illustrates the system to be controlled which is similar to the system in the previous section seen in Figure (6.3).

The discrete signal to be tracked is denoted r and y is the position of the tip of the Terfenol-D rod. Again, n is the sensor noise signal, d is the disturbance created by the inverse compensator and the error is denoted e. The weighting functions W_n and W_d are chosen based on *a priori* knowledge of the signals n and d. We are concerned

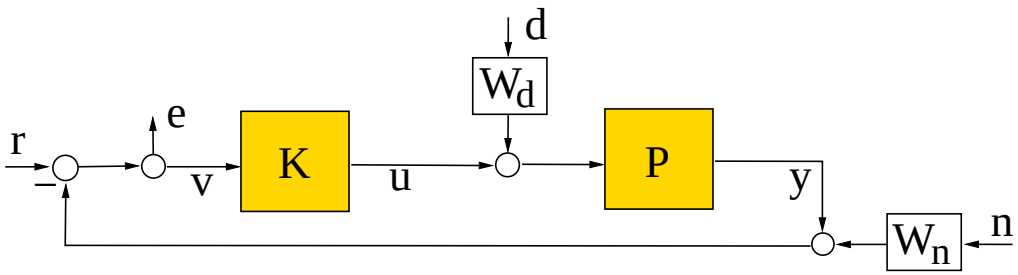

Figure 6.18: System diagram for multiple objective system.

with the effect of the input signals on the error e. Therefore, e is the only exogenous output in our system.

Several differences to note between the system given in Figure 6.18 and the system in Figure 6.3 include the omission of the signals s and $\widehat{u}$ and the weighting functions W_r and W_e. The signal s is left out or combined with n for simplicity. The weighted output $\widehat{u}$ of the controller K is not necessary for the multiobjective control synthesis as it was for the H_2 and H_∞ control designs. In the previous section, the weighting function on the error W_e was taken as an adjusted integrator to improve the tracking performance. With a multiobjective control design, high performance controls can be achieved without such a weight.

To formulate the Terfenol-D problem in the framework of the general problem, we denote the λ transform of r as $\overline{W}_r$ and define the signal $r_1 = (1, 0, \ldots)$. From these definitions, note that $\overline{r} = \overline{W}_r \overline{r_1}$, or equivalently, $r = W_r * r_1$. The reference signal r can be replaced with $W_r * r_1$, as seen in Figure 6.19, to ensure accurate tracking. In the numerical simulations, the reference signal to be tracked is taken as a sinusoidal signal $r(k) = a \cdot \sin(2\pi\omega T_s k)$ where ω is the frequency and T_s is the sampling frequency. This implies that

$$\overline{W}_r(\lambda) = \frac{\sin(\omega T_s)\lambda}{\lambda^2 - 2\cos(\omega T_s)\lambda + 1}. \tag{6.49}$$

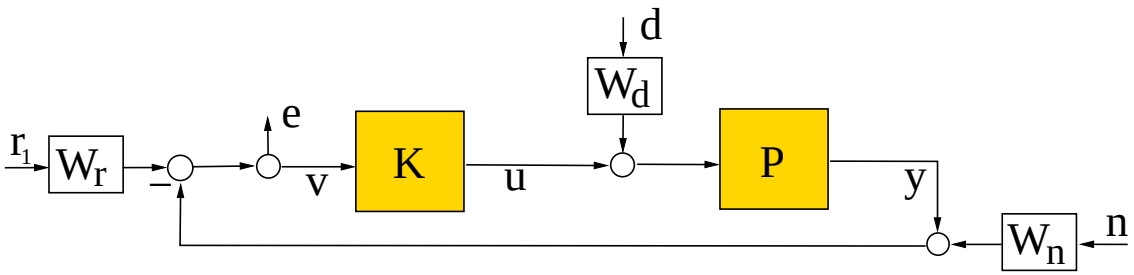

Figure 6.19: Equivalent system diagram for multiple objective system.

In the simulations we apply a 60 Hz sensor noise signal n. Therefore, W_n is specified as a sixth-order discrete Butterworth filter with a pass-band of 10 Hz centered at 60 Hz. For the system design, we consider the employment of the inverse of the free energy hysteresis model as the inverse compensator and chose W_d accordingly. Since the disturbance d has large spectrum values for frequencies less than 350 Hz, as seen in Figure 6.8, W_d is taken as a fourth-order low-pass discrete Butterworth filter with a cut-off frequency of 400 Hz.

The maps from the inputs d, n, and $\tilde{r}$ to the outputs e, and v for the Terfenol-D transducer system are specified by

$$\begin{aligned} v &= W_r * r_1 - (W_n * n + P[W_d * d + u]) \\ &= W_r * r_1 - W_n * n - PW_d * d - P * u \\ e &= v. \end{aligned} \tag{6.50}$$

Next, the closed loop system is represented by the LFT shown in Figure 6.20 with the matrix G given as

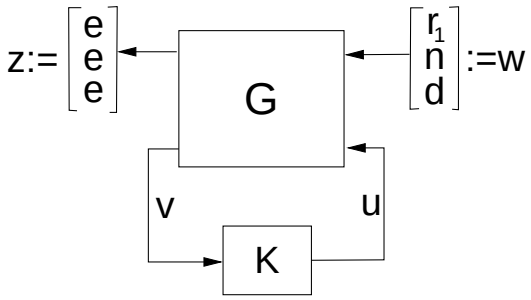

Figure 6.20: LFT for Terfenol-D system.

$$G = \begin{bmatrix} W_r & -W_n & -PW_d & -P \\ W_r & -W_n & -PW_d & -P \\ W_r & -W_n & -PW_d & -P \\ W_r & -W_n & -PW_d & -P \end{bmatrix} = \begin{bmatrix} G_{11} & G_{12} \\ G_{21} & G_{22} \end{bmatrix}, \tag{6.51}$$

so that

$$\begin{aligned} G_{11} &= \begin{bmatrix} W_r & -W_n & -PW_d \\ W_r & -W_n & -PW_d \\ W_r & -W_n & -PW_d \end{bmatrix}, \quad G_{12} = \begin{bmatrix} -P \\ -P \end{bmatrix}, \\ G_{21} &= \begin{bmatrix} W_r & -W_n & -PW_d \end{bmatrix}, \qquad G_{22} = [-P]. \end{aligned} \tag{6.52}$$

Recalling that all achievable closed loop maps are represented as $R = H - UQV$ with H, U and V given in (6.41), we specify

$$\begin{aligned} R^1(Q) &= W_r + MPQ\tilde{M}W_r \\ R^2(Q) &= -W_n - MPQ\tilde{M}W_n \\ R^3(Q) &= -PW_d - MPQ\tilde{M}PW_d \end{aligned} \tag{6.53}$$

where $\tilde{M}$, $\tilde{N}$, N, and M are double-coprime factors of $G_{22} = -P$. Since P is stable, we can take $Y = \tilde{Y} = 0$ in the coprime factorization of $-P$. The λ transform of P is

a rational function; therefore, we take

$$-\overline{P}(\lambda) = \frac{\overline{N}(\lambda)}{\overline{M}(\lambda)}. \tag{6.54}$$

Furthermore, we define $\tilde{N} = N$, $\tilde{M} = M$, $\tilde{X} = M^{-1}$ and $X = \tilde{M}^{-1}$ to satisfy the double coprime factorization.

The following examples will demonstrate several formulations of multiobjective control problems associated with the Terfenol-D transducer.

6.2.2 Mixed l_1 and H_2 Control

Initially, we consider a multiobjective control design for the Terfenol-D transducer depicted in Figure 1.3 employing an l_1 constraint on the tracking performance and an objective function based on the H_2 measure of the sensor noise rejection. The l_1 norm is chosen to quantify the tracking performance since it is a measure of the ratio of the worst case maximum amplitude of the output to the worst case maximum amplitude of the input. The H_2 norm is chosen to measure the map from the noise to the error because it quantifies the worst case maximum amplitude of the output in the presence of bounded energy. For this example the hysteresis is ignored in both the controller synthesis and the numerical simulation in order to demonstrate the capabilities of a mixed l_1/H_2 control formulation.

This problem is formulated as the auxiliary multiobjective problem

$$\nu = \inf_{Q \in l_1} \|R^2(Q)\|_2^2$$

subject to

$$\begin{aligned} &\|Q\|_1 \leq \gamma \\ &\|R^1(Q)\|_1 \leq c_1 \end{aligned} \tag{6.55}$$

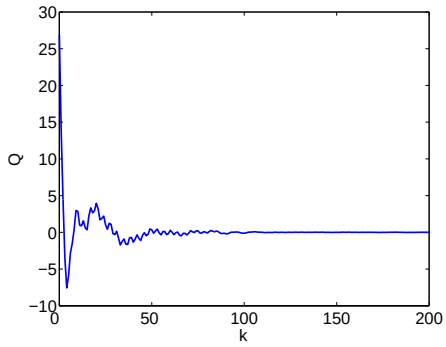

Figure 6.21: Optimal Q impulse response for multiobjective control design with an H_2 measure of sensor noise rejection as the objective function and an l_1 constraint on the tracking error.

where R^2 and R^1 are given in (6.53). To numerically implement this control design, the lower bound of the problem (6.55) is employed. This lower bound problem is given as

$$\nu = \inf_{Q \in l_1} \|P_n(R^2(Q))\|_2^2$$

subject to

$$\begin{aligned} &\|Q\|_1 \leq \gamma \\ &\|P_n(R^1(Q))\|_1 \leq c_1. \end{aligned} \tag{6.56}$$

It should be noted that in the computation of the solution to (6.56), a gain was applied to the plant P. This was done to aid the optimization process by causing a change in the free parameter Q to invoke a more noticeable change in the closed loop system. In the closed loop simulations, the gain was removed.

A sensor noise signal with a frequency of 60 Hz and an amplitude of 1×10^{-5} m, which is approximately 10% of the signal, was applied to the system and the scalar gains are taken to be $\gamma = 1 \times 10^5$ and $c_1 = 1$. The l_1 norm on Q is redundant for this example but aids the optimization as previously stated.

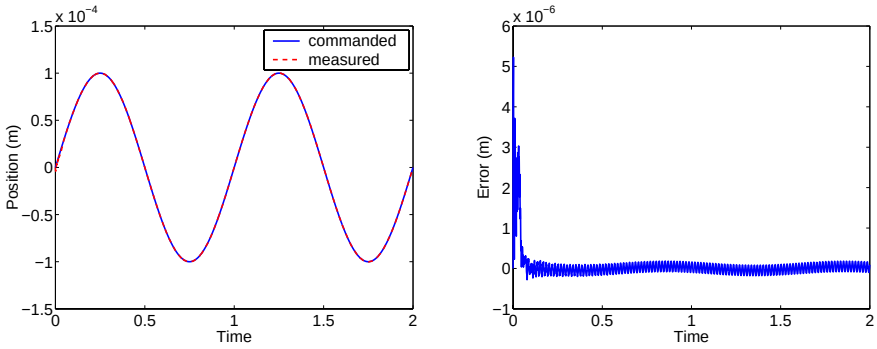

(a) (b)

Figure 6.22: (a) Tracking, and (b) error for multiobjective control design with an H_2 measure of sensor noise rejection as the objective function and an l_1 constraint on the tracking error.

Figure 6.21 illustrates the free parameter Q which solved the problem (6.56). The parameter Q was optimized over the first 200 steps, i.e., $n = 200$, and a state space representation of Q was constructed from the impulse response of Q assuming $Q(k) = 0$ for $k > 200$. This system was employed over the entire time span. The H_2 norm of $P_n(R^2(Q))$ for the optimal Q was found to be 2.3×10^{-1}.

In Figure 6.22, the tracking and error of the system are depicted. Figure 6.22b shows the capability of the multiobjective controller to reject the sensor noise while maintaining accurate tracking. Comparing the error shown in Figure 6.22b with the error for the H_2 formulation for a system with sensor noise and no hysteresis shown in Figure 6.9b, it is clear that the multiobjective control provides better sensor noise attenuation than the H_2 formulation. This example is evidence of the benefits of employing a multiobjective control approach to measure the performance of different aspects of the system utilizing different norms.

6.2.3 Mixed l_1 and H_∞ Control

Here, we consider a multiobjective control design for the Terfenol-D transducer employing an l_1 constraint on the tracking performance and an objective function consisting of an H_∞ measure of the rejection of the error caused by the inherent hysteresis. In order to demonstrate the capabilities of a mixed l_1/H_∞ control formulation, no sensor noise is considered. The formulation of the auxiliary multiobjective problem, in this case, is given as

$$\nu = \inf_{Q \in l_1} \|\overline{R}^3(Q)\|_{H_\infty}$$

subject to

$$\begin{aligned} &\|Q\|_1 \leq \gamma \\ &\|R^1(Q)\|_1 \leq c_1 \end{aligned} \tag{6.57}$$

where, again, R^3 and R^1 are given in (6.53). The lower bound of the problem (6.57) which is numerically implemented is given by

$$\nu = \inf_{Q \in l_1} \quad \|T_{3,n}(Q))\|$$

subject to

$$\begin{aligned} &\|Q\|_1 \leq \gamma \\ &\|P_n(R^1(Q))\|_1 \leq c_1. \end{aligned} \tag{6.58}$$

The scalar gains were taken to be $\gamma = 1 \times 10^5$ and $c_1 = 0.6$. Again, the l_1 norm on Q becomes redundant.

The inverse compensator was computed using 4 quadrature points, 20 divisions for the coercive field, 40 divisions for the effective field and a step size of $\Delta H = 1$. These parameters allow the possibility of real time implementation of the multiple objective control system. The parameters utilized for the free energy hysteresis model (2.37) are given in Table 2.3.

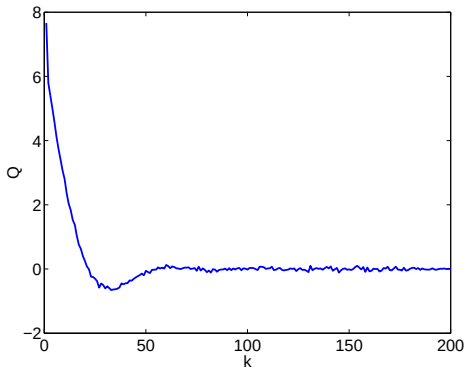

Figure 6.23: Optimal Q impulse response for multiobjective control design with an H_∞ measure of the hysteretic disturbance rejection as the objective function and an l_1 constraint on the tracking error.

The free parameter Q which solved the problem (6.58) is illustrated in Figure 6.23. The parameter Q was optimized over the first 200 steps, i.e. $n = 200$, and this system was employed over the entire time span. The H_∞ norm of $T_{3,n}(Q))$ for the optimal Q was found to be 2.2×10^{-2}.

The tracking and error are shown in Figure 6.24a and Figure 6.24b, respectively. These figures demonstrate the capability of the multiobjective controller to reject the disturbance due to the inverse filter and hysteresis while maintaining accurate tracking. The level of error shown in Figure 6.24b is significantly less than the error resulting from the H_∞ sub-optimal control design with no sensor noise depicted in Figure 6.14b. These results again illustrate the benefit of utilizing different norms to measure performance in the multiobjective control design.

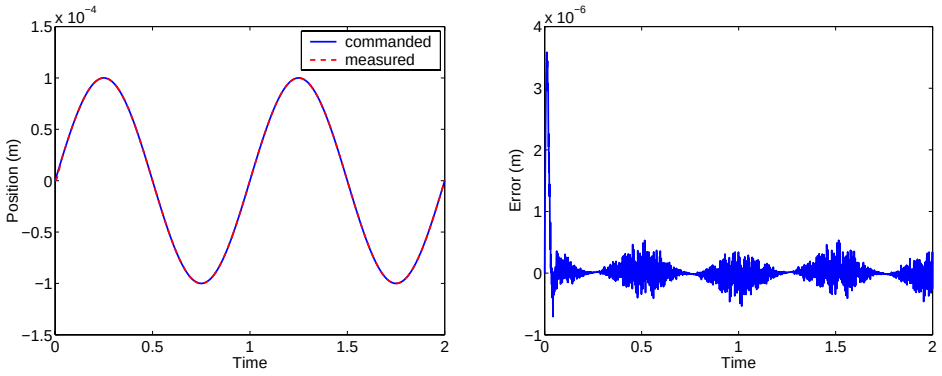

(a) (b)

Figure 6.24: (a) Tracking, and (b) error for multiobjective control design with an H_∞ measure of hysteretic disturbance rejection as the objective function and an l_1 constraint on the tracking error.

6.2.4 Mixed l_1, H_2 and H_∞ Control

Finally, we consider a multiobjective control design with an l_1 constraint on the tracking performance, an H_∞ constraint on the rejection of the error caused by the hysteresis and an objective function of the H_2 measure of sensor noise rejection. This problem is formulated as the following auxiliary multiobjective problem.

$$\nu = \inf_{Q \in l_1} \|R^2(Q)\|_2^2$$

subject to

$$\begin{aligned} &\|Q\|_1 \leq \gamma \\ &\|R^1(Q)\|_1 \leq c_1 \\ &\|\overline{R}^3(Q)\|_{H_\infty} \leq c_2 \end{aligned} \tag{6.59}$$

where, again, R^3 and R^1 are given in (6.53). The lower bound of the problem (6.59)

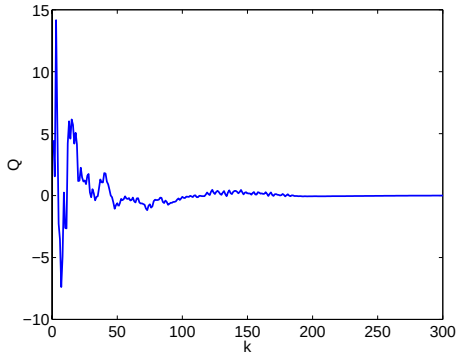

Figure 6.25: Optimal Q impulse response for multiobjective control design with an H_2 measure of the noise rejection as the objective function, an H_∞ constraint on the hysteretic disturbance rejection and an l_1 constraint on the tracking error.

that is numerically implemented is given by

$$\nu = \inf_{Q \in l_1} \|P_n(R^2(Q))\|_2^2$$

subject to

$$\begin{aligned} &\|Q\|_1 \leq \gamma \\ &\|P_n(R^1(Q))\|_1 \leq c_1 \\ &\|T_{3,n}(Q)\| \leq c_2. \end{aligned} \tag{6.60}$$

The scalar gains were taken to be $\gamma = 1 \times 10^5$, $c_1 = 1$ and $c_2 = 0.04$. Again, the l_1 norm on Q becomes redundant. The inverse compensator was computed using 4 quadrature points and 20 divisions for the coercive field, 40 divisions for the effective field and a step size of $\Delta H = 1$.

The free parameter Q which solved the problem (6.60) is illustrated in Figure 6.25. Again, the parameter Q was optimized over the first 300 steps, i.e. $n = 300$, and this system was employed over the entire time span. Note that more steps are included in the optimization for this example than in the previous examples. The solution of the

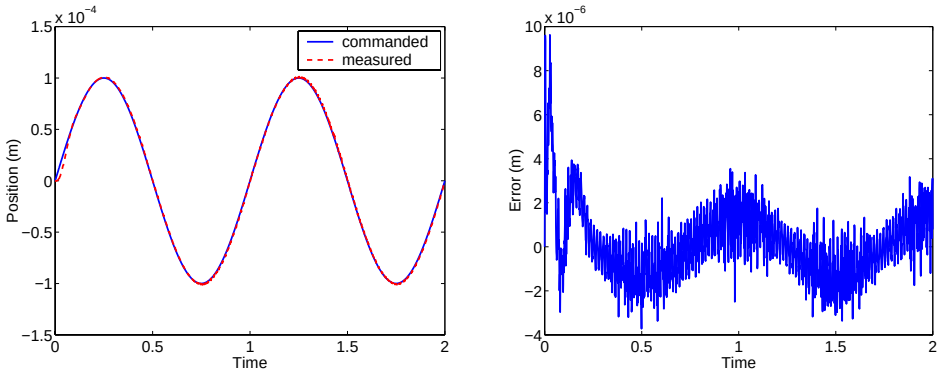

(a) (b)

Figure 6.26: (a) Tracking, and (b) error for multiobjective control design with an H_2 measure of sensor noise rejection as the objective function, an H_∞ constraint on the hysteretic disturbance rejection and an l_1 constraint on the tracking error.

lower bound problem (6.60) converges to the solution of the auxiliary problem (6.59) as $n \to \infty$ and more step were needed in this example to provide good results.

The tracking and error are shown in Figure 6.26a and Figure 6.26b, respectively. These figures demonstrate the ability of the multiobjective controller to design a controller which incorporates different performance measures for the different control objectives. The level of performance is comparable to the H_2 optimal and H_∞ sub-optimal control designs implemented in the previous section.

6.3 Concluding Remarks

This chapter presented robust control designs which incorporated external disturbances to the system due to unattenuated hysteretic behavior and sensor noise in the control design. In the first section, H_2 and H_∞ norms were employed to measure the robustness of the system to disturbances due to unattenuated hysteresis and sensor

noise. It was shown that the controllers designed under the consideration of the utilization of an inverse compensator based on the free energy model of hysteresis (2.37) were able to achieve accurate tracking while rejecting the disturbances due to sensor noise and the inherent hysteresis.

The last section demonstrated that a multiobjective control design incorporating the inverse compensator can provide high levels of performance for the magnetostrictive transducer. The multiobjective control synthesis is able to utilize different norm measures of robustness with respect to the different disturbances. This allows the most relevant measure to be applied to each control criteria. A disadvantage of the multiobjective control design is the computational effort required to obtain the optimal controller. For the last example, an optimization problem with 300 degrees of freedom was solved. To improve the controller's performance, the number of degrees of freedom must be increased.

Chapter 7

Conclusion

This dissertation has focused on the modeling and control of a magnetostrictive actuator. The techniques for the control of the transducer include the employment of an inverse compensator to attenuate the effects of the inherent hysteresis in the material. An emphasis was placed on the development of models and inverse compensators which are sufficiently simple to facilitate their incorporation into control methods which allow the possibility of real-time implementation.

Three hysteresis models are summarized in Chapter 2 and inverse compensators based on these hysteresis models are developed. The domain wall and free energy hysteresis models utilize energy principles to quantify the relationship between the applied magnetic field and the magnetization in a magnetostrictive material while the straight line Preisach hysteresis model is not derived from physical properties. The free energy hysteresis model provides the most accurate description of the hysteresis inherent in magnetostrictive materials including biased minor loop behavior. This model can be implemented algebraically; thus is ideal for control design.

Once the hysteretic behavior in the magnetostrictive material has been quantified, the strains, forces and displacements in the actuator are specified in Chapter 3. The magnetostrictive effects are included in the quantification of the strains in the

Terfenol-D rod as is a term incorporating Kelvin-Voight damping. The PDE giving the displacement of the rod at any time can be numerically implemented by applying a Galerkin finite element approximation method. If certain flux shaping methods are utilized, the magnetostrictive transducer can be modeled as an ODE elastic equation with a nonlinear hysteretic input. For transducer where an ODE model is insufficient, the techniques in Chapters 4-6 could be applied to the Galerkin finite element approximation.

Chapter 4 provides adaptive nonlinear parameter estimation algorithms. These methods are able to determine nonlinearly occurring parameters in the transducer models during the actuation process. This may be preferable to off-line parameter estimation methods such as a least squares fit to data since the parameters can be updated on-line. To effectively employ inverse compensation techniques, the parameters in the model must be accurately estimated. The hysteretic behavior of the Terfenol-D is effected by changes in operating conditions such as temperature. Thus, it is advantageous to develop a method of re-identifying slowly varying nonlinear material parameters without interrupting the actuation.

The difficulties in controlling a magnetostrictive actuator under realistic operating conditions are illustrated by applying several preliminary control designs to the Terfenol-D transducer in Chapter 5. First, a linear adaptive control techniques is applied to the transducer. This method utilizes the Preisach model and corresponding approximate inverse and provides the capability of tracking a reference response while tuning the parameters in the approximate inverse to the actual parameters. The Preisach hysteresis model is required since the control error must be quantified by a linear combination of the parameter estimates. The inability of the linear adaptive control technique to incorporate more accurate hysteresis models limits its utility for controlling general nonlinear smart structures.

The attributes and limitations of inverse compensation techniques combined with PID and LQR control designs are also summarized in Chapter 5. While the employment of inverse compensation is able to reduce the effects of the inherent hysteresis, these control methods are not designed to accommodate the remaining error in the system nor can they attenuate the presence of sensor noise.

Chapter 6 describes control designs which include the presence of external disturbances to the system such as the error caused by the hysteretic material and sensor noise. Controllers designed to minimize the H_2 and H_∞ norms of the closed-loop system are designed and the performance is illustrated. A multiobjective control technique is also discussed in this chapter. This technique has the capability of measuring the robustness with respect to different disturbance with different norm to reflect the performance criteria.

The simulation results presented in this dissertation illustrate that the incorporation of an inverse filter based on the free energy hysteresis model (2.37) provides significant attenuation of the inherent hysteresis in the Terfenol-D actuator. It is also noted that control designs which consider the error due to hysteresis and the presence of sensor noise in the design system provide the highest level of performance.

The techniques for transducer modeling, nonlinear parameter estimation and robust control were developed in the context of a magnetostrictive transducer but they are sufficiently general to be extended to many smart systems. In [21], it is shown that analogous free energy hysteresis formulations can be developed for ferroelectric and, in certain operating regimes, ferroelastic materials. These hysteresis models can be incorporated into a model of the full transducer and the robust control designs in Chapter 6 can be employed. If the transducer can not be accurately model by an ODE, the finite element approximation of the PDE model can be utilized in the control design. This will increase the number of states in the system and, for H_2 and H_∞ control formulations, the controller but these methods can still be applied.

As multiobjective control design employs the impulse response of the free parameter Q, the number of states in the transducer will not affect the number of states in the resulting controller.

The investigation of robust control techniques presented in this dissertation is by no means exhaustive. In addition to external disturbances, model uncertainty can be incorporated into the control design system. Techniques employing the structural singular value can be employed to quantifying the robustness of a system to unknown dynamics. Controllers can then be designed to accommodate a level of uncertainty in the plant model. This may be an alternative method for accommodating the disturbance caused by the inverse compensator and inherent hysteresis in smart materials. A detailed description of model uncertainty methods are provided in [26].

Another area of interest is the experimental implementation of the control designs discussed in Chapter 6. The performance of the inverse compensator and the robustness of the control designs can be validated through simulation but the ultimate goal is the implementation of these method in physical experiments.

Appendix A

Proof of Theorem 4.1

The proof of Theorem 4.1 is outlined in [14]. Here we present a detailed proof of the theorem. To prove that (4.18) is the solution of (4.8) we must first introduce a lemma.

Lemma 1: For any bounded function $g(y)$, if $\widehat{y} \in Y$, where Y is a bounded convex set, then

1) $0 \leq \min\limits_{x\in\mathbb{R}} \max\limits_{y\in Y} \ (g(y) - g(\widehat{y}) + x(\widehat{y} - y)) < \infty$

2) $\min\limits_{x\in\mathbb{R}} \max\limits_{y\in Y} \ (g(y) - g(\widehat{y}) + x(\widehat{y} - y)) = \min\limits_{x,c\in\mathbb{R}} \ (x\widehat{y} + c)$ subject to (s.t.)
$xy + c \geq g - \widehat{g}$ for all $y \in Y$.

Proof of Lemma 1:

The proof presented here is a detailed version of the proof given in [14].

1) For any x and bounded $g(y)$, if $\widehat{y} \in Y$ then

$$0 \leq g - \widehat{g} + x(\widehat{y} - y) < \infty \text{ for some } y \in Y. \tag{A.1}$$

For example, $y = \widehat{y}$ will satisfy (A.1). Therefore,

$$\begin{aligned} 0 &\leq \max_{y\in Y}\left(g(y)-g(\widehat{y})+x(\widehat{y}-y)\right)<\infty \\ 0 &\leq \min_{x\in\mathbb{R}}\max_{y\in Y}\left(g(y)-g(\widehat{y})+x(\widehat{y}-y)\right)<\infty. \end{aligned}$$

2) For any x satisfying $xy+c\geq g-\widehat{g}$,

$$g(y)-g(\widehat{y})+x(\widehat{y}-y)\leq x\widehat{y}+c.$$

Hence, for any x

$$\max_{y\in Y}\ \left(g(y)-g(\widehat{y})+x(\widehat{y}-y)\right)\leq x\widehat{y}+c$$

and

$$\min_{x\in\mathbb{R}}\max_{y\in Y}\ \left(g(y)-g(\widehat{y})+x(\widehat{y}-y)\right)\leq \min_{x\in\mathbb{R}}\ \left(x\widehat{y}+c\right). \quad \square$$

Employing this lemma, Theorem 4.1 can be proved. We will prove the case where $\tilde{y}_\epsilon>0$. The proof for $\tilde{y}_\epsilon<0$ is analogous.

Proof of Theorem 4.1:
Consider $\theta\in\theta_c$; since f is concave on θ_c, $\underline{F}(\theta)=f-\widehat{f}$ is concave on θ_c. If $\theta\in\tilde{\theta}_c$, $\underline{F}(\theta)$ is linear and hence concave. $\underline{F}(\theta)$ is continuous on Θ since $f^i-\widehat{f}=\phi^{ij}\theta^i+c^{ij}$ for any θ^i which is an endpoint of an interval of θ_c. In addition to $\underline{F}(\theta)$ being a continuous concave function on Θ, if $\theta\in\theta^{ij}$

$$\underline{F}(\theta)=\lambda f^j+(1-\lambda)f^i-\widehat{f}\quad\text{where}\quad\lambda=\frac{\theta-\theta^i}{\theta^j-\theta^i}.$$

As $\theta\in\theta^{ij}$, $0\leq\lambda<1$. Since f is not concave on every θ^{ij}, we have

$$f(\theta)\leq\lambda f^j+(1-\lambda)f^i\text{ for all }\theta\in\theta^{ij} \tag{A.2}$$

and therefore $\underline{F}(\theta) \geq f - \widehat{f}$ for all $\theta \in \tilde{\theta}_c$.

Consider $\widehat{\theta} \in \theta_c$. By definition we have

$$\nabla f_{\widehat{\theta}}(\theta - \widehat{\theta}) \geq f - \widehat{f} \text{ for all } \theta \in \Theta. \tag{A.3}$$

Defining the following

$$\theta = y, \quad \widehat{\theta} = \widehat{y}, \quad \nabla f_{\widehat{\theta}} = x, \quad -\nabla f_{\widehat{\theta}}\, \widehat{\theta} = c, \quad f = g, \quad \widehat{f} = \widehat{g}, \quad \Theta = Y, \tag{A.4}$$

and employing Lemma 1, we can rewrite (A.3) as

$$xy + c \geq g - \widehat{g} \text{ for all } y \in Y.$$

Since, by the definitions in (A.4), $x\widehat{y} + c = 0$ we have

$$\min_{x,c \in \mathbb{R}} \; (x\widehat{y} + c) = 0.$$

By the equivalence of the min/max problem given by Lemma 1 and the fact that, since $\widehat{\theta} \in \theta_c$, $\underline{F}(\widehat{\theta}) = 0$, problem (4.8) has a solution

$$a^* = \underline{F}(\widehat{\theta}) = 0 \qquad\qquad \phi^* = \left.\frac{\partial f}{\partial \theta}\right|_{\widehat{\theta}}.$$

Now we must consider $\widehat{\theta} \in \tilde{\theta}_c$. Let $\widehat{\theta} \in \theta^{ij}$ for some i, j. From part 2 of Lemma 1 we have that

$$\begin{aligned} \min_{\phi \in \mathbb{R}} \max_{\theta \in \Theta} \; J(\phi, \theta) &= \min_{\phi, c \in \mathbb{R}} \; \phi\widehat{\theta} + c \quad \text{s.t.} \quad f - \widehat{f} \leq \phi\theta + c \text{ for all } \theta \in \Theta \\ &\leq \min_{\phi, c \in \mathbb{R}} \; \phi\widehat{\theta} + c \quad \text{s.t.} \quad \underline{F}(\theta) \leq \phi\theta + c \text{ for all } \theta \in \Theta \end{aligned} \tag{A.5}$$

since $\underline{F}(\theta) \geq f - \widehat{f}$. Since $\underline{F}(\theta)$ is concave on Θ, we can write

$$\underline{F}(\theta) \leq \nabla \underline{F}_{\theta'}(\theta - \theta') + \underline{F}(\theta') \text{ for all } \theta, \theta' \in \Theta. \tag{A.6}$$

By (4.16), $\underline{F}(\theta) = \phi^{kl}\theta + c^{kl}$ for all $\theta \in \theta^{kl}$, therefore, for any $\theta' \in \theta^{kl}$ we have $\nabla \underline{F}_{\theta'} = \phi^{kl}$. Thus, we can rewrite (A.6) as

$$\underline{F}(\theta) \leq \phi^{kl}\theta + c^{kl} \text{ for all } \theta \in \Theta. \tag{A.7}$$

Utilizing the fact that the intervals θ^{kl} for all k, l are unique, we note that equality in (A.7) only holds for the interval θ^{kl}. Hence,

$$\underline{F}(\theta) < \phi^{kl}\theta + c^{kl} \text{ for all } \theta \notin \theta^{kl}. \tag{A.8}$$

With this information, we reformulate (A.5) as

$$\begin{aligned} \min_{\phi \in \mathbb{R}} \max_{\theta \in \Theta} \; J(\phi, \theta) \;&\leq\; \min_{\phi, c \in \mathbb{R}} \; \phi\widehat{\theta} + c \quad \text{s.t.} \quad \underline{F}(\theta) \leq \phi\theta + c \text{ for all } \theta \in \Theta \\ &\leq\; \min_{\phi, c \in \mathbb{R}} \; \phi\widehat{\theta} + c \quad \text{s.t.} \quad \underline{F}(\theta) = \phi^{kl}\theta + c^{kl} \text{ for all } \theta \in \theta^{kl} \\ &\qquad\qquad\qquad\qquad\quad \underline{F}(\theta) < \phi^{kl}\theta + c^{kl} \text{ for all } \theta \notin \theta^{kl}. \end{aligned} \tag{A.9}$$

The active constraints in (A.9) occur only in θ^{kl} so the solution of (A.9) is simply $\phi^{kl}\widehat{\theta} + c^{kl}$. The expansion of the constraint in (A.5) to the two constraints in (A.9) is not unique since the choice of k and l is arbitrary. Therefore, the optimum solution of (A.5) has to be minimum of all possible solutions derived from all possible sets of

constraints. This implies that

$$\begin{aligned}\min_{\phi\in\mathbb{R}}\max_{\theta\in\Theta}\ J(\phi,\theta) \ &\leq \ \min_{\phi,c\in\mathbb{R}}\ \phi\widehat{\theta}+c \quad \text{s.t.} \quad \underline{F}(\theta)\leq\phi\theta+c \text{ for all } \theta\in\Theta \\ &= \min\left\{\phi^{kl}\widehat{\theta}+c^{kl} \text{ for } k,l=1,\ldots,n\right\}.\end{aligned} \tag{A.10}$$

Recall that we have chosen $\widehat{\theta}\in\theta^{ij}$ and that when $i\neq k$, $j\neq l$, $\widehat{\theta}\notin\theta^{kl}$. Hence, from (A.10) it follows that

$$\underline{F}(\theta)<\phi^{kl}\widehat{\theta}+c^{kl} \text{ for all } k\neq i, \quad l\neq j.$$

We can now deduce that the minimal solution occurs if $k=i$ and $l=j$, thus yielding

$$\begin{aligned}\min_{\phi,c\in\mathbb{R}}\ \phi\widehat{\theta}+c \quad &= \quad \underline{F}(\widehat{\theta}) \quad = \quad \phi^{ij}\widehat{\theta}+c^{ij}. \\ \text{s.t. } \underline{F}(\theta)&\leq\phi\theta+c\end{aligned} \tag{A.11}$$

The optimal ϕ is given by $\phi^*=\phi^{ij}$. We must now show that the equality in (A.5) is attained. We will show that if $\underline{F}(\theta)$ was constructed to be strictly larger than $f-\widehat{f}$, the optimal solution would be larger and if $\underline{F}(\theta)$ was less than $f-\widehat{f}$ for some θ, the optimal solution would be smaller.

From (A.5) and (A.11), we have

$$\begin{aligned}\min_{\phi,c\in\mathbb{R}}\ \phi\widehat{\theta}+c \quad &\leq \quad \min_{\phi,c\in\mathbb{R}}\ \phi\widehat{\theta}+c \quad = \quad \phi^{ij}\widehat{\theta}+c^{ij}. \\ \text{s.t. } f-\widehat{f}&\leq\phi\theta+c \qquad \text{s.t. } \underline{F}(\theta)\leq\phi\theta+c\end{aligned}$$

Let $\underline{F}'(\theta)=\underline{F}(\theta)+\epsilon\geq f-\widehat{f}+\epsilon$, where $\epsilon>0$. This implies that

$$\begin{aligned}\min_{\phi,c\in\mathbb{R}}\ \phi\widehat{\theta}+c \quad &\leq \quad \min_{\phi,c\in\mathbb{R}}\ \phi\widehat{\theta}+c \quad = \quad \min_{\phi,c\in\mathbb{R}}\ \phi\widehat{\theta}+c \\ s.t.\ f-\widehat{f}&\leq\phi\theta+c \qquad s.t\ \underline{F}'(\theta)\leq\phi\theta+c \qquad s.t\ \underline{F}(\theta)\leq\phi\theta+c-\epsilon\end{aligned}. \tag{A.12}$$

Defining $c' = c - \epsilon$, we can rewrite (A.12) as

$$\begin{aligned} \min_{\phi, c' \in \mathbb{R}} \ & \phi\widehat{\theta} + c' + \epsilon \quad = \phi^{ij}\widehat{\theta} + c^{ij} + \epsilon. \\ s.t \ & \underline{F}(\theta) \leq \phi\theta + c' \end{aligned} \tag{A.13}$$

Now suppose $\underline{F}'(\theta) = \underline{F}(\theta) - \epsilon$. This implies that $\underline{F}' \leq f - \widehat{f}$ for some θ, for example $\widehat{\theta}$. Following the same argument as above, we notice that

$$\begin{array}{ccccc} \min\limits_{\phi, c \in \mathbb{R}} \ \phi\widehat{\theta} + c & \geq & \min\limits_{\phi, c \in \mathbb{R}} \ \phi\widehat{\theta} + c & = & \phi^{ij}\widehat{\theta} + c^{ij} - \epsilon. \\ s.t. \ f - \widehat{f} \leq \phi\theta + c & & s.t \ \underline{F}'(\theta) \leq \phi\theta + c & & \end{array} \tag{A.14}$$

The inequalities (A.12) and (A.14) imply that

$$\phi^{ij}\widehat{\theta} + c^{ij} - \epsilon \ \leq \ \begin{array}{c} \min\limits_{\phi, c \in \mathbb{R}} \ \phi\widehat{\theta} + c \\ s.t. \ f - \widehat{f} \leq \phi\theta + c \end{array} \ \leq \ \phi^{ij}\widehat{\theta} + c^{ij} + \epsilon. \tag{A.15}$$

Since $\underline{F}$ was constructed as a tight upper bound on $f - \widehat{f}$, i.e. $\underline{F} \geq f - \widehat{f}$, we have $\epsilon = 0$ in (A.15) and

$$\begin{array}{ccccc} \min\limits_{\phi, c \in \mathbb{R}} \ \phi\widehat{\theta} + c & = & \phi^{ij}\widehat{\theta} + c^{ij} & = & \underline{F}(\theta) \\ s.t. \ f - \widehat{f} \leq \phi\theta + c & & & & \end{array} \tag{A.16}$$

with the optimal ϕ given as $\phi^* = \phi^{ij}$. $\square$

List of References

[1] I. Mayergoyz A. Adly and A. Bergqvist. Preisach modeling of magnetostrictive hysteresis. *Journal of Applied Physics*, 69(8):5777–5779, 1991.

[2] B. Anderson and J.B. Moore. *Optimal Control: Linear Quadratic Methods*. Prentice Hall, Englewood Cliffs, NJ, 1990.

[3] K.J. Astrom and T. Hagglund. *Automatic Tuning of PID Controllers*. Instrument Society of America, Raleigh, NC, 1988.

[4] C. Bouton, R.C. Smith, and R. Zrostlik. Partial and full inverse compensation for hysteresis in smart material systems. *Proceedings of the*, American Control Conference, 2000.

[5] F.T. Calkins, R.C. Smith, and A.B. Flatau. An energy-based hysteresis model for magnetostrictive transducers. *IEEE Transactions on Magnetics*, 36(2):429–439, 2000.

[6] M.A. Dahleh and I.J. Diaz-Bobillo. *Control of Uncertain Systems: a linear programming approach*. Prentice Hall., New York, 1995.

[7] M.J. Dapino, R.C. Smith, and A.B. Flatau. Structural magnetic strain model for magnetostrictive transducers. *IEEE Transactions on Magnetics*, 36(3):545–556, 2000.

[8] D.C. Jiles and D.L. Atherton. Theory of ferromagnetic hysteresis. *Journal of Magnetism and Magnetic Materials*, 61:48–60, 1986.

[9] A Kojić, C. Cao, and A.M. Annaswamy. Parameter convergence in systems with convex/concave parameterization. *Proceedings of the American Control Conference*, pages 2240–2244, 2000.

[10] P.V. Kokotović and G. Tao. Adaptive control of plants with unknown hysteresis. *IEEE Transactions on Automatic Control*, 40:200–213, 1995.

[11] P.V. Kokotović and G. Tao. *Adaptive control of Systems with Actuator and Sensor Nonlinearities*. John Wiley and Sons, Inc., New York, 1996.

[12] F.L. Lewis and V.L. Syrmos. *Optimal control*. John Wiley and Sons, Inc., New York, 1995.

[13] D.K. Lindner. *Introduction to signals and systems*. McGraw-Hill, New York, 1999.

[14] Ai-Poh Loh, A.M. Annaswamy, and F.P. Skantze. Adaptation in the presence of a general nonlinear parameterization: an error model approach. *IEEE Transactions on Automatic Control*, 44(9):1634–1652, 1999.

[15] M.H. Khammash M.V. Salapaka and M. Dahleh. Solutions of mimo h_2/l_1 problems without zero interpolations. *CDC97*, pages 21546–1551, 1997.

[16] J. Nealis and R.C. Smith. Partial inverse compensation techniques for linear control design in magnetostrictive transducers. *Proc. SPIE, Smart Structures and Materials*, 4326:462–473, 2001.

[17] P.M. Prenter. *Splines and Variational Methods*. Wiley., New York, 1975.

[18] M.J. Dapino R.C. Smith and S. Seelecke. A free energy model for hysteresis in magnetostrictive transducers. *Journal of Applied Physics*, 93(1):458–466, 2003.

[19] R.C. Smith. Inverse compensation for hysteresis in magnetostrictive transducers. *Mathematical and Computer Modeling*, to appear.

[20] R.C. Smith and C.L. Hom. A domain wall theory for ferroelectric hysteresis. *Journal of Intelligent Material Systems and Structures*, 10(3):195–213, 1999.

[21] R.C. Smith and J.E. Massad. A unified methodology for modeling hysteresis in ferroelectric, ferromagnetic and ferroelastic materials. *Proceedings of DETC'01 the ASME Design Engineering Technical Conference and Computers and Information in Engineering Conference*, 6(B):62–79, 2000.

[22] R.C. Smith and Z. Ounaies. A domain wall model for hysteresis in piezoelectric materials. *Mathematical and Computer Modeling*, 11(1):62–79, 2000.

[23] M.H. Khammash X. Qi and M.V. Salapaka. A matlab package for multiobjective control synthesis. *Proceedings of the 40th IEEE Conference on Decision and Control*, pages 3991–3996, 2001.

[24] M.H. Khammash X. Qi and M.V. Salapaka. Optimal controller synthesis with multiple objectives. *ACC00*, pages 2730–2735, 2001.

[25] R. Venkataraman X. Tan and P.S. Krishnaprasad. Control of hysteresis: theory and experimental results. *Smart Structures and Materials 2001, Modeling, Signal Processing and Control in Smart Structures*, 4326:101–112, 2001.

[26] K. Zhou and J.C. Doyle. *Essentials of Robust Control*. Prentice Hall., New York, 1998.